# EXPERIMENTAL STUDIES OF INTEGER SPIN ANTIFERROMAGNETIC CHAINS

By

GARRETT E. GRANROTH

A DISSERTATION PRESENTED TO THE GRADUATE SCHOOL
OF THE UNIVERSITY OF FLORIDA IN PARTIAL FULFILLMENT
OF THE REQUIREMENTS FOR THE DEGREE OF
DOCTOR OF PHILOSOPHY

UNIVERSITY OF FLORIDA

1998

ACKNOWLEDGMENTS

I am sincerely grateful for the guidance and encouragement of my thesis advisor Professor Mark Meisel. Many thanks go to Professors Selman Hershfield, Gary Ihas, Kevin Ingersent, Stephen Nagler, Fred Sharifi, and Dan Talham for serving on my supervisory committee at one time or another. Special thanks go to the materials wizards Brian Ward and Liang-Keui Chou and their supervisor Professor Dan Talham for synthesizing the samples. Several people have provided help with various measurements. Thanks to Dr. Murali Chaparala for help with the cantilever magnetometer and interpretation of the resultant data. Thanks to Dr. Brian Chakoumakos for assistance with the powder neutron diffractometer and for advice concerning Rietveld refinement. Thanks to Dr. Jeff Lynn and Dr. Ross Erwin for assistance with the time of flight neutron diffraction experiments. Thanks to Brian Ward, Liang-Keui Chou, and Candace Seip for operating the 9 GHz ESR spectrometer. Thanks to Gail Fanucci for running the NINAZ on the high field ESR spectrometer. Thanks to Nelson Bell and his advisor Professor Jim Adair for preparing the ball milled samples and for characterizing their particle size. Thanks to Dr. Thierry Jolicœur for help with many aspects of the theory for $S = 2$ chains and for providing the high temperature series expansions for $S = 1$ chains. I am grateful for several fruitful discussions with Kingshuk Majumdar and Dr. Arnold Sikkema that have helped me to understand non-linear sigma models and other theoretical obfuscations. Several individuals

have provided tutelage along the path to this degree. Professor Stephen Nagler helped with the neutron scattering experiments. Professor Satoru Maegawa gave stimulating input on the NINAZ work. Dr. Philippe Signore provided the essential knowledge that is passed down the line of graduate students. Professor Kevin Riggs introduced me to experimental studies of magnetic materials using microwave resonance techniques. I would also like to thank my high school chemistry teacher Mrs. Dorris Wasson for encouraging me to choose a career in science.

I am always grateful for the encouragement of my parents and family that has helped me along the way. Additionally, I would like to acknowledge the Creator who provides endless scientific problems to study. Finally, I am indebted to Amelia Helmus for grammatical editing of this thesis.

TABLE OF CONTENTS

ACKNOWLEDGMENTS . . . . . ii

LIST OF FIGURES . . . . . vii

ABSTRACT . . . . . xi

CHAPTERS

1 INTRODUCTION . . . . . 1

2 REVIEW OF THEORETICAL STUDIES . . . . . 3

2.1 Theoretical Models . . . . . 4
2.1.1 The Non-Linear Sigma Model . . . . . 4
2.1.2 Valence Bond Solids . . . . . 6
2.2 An Intuitive Picture of the Haldane Gap . . . . . 9
2.3 Numerical Studies of Quantum Spin Chains . . . . . 10
2.3.1 Realistic Hamiltonians . . . . . 18
2.4 Measurement Theory . . . . . 22
2.4.1 Electron Spin Resonance . . . . . 24

3 REVIEW OF EXPERIMENTAL STUDIES . . . . . 30

3.1 Haldane Gap Materials . . . . . 30
3.2 Experimental Tests of the Haldane Gap . . . . . 32
3.3 Studies of End-chain Spins . . . . . 40
3.4 Other Experimental Results . . . . . 45

4 EXPERIMENTAL MEASUREMENT TECHNIQUES . . . . . 48

4.1 SQUID Magnetometer . . . . . 48
4.2 Cantilever Magnetometer . . . . . 54
4.3 Electron Spin Resonance . . . . . 61
4.4 Neutron Scattering . . . . . 68

4.5 Mechanical Ball Milling . . . . . 74
4.6 Centripetal Sedimentation . . . . . 74
4.7 Inductively Coupled Plasma Mass Spectrometry . . . . . 76

5 TMNIN . . . . . 78

5.1 Synthesis and Structure of TMNIN . . . . . 78
5.2 Magnetization Measurements on TMNIN . . . . . 80
5.3 Comparison with Other Experiments . . . . . 89

6 NINAZ . . . . . 92

6.1 Material Description . . . . . 93
6.2 Other Experiments . . . . . 96
6.3 Experimental Studies . . . . . 99
6.3.1 Samples . . . . . 99
6.3.2 $[Ni(C_4H_{12}N_2)_2(\mu-N_3)]_n(ClO_4)_n$ . . . . . 103
6.3.3 Macroscopic Measurements . . . . . 108
6.3.4 Microscopic Measurements: Electron Spin Resonance . . . 117

7 THE $S = 2$ HALDANE GAP IN $MnCl_3$(bipy) . . . . . 153

7.1 $S = 2$ Quasi-linear Chain Materials . . . . . 154
7.1.1 $MnCl_3$(phen) . . . . . 154
7.1.2 $Mn(acac)_2N_3$ . . . . . 154
7.1.3 Mn(salpn)OAc . . . . . 157
7.1.4 $MnCl_3$(bipy) . . . . . 161
7.1.5 Synthesis . . . . . 161
7.2 Macroscopic Magnetic Measurements of $MnCl_3$(bipy) . . . . . 164
7.3 Low Temperature Crystal Structure: Preparation for Microscopic Measurements . . . . . 175
7.4 Inelastic Neutron Scattering Measurements . . . . . 180

8 CONCLUSIONS . . . . . 196

8.1 TMNIN . . . . . 196
8.2 NINAZ . . . . . 197
8.3 $MnCl_3$(bipy) . . . . . 198

APPENDICIES

A High Temperature Expansions . . . . . 200

A.1 Specific Heat . . . . . 200
A.2 Perpendicular Magnetic Susceptibility . . . . . 214
A.3 Parallel Magnetic Susceptibility . . . . . 220

B Low Temperature Crystallographic data for $MnCl_3$(d-bipy) . . . . . 226

BIBLIOGRAPHY . . . . . 232

BIOGRAPHICAL SKETCH . . . . . 240

LIST OF FIGURES


2.1 A single valence bond . . . . . 6
2.2 An $S = 1/2$ chain in the RVB picture . . . . . 7
2.3 An $S = 1$ chain according to a VBS model . . . . . 7
2.4 The VBS state for an $S = 2$ chain . . . . . 8
2.5 $S = 1$ chain dispersion curve . . . . . 13
2.6 Staggered magnetization for $S = 1$ chains . . . . . 16
2.7 $1/\chi$ vs. $T$ for end-chain spins from QMC work . . . . . 17
2.8 $S = 1$ phase diagram . . . . . 19
2.9 $S = 2$ phase diagram . . . . . 21
2.10 Energy level diagram showing the Haldane gap . . . . . 23
2.11 Allowed transitions between end-chain spin states . . . . . 27

3.1 $M(H)$ for NENP . . . . . 34
3.2 Inelastic neutron scattering intensity for $Y_2BaNiO_5$ . . . . . 36
3.3 $\chi(400\,\mu\text{K} < T < 300\,\text{K})$ for pure NENP . . . . . 44
3.4 The crystal structure of NENP . . . . . 46

4.1 $M(T)$ SQUID background . . . . . 52
4.2 $M$(H) SQUID background . . . . . 53
4.3 Cantilever magnetometer diagram . . . . . 55
4.4 Cantilever magnetometer electronics schematic . . . . . 59
4.5 Schematic diagram of the X-band ESR spectrometer . . . . . 62
4.6 Cross-sectional schematic view of the ESR flow cryostat . . . . . 64
4.7 $dI/dH$ vs. $H$ for a 0.1 mg sample of DPPH . . . . . 66
4.8 $I$ vs. $H$ for a 0.1 mg sample of DPPH . . . . . 67
4.9 NIST TOF spectrometer . . . . . 73
4.10 A normalized log-normal distribution . . . . . 75
4.11 Schematic diagram of an ICP-MS system . . . . . 77

5.1 TMNIN Crystal Structure . . . . . 79
5.2 SQUID $M$ vs. $B$ for TMNIN . . . . . 81
5.3 $F$ and $M$ vs. $B_\perp$ for TMNIN packet 16 cm off the center of the field 83
5.4 $F$ and $M$ vs. $B_\parallel$ for TMNIN packet 16 cm off the center of the field 85
5.5 $F$ and $M$ vs. $B_\perp$ for TMNIN packet 5 cm off the center of the field 86
5.6 $F$ and $M$ vs. $B_\perp$ for TMNIN single crystal . . . . . 87

5.7 $F$ and $M$ vs. $B_{\|}$ for TMNIN single crystal . . . . . 88

6.1 Room temperature NINAZ crystal structure . . . . . 94
6.2 DC $\chi(T)$ of NINAZ . . . . . 97
6.3 Constant $Q \approx \pi$ inelastic neutron scattering data for deuterated NINAZ . . . . . 98
6.4 Powder NINAZ particle size distributions . . . . . 101
6.5 Ultrafine powder NINAZ particle size distributions . . . . . 102
6.6 The crystal structure of $[Ni(C_4H_{12}N_2)_2(\mu{-}N_3)]_n(ClO_4)_n$ . . . . . 105
6.7 $\chi_{\perp}(2\,K < T < 300\,K)$ for $[Ni(C_4H_{12}N_2)_2(\mu{-}N_3)]_n(ClO_4)_n$ . . . . . 106
6.8 $\chi_{\|}(2\,K < T < 300\,K)$ for $[Ni(C_4H_{12}N_2)_2(\mu{-}N_3)]_n(ClO_4)_n$ . . . . . 107
6.9 $\chi(50\,mK < T < 2\,K)$ of polycrystalline and powder NINAZ . . . . 109
6.10 $\chi(T)$ for powder and ultrafine powder NINAZ . . . . . 110
6.11 $M(H < 5\,T, 2\,K)$ for polycrystalline, powder, and ultrafine powder NINAZ samples . . . . . 112
6.12 $\chi(T)$ for doped NINAZ samples . . . . . 114
6.13 $M(H < 5\,T, 2\,K)$ for doped NINAZ samples . . . . . 116
6.14 Typical ESR lines for polycrystalline, powder and ultrafine powder samples of NINAZ . . . . . 119
6.15 ESR line for a polycrystalline sample of NINAZ . . . . . 120
6.16 ESR spectra for a polycrystalline NINAZ sample as a function of angle . . . . . 122
6.17 ESR peak $g$ values as function of angle in a polycrystalline sample 123
6.18 Hg doped NINAZ ESR spectrum . . . . . 125
6.19 Hg doped NINAZ ESR peak $g$ values as function of angle . . . . . 126
6.20 $T$ dependence of ESR lines for $H \perp$ to the chains of a NINAZ polycrystalline sample from Batch 1 . . . . . 129
6.21 $T$ dependence of ESR lines for $H \|$ to the chains of a NINAZ polycrystalline sample from Batch 1 . . . . . 130
6.22 $T$ dependent ESR spectra for $H \|$ to the chains of a NINAZ polycrystalline sample . . . . . 131
6.23 $T$ dependence of ESR lines for $H \perp$ to the chains of a NINAZ polycrystalline sample from Batch 2 . . . . . 132
6.24 ESR $I(T)$ for a NINAZ polycrystalline sample from Batch 1 . . . 133
6.25 ESR $I(T)$ for a NINAZ polycrystalline sample from Batch 2 . . . 134
6.26 $T$ dependence of the ESR line for a powder sample of NINAZ . . 136
6.27 $T$ dependence of the ESR line for an ultrafine powder sample of NINAZ . . . . . 137
6.28 $I(T)$ for powder and ultrafine powder NINAZ samples . . . . . 138

6.29 Energy level diagram for powder NINAZ . . . . . 140
6.30 ESR FWHM vs. $T$ for powder and ultrafine powder NINAZ . . . 142
6.31 $1/\chi$ vs. $T$ for powder and ultrafine powder NINAZ . . . . . 144
6.32 The ratio of the area under ultrafine powder data to the area under the powder data for NINAZ . . . . . 145
6.33 $\chi(T) \cdot T$ for the powder and ultrafine powder samples of NINAZ from Batch 1 . . . . . 147
6.34 NINAZ ESR spectrum at 93.934 GHz, increasing $H$ . . . . . 148
6.35 NINAZ ESR spectrum at 93.934 GHz, decreasing $H$ . . . . . 149
6.36 NINAZ ESR spectrum at 189.866 GHz, increasing $H$ . . . . . 150
6.37 NINAZ ESR spectrum at 189.866 GHz, decreasing $H$ . . . . . 151
6.38 $g$ vs. $\nu$ for ESR in a NINAZ powder sample . . . . . 152

7.1 Approximate crystal structure of $MnCl_3$(phen) . . . . . 155
7.2 $M(T)$ for $MnCl_3$(phen) . . . . . 156
7.3 Crystal structure of $Mn(acac)_2N_3$ . . . . . 158
7.4 $M(T)$ of $Mn(acac)_2N_3$ . . . . . 159
7.5 Crystal structure of Mn(salpn)OAc . . . . . 160
7.6 $\chi(T)$ of Mn(salpn)OAc . . . . . 162
7.7 Crystal structure of $MnCl_3$(bipy) . . . . . 163
7.8 $\chi(T)$ of $MnCl_3$(bipy) . . . . . 166
7.9 9 GHz ESR signal intensity vs. $T$ for $MnCl_3$(bipy) . . . . . 168
7.10 SQUID $M$ vs. $H$ measurement of $MnCl_3$(bipy) . . . . . 170
7.11 Raw $M$ vs. $H$ data for three crystals of $MnCl_3$(bipy) . . . . . 171
7.12 Raw $M$ vs. $H$ data for one crystal of $MnCl_3$(bipy) . . . . . 172
7.13 $M$ vs. $H$ data for two oriented crystals of $MnCl_3$(bipy) . . . . . 174
7.14 Powder diffraction pattern, Rietveld refinement, and difference plot for $MnCl_3$(d-bipy) . . . . . 177
7.15 Crystal structure near a Mn atom in $MnCl_3$(d-bipy) . . . . . 178
7.16 $a$ vs. $T$ for $MnCl_3$(d-bipy) . . . . . 181
7.17 $b$ vs. $T$ for $MnCl_3$(d-bipy) . . . . . 182
7.18 $c$ vs. $T$ for $MnCl_3$(d-bipy) . . . . . 183
7.19 $\gamma$ vs. $T$ for $MnCl_3$(d-bipy) . . . . . 184
7.20 V vs. $T$ for $MnCl_3$(d-bipy) . . . . . 185
7.21 Estimated $S = 2$ dispersion for $MnCl_3$(bipy) and theoretical TOF spectrometer behavior . . . . . 186
7.22 Incoherent scattering from a vanadium standard . . . . . 188
7.23 Incoherent scattering from the $MnCl_3$(d-bipy) sample . . . . . 189
7.24 Inelastic neutron scattering intensity at $T = 0.4$ K and $Q \approx \pi$ . . 191

7.25 Inelastic neutron scattering intensity at $T = 0.4$ K and $Q \ll \pi$ . . 192
7.26 Inelastic neutron scattering intensity near $Q = \pi$ at $T = 10$ K . . 194

Abstract of Dissertation Presented to the Graduate School
of the University of Florida in Partial Fulfillment of the
Requirements for the Degree of Doctor of Philosophy

# EXPERIMENTAL STUDIES OF INTEGER SPIN ANTIFERROMAGNETIC CHAINS

By

Garrett E. Granroth

May 1998

Chairman: Mark W. Meisel
Major Department: Physics

Experimental studies of several $S = 1$ and $S = 2$ antiferromagnetic chain materials have uncovered novel phenomena. Firstly, measurements on $MnCl_3(C_{10}H_8N_2)$ provided the first evidence of an $S = 2$ Haldane gap. Secondly, studies of the $S = 1$ material $Ni(C_3H_{10}N_2)_2N_3(ClO_4)$, NINAZ, demonstrated the presence of $S = 1/2$ end-chain spins and provided evidence of their interactions with the magnetic excitations on the chain. Thirdly, investigations of the $S = 1$ material $(CH_3)_4N[Ni(NO_2)_3]$, TMNIN, revealed a small single-ion anisotropy, $D$. Finally, the magnetic properties of $MnCl_3(C_{12}H_8N_2)$, $Mn(C_5H_7O_2)_2N_3$, $Mn(C_{17}H_{15}O_3N_2)CH_3COO$, and $Ni(C_4H_{12}N_2)_2(\mu\text{-}N_3)]_n(ClO_4)_n$ were studied in a search for additional systems with properties similar to the aforementioned materials.

Magnetic field, $H$, dependent magnetization, $M$, measurements at $T = 30$ mK for $H \leq 16$ T have demonstrated $MnCl_3(C_{10}H_8N_2)$ to be the first known $S = 2$ material to posses a Haldane gap. Specifically, $M \approx 0$ until critical fields $H_{c\perp} = 1.8 \pm 0.2$ T and $H_{c\parallel} = 1.2 \pm 0.2$ T are reached for $H$ oriented perpendicular and parallel to the chains respectively. These critical fields and the intra-chain exchange $J = 34.8 \pm 1.6$ K reveal a Haldane gap of $\Delta = 2.3 \pm 0.8$ K and $D/J = 0.010 \pm 0.003$, which are consistent with theoretical predictions for $S = 2$ antiferromagnetic chains. Furthermore, preliminary inelastic neutron scattering data possess a possible magnetic scattering peak at an energy consistent with the Haldane gap.

Polycrystalline, two powders with different particle sizes, and doped samples of NINAZ were used to study end-chain spin effects. Fits to $M(H \leq 5\,\mathrm{T}, T = 2\,\mathrm{K})$, for all the samples, confirm that the end-chain spins are $S = 1/2$. The electron spin resonance, ESR, intensity as a function of temperature, provided a microscopic comparison of the chain lengths to the macroscopic particle size distributions. Finally, the ESR line widths of the powder samples are consistent with a model describing interactions between the magnetic excitations on the chains and the end-chain spins.

Measurements of $M(H \leq 8\,\mathrm{T}, T = 25\,\mathrm{mK})$ performed on both an oriented packet of single crystals and individual single crystals of TMNIN have revealed $H_{c\perp} = 2.60 \pm 0.15$ T and $H_{c\parallel} = 2.40 \pm 0.15$ T. These critical fields, along with $J = 10$ K, determine $\Delta = 3.5 \pm 2$ K and $D/J = 0.06 \pm 0.03$.

# CHAPTER 1
# INTRODUCTION

Ever since the pioneering theoretical work by Bethe [1], studies of antiferromagnetic chains have illuminated new phenomena related to quantum magnetism. A particularly intriguing theoretical prediction, made by Haldane [2,3], is that Heisenberg antiferromagnetic chains have a gap between a singlet ground state and a triplet excited state for integer spin, in contrast to the half-integer spin case that has no gap. This prediction sparked a flurry of theoretical and experimental work that is reviewed in Chapters 2 and 3, respectively. The majority of this dissertation presents experimental studies on three materials that provide insight into several different phenomena related to the Haldane state. Chapter 4 explains the experimental techniques used to study these samples. Chapter 5 discusses magnetization measurements identifying the Haldane gap and a small single-ion anisotropy in the $S = 1$ material $(CH_3)_4N[Ni(NO_2)_3]$, TMNIN. Chapter 6 details our extensive studies of $S = 1/2$ end-chain spins in the $S = 1$ system $Ni(C_3H_{10}N_2)_2N_3(ClO_4)$, NINAZ, using magnetization, magnetic susceptibility, and electron spin resonance. In addition to the intrinsic crystal shattering processes, chain breaks were generated in NINAZ primarily by pulverization techniques, and in a few cases by doping. Chapter 7 covers the search and discovery of the $S = 2$ Haldane gap. The discussion is focused on $MnCl_3(bipy)$, where bipy $= C_{10}H_8N_2$, for which our magnetic field dependent magnetization

measurements at $T = 30$ mK provide the first evidence of the $S = 2$ Haldane gap. In addition, preliminary neutron scattering results, which microscopically test the $S = 2$ Haldane gap, are presented. Finally, Chapter 8 will review the conclusions of the previous chapters and provide suggestions for further study.

# CHAPTER 2
# REVIEW OF THEORETICAL STUDIES

Since the nascence of quantum mechanics, quantum antiferromagnetism has provided puzzling theoretical problems. The Heisenberg Hamiltonian

$$\mathcal{H} = J \sum_i \mathbf{S}_i \cdot \mathbf{S}_{i+1} \tag{2.1}$$

describes the system where $J$, the exchange, characterizes the strength of the interaction between nearest neighbor spins and $\mathbf{S}_i$ is the spin at the $i$th site. The ground state of this system is inherently difficult to find, so several approximations have been used. A common approximation is the classical limit, where $S \to \infty$. In this limit, the three-dimensional ground state is long-range ordered with no net magnetization because each spin is oriented opposite its nearest neighbors. This state can be represented by $|\uparrow\downarrow\uparrow\downarrow\uparrow\downarrow>$. However, when the spins are quantized, it is easily shown that a state exists below the classical ground state [4]. Nevertheless, the true ground state remains unsolved. Consequently, several other simplifying assumptions have been made, and the one pertinent to this thesis is to reduce the system to one dimension. Even the one-dimensional, 1-D, case is difficult to handle theoretically. Attempts at using the classical approximation reveal a negatively divergent correlation length, known as the long wavelength divergence. Most of the theoretical progress on 1-D antiferromagnets has involved creative methods of avoiding this divergence. Bethe in 1931 [1, 5]

successfully circumvented this divergence for the $S = 1/2$ Heisenberg model by a technique know as the Bethe *ansatz*. Unfortunately, the resultant ground state is hard to manipulate, so further predictions about the dispersion were not made until 1962 [6]. The difficulty of the theory discouraged theoretical work for higher spins values. It was not until Haldane [2,3] used clever limits on an approximate model that evidence of a gap in the integer spin case was observed. Since then, several approximate models have been used to describe the properties of integer spin antiferromagnetic chains. Therefore, this chapter begins with an overview of the two primary theoretical models used: the non-linear sigma model (NL$\sigma$M) and the valence bond solid (VBS) model. Since the details of these models may obfuscate the physical processes behind the predicted phenomena, a physically intuitive argument for gapped integer and gapless half integer spin chains will be given next. Then, a discussion of realistic Hamiltonians and the numerical studies that illuminated their properties will be provided to connect the theory to the experiment. The chapter will finish with several theoretical details on the experimental techniques used.

## 2.1 Theoretical Models

### 2.1.1 The Non-Linear Sigma Model

Haldane proposed, in 1983, that integer and half integer Heisenberg spin chains would have a fundamentally different excitation spectrum [2,3]. By making an approximation, to be described below, he proposed that the integer spin case has a singlet ground state and a triplet excited state separated by an energy

gap, $\Delta$, and the half integer spin case is gapless. The half integer spin case is completely consistent with previous exact work, but the integer case was an unexpected prediction that started a flurry of theoretical and experimental research. In his approach, he assumed that order existed for some distance larger than the lattice spacing but smaller than the long-range ordered domains. This assumption of short-range order circumvents long wave length divergences found in the classical spin wave approach [5]. Next, the system was mapped from a statistical mechanical model to a field theory in (1+1) dimensions, namely a NL$\sigma$M. Once the mapping is complete, the $S \to \infty$ limit [7–9] reveals a gap in the excitation spectrum for the integer spin chain and no gap for the half integer spin chain. More specifically, the Haldane gap, $\Delta$, is proportional to $e^{-\pi S}$, and the correlation length between spins, $\xi$, is proportional to $e^{\pi S}$ [7]. There is only one problem with this approach. Spins of value one and one half can hardly be called large, and in fact, this technique [8,10] provides inconclusive results for $S \leq 1$. Studies of the NL$\sigma$M are well documented in the literature [7–9,11,12], so further details are beyond the scope of this thesis.

Non-linear sigma models have been extended beyond arguing the existence of the Haldane gap. Jolicœur and Golinelli used the $N \to \infty$ limit to study $\Delta(T)$ for $T < \Delta$. The result is an "anti-BCS" gap of the form [10]

$$\Delta(T) \approx \Delta(0) + \sqrt{2\pi\Delta(0)T}\, e^{-\Delta(0)/T}. \tag{2.2}$$

Furthermore, they calculated the free energy and used it to derive expressions for the low temperature specific heat

$$C_V(T) \approx \frac{N\Delta(0)}{\sqrt{2\pi}} \left(\frac{\Delta(0)}{T}\right)^{3/2} e^{-\Delta(0)/T} \tag{2.3}$$

and magnetic susceptibility

$$\chi(T) \approx \sqrt{\frac{8}{\pi}} \left(\frac{\Delta(0)}{T}\right)^{1/2} e^{-\Delta(0)/T}. \tag{2.4}$$

### 2.1.2 Valence Bond Solids

Another approach that has been both theoretically and experimentally illuminating is the valence bond solid (VBS) model, also called the AKLT model, introduced by Affleck, Kennedy, Lieb, and Tasaki [13, 14]. Anderson [15, 16] initially introduced valence bonds in the resonating valence bond (RVB) model to suggest the existence of a quantum disordered ground state in an $S = 1/2$ two-dimensional antiferromagnet. This model has been used to explain some features of high-$T_c$ superconductivity [7, 16] and may accurately describe spin ladders [17]. A valence bond is a bond between two $S = 1/2$ spins at two sites [7]. The bond is commonly represented [7, 14] as a solid line between the $S = 1/2$ sites given as points. Figure 2.1 shows a valence bond for two $S = 1/2$ entities. It is easily determined that for $S = 1/2$ spins on any lattice, there are multiply degenerate



Figure 2.1: A single valence bond.

configurations of valence bonds, hence the name resonating valence bond [7, 15]. For example, Figure 2.2 shows an RVB configuration for an $S = 1/2$ chain where the dashed lines are the unoccupied bonds, but an equally probable state is one where the dashed lines are the valence bonds and the solid lines are not; therefore, these two states are in resonance. Affleck, Kennedy, Lieb and Tasaki [13,14]

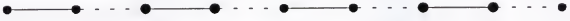

Figure 2.2: An $S = 1/2$ chain in the RVB picture.

extended the theory by examining valence bonds on lattices with higher spin. They consider an $S = 1$ site as two $S = 1/2$ entities, represented by two points enclosed by a circle. Therefore, Figure 2.3 shows an $S = 1$ chain coupled by valence bonds. Clearly, there is no degeneracy, so the singlet ground state is "solid"

Figure 2.3: An $S = 1$ chain according to a VBS model.

when compared to the resonating bonds of the $S = 1/2$ chain. A continuation of the theory in Figure 2.4 shows an $S = 2$ chain can also be modeled as a valence bond solid. Another look at Figures 2.3 and 2.4 shows an interesting property of VBS models, namely that finite chains terminate with spins of value $S/2$. This feature will be discussed more below.

Up to this point in the discussion, nothing has been said about the system for which the VBS state is the ground state nor how closely related the system is

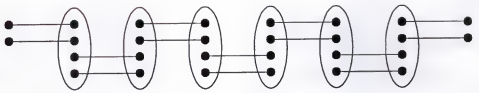

Figure 2.4: The VBS state for an $S = 2$ chain.

to a Heisenberg model. By assuming the VBS state is the ground state of some Hamiltonian, and working backward to find it, the $S = 1$ Hamiltonian

$$\mathcal{H} = J \sum_i S_i \cdot S_{i+1} - \beta \left( S_i \cdot S_{i+1} \right)^2 \tag{2.5}$$

is obtained where, for now, $\beta = -1/3$, but it will be varied later in the discussion [13, 14]. This system exhibits a gap [7, 14], albeit with an energy, $\sim 0.350J$, significantly smaller than the Haldane gap. To compare the properties between this system and the Heisenberg system, Kennedy [18] performed exact diagonalization studies on Equation 2.5 for a range of $\beta$ values. He confirmed a continuous region of phase space in $\beta$ from $-1/3$ through 0, so the gap and the end-chain spins should be realized for the Heisenberg model as well. Equation 2.5 is for $S = 1$ chains. A different Hamiltonian is constructed when a similar procedure is carried out for an $S = 2$ chain, and the result is not as closely related to the Heisenberg Hamiltonian [7, 14] as Equation 2.5. Nevertheless, the VBS model provides some physical intuition to help understand the experimental results in an $S = 2$ system.

## 2.2 An Intuitive Picture of the Haldane Gap

Though the VBS model produces a physically intuitive explanation for the presence of $S = 1/2$ spins at the ends of a finite $S = 1$ spin chain, it does not provide similar intuition for the presence of a gap for the integer spin case and the absence of it for the $1/2$ integer spin case. The NL$\sigma$M is even less intuitive. Nevertheless, the following argument, derived from the large body of theoretical and numerical work, lucidates the physical origin of the Haldane gap [19]. To start from a long-range ordered ground state

$$|\uparrow\downarrow\uparrow\downarrow\uparrow\downarrow\uparrow\downarrow>, \tag{2.6}$$

assume an Ising system

$$\mathcal{H} = J \sum S_i^z S_{i+1}^z. \tag{2.7}$$

Next, make the spins more isotropic, thereby approaching the Heisenberg model

$$\mathcal{H} = J \sum_i S_i^+ S_{i+1}^- + S_{i+1}^+ S_i^- + S_i^z S_{i+1}^z, \tag{2.8}$$

where $S^+ = S^x + iS^y$ and $S^- = S^x - iS^y$. Clearly, the added interactions destabilize the long-range ordered state, so there is a lower ground state. Nevertheless, for the ground state to remain antiferromagnetic, $< M >= 0$. Therefore, the ground state must at least be the superposition of short-range ordered antiferromagnetic states. If a source of energy (*i.e.* $T$, $H$) is added to the system so as to cause one spin to locally increase above the ground state, the new state for the $S = 1/2$ chain is

$$|\downarrow\uparrow\downarrow\uparrow\downarrow\uparrow\downarrow> \tag{2.9}$$

that has $< M > \neq 0$ which is indicative of an excited state. In sharp contrast, a spin on the $S = 1$ chain has the $S_z = 0$ state as its next excited state. Therefore, the many-body state of the $S = 1$ chain with an excitation on it would look like

$$|0\downarrow\uparrow\downarrow\uparrow 0\downarrow\uparrow> . \tag{2.10}$$

Clearly, $< M >= 0$, so this state is degenerate with the ground state. If more energy is added to the system, only when the $\Delta S_z = 1$ transition becomes the most probable for each site does $< M > \neq 0$, and the ground state is destroyed. Since a finite quantum of energy must be added to the system for this transition to occur, an energy gap in the excitation spectrum is observed.

A further interesting theoretical observation can be made from the above discussion. First, notice that as long as two of the spins are arranged in the zero state, they can be anywhere along the chain. Second, notice that if the zeros were simply removed from the chain, the spins across the empty space would be antiferromagnetically arranged. This result is know as hidden (or string) order and was first identified by Tasaki [20].

## 2.3 Numerical Studies of Quantum Spin Chains

Other tools useful for characterizing spin chain behavior and for connecting the theory to experimentally studied systems are numerical techniques. Four techniques have been used, and they are high temperature series expansions,

exact diagonalization, quantum Monte Carlo (QMC), and density matrix renormalization group (DMRG). High temperature series expansions have produced expressions for the directly measurable quantities $C_V(T)$, the specific heat, and $\chi(T)$, the magnetic susceptibility. Weng [21] performed expansions of $\chi(T)$ for $S = 1/2$, 1, and $\infty$. Furthermore, he extrapolated between the $S = 1$ and $S = \infty$ results to determine $\chi(T)$ for $S = 2$ and $S = 3/2$. Meyer *et al.* [22] have generated a rational function representation of Weng's $S = 1$ curve, namely

$$\chi(T) = \frac{N\mu_B^2 g^2}{k_B T}\left[\frac{2 + 0.0194X + .777X^2}{3 + 4.346X + 3.232X^2 + 5.834X^3}\right] \tag{2.11}$$

where $X = J/k_B T$. In a similar manner, Hiller *et al.* [23] arrived at a more versatile group of rational functions which can be used for many different values of $S$ as given by

$$\chi(T) = \frac{N\mu_B^2 g^2}{k_B T}\left[\frac{A + Bx^2}{1 + Cx + Dx^3}\right] \tag{2.12}$$

where $x = J/(2k_B T)$ and the coefficients are given in Table 2.1. All of these

| $S$ | $A$ | $B$ | $C$ | $D$ |
|---|---|---|---|---|
| 1/2 | 0.2500 | .18297 | 1.5467 | 3.4443 |
| 1 | .6667 | 2.5823 | 3.605 | 39.558 |
| 3/2 | 1.2500 | 17.041 | 6.7360 | 238.47 |
| 2 | 2.0000 | 71.938 | 10.482 | 9555.56 |

Table 2.1: Coefficients as a function of $S$ for Equation 2.12 from Reference [23].

expressions are only for the Heisenberg model. Recent extensions to Hamiltonians including single-ion anisotropy will be discussed below. In recent QMC studies,

Yamamoto and Miyashita [24] calculated the temperature dependent magnetic susceptibility and specific heat of open and closed chains for $0.1J < T < 5J$. Their work agrees well with the high temperature expansions above $J$ and with the exponential excitation of a gap below $J$, until end-chain spin effects become important. Further discussion of the end-chain spin effects will be given below.

Furthermore, QMC has been used to determine the dispersion curves of linear chain systems. Figure 2.5 shows the $S = 1$ dispersion as $Q$ is varied from 0 to $\pi$ [25, 26]. One interesting feature is that the points suggest the gap at $Q = 0$ is larger than the one at $Q = \pi$. This feature has been interpreted as evidence of a two particle continuum of excited states near $Q = 0$, instead of the triplet excitations at $Q = \pi$ [25–29]. The solid and dashed lines in Figure 2.5 show the agreement between the theoretically predicted curves and the QMC data for the triplet excitations at $Q = 0$ and the two particle excitations at $Q = \pi$, respectively. The net result is a gap of $2\Delta$ at $Q = 0$ and $\Delta$ at $Q = \pi$. Meshkov [29] performed QMC work on an $S = 2$ chain to determine the dispersion. Similar to the $S = 1$ case, the $Q = 0$ gap is twice the $Q = \pi$ gap. In addition for both the $S = 1$ and $S = 2$ cases, $S(Q, \omega)$ looses intensity and broadens as $Q \to 0$ [29]. This loss of intensity explains why the $2\Delta$ gap has not been observed. Detailed discussion of the shape of $S(Q, \omega)$ is not required for this thesis and is discussed at length in the literature, so no further comments will be made here. The DMRG technique has been shown to determine very precise results for relatively long chains ($\sim$ 60 sites) [30–33], but unfortunately it is limited to $T = 0$. A combination of QMC, exact diagonalization, and DMRG studies produced the

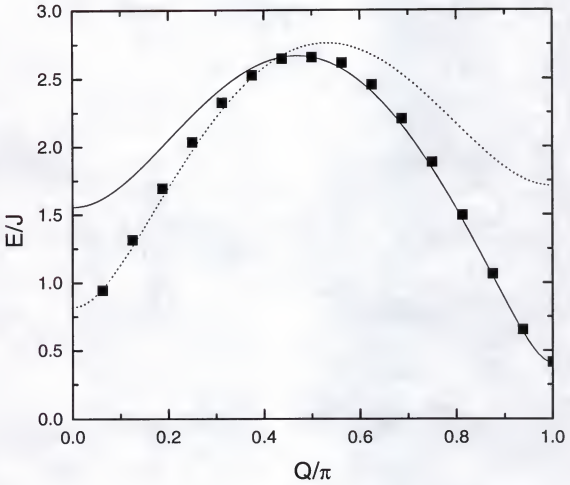


Figure 2.5: $S = 1$ chain dispersion curve. The squares are the dispersion for a 1-D $S = 1$ Heisenberg antiferromagnet calculated by QMC [25, 26]. The solid line is the expected dispersion for single particle excitations and the dotted line is the expected dispersion for the two particle continuum [28].

| $\Delta/J$ | Reference |
|---|---|
| 0.08 | Deisz *et al.* [34] |
| $0.055 \pm 0.015$ | Nihiyama *et al.* [35] |
| 0.05 | Sun [36] |
| $0.085 \pm 0.005$ | Schollwöck *et al.* [37,38] |
| $0.049 \pm 0.018$ | Yamamoto *et al.* [39] |

Table 2.2: Values for the $S = 2$ Haldane gap calculated by different groups.

result of $\Delta = 0.41J$ for $S = 1$, and work is converging for the $S = 2$ chains where the present published values are given in Table 2.2.

Numerical studies have also provided information on how the Haldane gap behaves as a function of magnetic field, $H$. The triplet excited state is split, and at a certain field, $H_c = \Delta$, the non-magnetic singlet is replaced by one of the magnetic states as the ground state. A detailed description of the splitting will be provided in relationship to more realistic Hamiltonians.

The VBS model prediction of $S = 1/2$ end-chain spins is really quite intriguing, and an extensive body of numerical work [18,24,30–33,40–43] has been performed to compare this model to the exact Heisenberg case. Initially, exact diagonalization [18] results demonstrated the presence of $S = 1/2$ degrees of freedom for models where $\beta$ in Equation 2.5 is varied through zero. Furthermore, Kennedy [18] applied the general result of Lieb and Mattis [44], that implies a difference between even and odd length chains, to the integer spin Heisenberg antiferromagnetic chain. More specifically, he found that the ground state of a finite chain is a four-fold degenerate ground state, made of two levels from each $S = 1/2$ end-chain spin. If an interaction along the chain is permitted between

the end-chain spins, the ground state is divided into a singlet and a triplet. In other words, for chains with even and odd numbers of spins, the singlet and the triplet are the ground states, respectively. Therefore, the chain with an odd number of spins has a magnetic ground state while the even case does not. Both exact diagonalization [18] and QMC [41] on short chains support this difference, but similar techniques on longer chains do not. Figure 2.6 shows $< S_z >$ for chains of 60, 65, and 97 units. The shortest chain was calculated by DMRG [31] and the longer chains were calculated by QMC [41]. Clearly within the size of the data points, whose size is an estimate of the uncertainty, the staggered magnetization is independent of the number of spin sites. This result is not surprising since the correlation length of 6 units is so short that any parity effects are averaged out over several correlation lengths. More directly related to experimental measurements, Yamamoto and Miyashita [24] derived information on the temperature dependent properties of end-chain spins from QMC results. By subtracting the magnetic susceptibility for chains with closed ends from open chains with odd numbers of sites, they can determine the end-chain spin contribution to the magnetic susceptibility alone. At first glance, their results are well fit by a Curie law, but a closer examination, performed by plotting $1/\chi$ vs. $T$ (Figure 2.7), suggests otherwise. Discontinuous features near $T = J$ suggest that the subtraction did not completely remove the contribution from the chain. One could argue that below $T \approx J$ the data obeys a Curie law, but this range is smaller than one decade in temperature. Therefore, a fit can not be performed to determine a definitive functional form. Nevertheless, these results are directly compared to experimental results in Chapter 6.

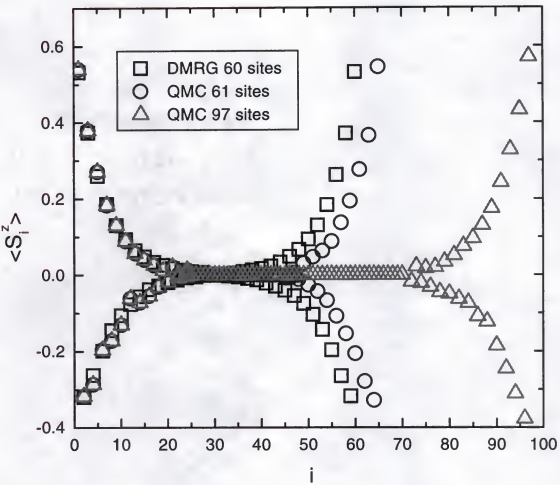


Figure 2.6: Staggered magnetization for $S = 1$ chains of 60, 65, and 97 spins. The 60 spin chain was calculated by DMRG [31], and the two longer chains were calculated by QMC [41].

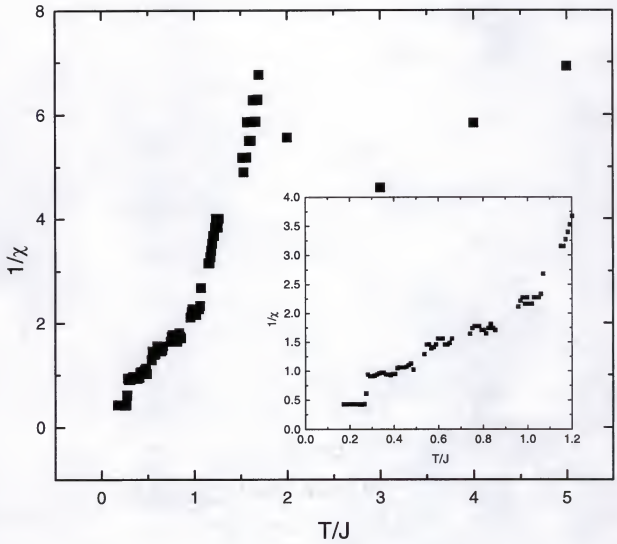


Figure 2.7: $1/\chi$ vs. $T$ for end-chain spins from QMC work of Yamamoto and Miyashita [24]. Several features suggesting non-Curie like behavior are mentioned in the text. Although, at the lowest temperatures, the inset shows reasonable agreement with a Curie-law.

### 2.3.1 Realistic Hamiltonians

The above discussion has been for systems described by Equation 2.1, but in a real system, next order terms relating to the symmetry of the environment around the magnetic ion must be considered. More specifically, the Hamiltonian should include single-ion anisotropy $D$, in some cases orthorhombic anisotropy $E$, and the degree of symmetry in the exchange $\eta$. As these terms break some of the symmetries of the system, they become very difficult to handle analytically. Nevertheless, numerical studies have revealed many properties of these systems. The Hamiltonian which takes all these effects into account is

$$\mathcal{H} = J \sum_i S_i^x S_{i+1}^x + S_i^y S_{i+1}^y + \eta S_i^z S_{i+1}^z + D(S_i^z)^2 + E\left[(S_i^x)^2 - (S_i^y)^2\right]. \quad (2.13)$$

Since $E$ is small, it is usually negligible. However, splitting in inelastic neutron scattering data [45] demonstrates that this term is measurable for NENP. The remainder of this discussion will consider $E = 0$. The best way to describe the overall behavior of Equation 2.13 is with the semi-quantitative phase diagrams [20,37,46] shown in Figures 2.8 and 2.9. First, examine the $S = 1$ case in Figure 2.8. Note that a rather large region of phase space is the Haldane phase, and the XY phase does not take over until $\eta < 0$. Two of the extreme boundaries of the phase diagram are long-range antiferromagnetic order for $\eta \gg 0$ and ferromagnetic order for $\eta \ll 0$, *i.e.* the Ising limit. If $D$ is sufficiently large, a singlet phase, which is gaped but is not the Haldane gap, develops. Finally, for the $S = 2$ case, Figure 2.9 shows a greatly reduced Haldane phase region. This result is reasonable because higher spin means more possible $\mathbf{S}$ components in

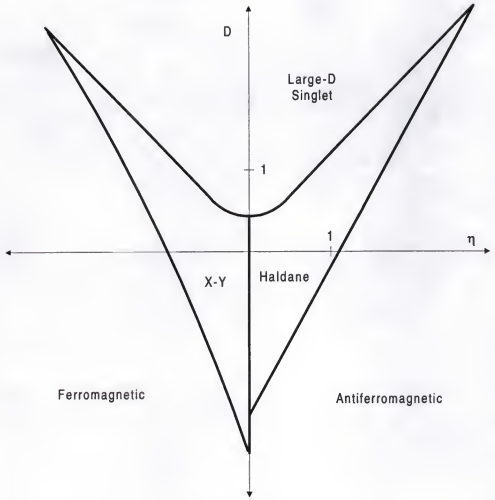


Figure 2.8: $S = 1$ phase diagram. The single-ion anisotropy vs. exchange anisotropy phase diagram for an $S = 1$ linear chain antiferromagnet described by the Hamiltonian 2.13 [20, 37, 46].

the $x$ and $y$ direction to amplify the anisotropies. Therefore, it can be said that the Haldane phase in the $S = 1$ system is lost to the XY phase as the spin is increased.

Finite values of $D$ affect antiferromagnetic chains in the Haldane phase region as well. As was stated earlier, $\Delta$ is a gap between the singlet ground state and a triplet excited state (see Figure 2.10a). A finite $D$ term splits the triplet to form two gaps (see Figure 2.10b), $\Delta_\perp$ for directions perpendicular to the chains and $\Delta_\parallel$ for directions parallel to the chains, so at $Q = \pi$, $\Delta_\perp < \Delta_\parallel$ [28, 47–50]. As $Q$ is reduced to zero, the numerical work of Golinelli *et al.* [28] shows that the dispersion curves $\perp$ and $\parallel$ to the chains cross so at $Q = 0$, $\Delta_\perp > \Delta_\parallel$. To directly compare results with several experiments (see Chapters 3, 5, and 7), extensive work [47–50] has described the magnetic field dependence of the excited states split by $D$ at $Q = \pi$. Figure 2.10c shows that the doublet splits, with the lower state moving towards, and finally crossing, the ground state at critical fields $H_{c\parallel}$ and $H_{c\perp}$, depending on the orientation of the field. The energy gaps are related to the critical fields by

$$g_\parallel \mu_B H_{c\parallel} = \Delta_\perp \tag{2.14}$$

$$g_\perp \mu_B H_{c\perp} = \sqrt{\Delta_\parallel \Delta_\perp} \tag{2.15}$$

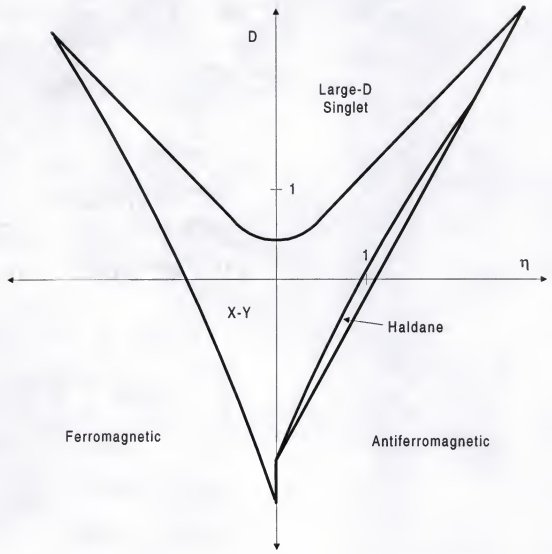


Figure 2.9: $S = 2$ phase diagram. The single-ion anisotropy vs. exchange anisotropy phase diagram for an $S = 2$ linear chain antiferromagnet for the Hamiltonian 2.13 [37].

where $g_{\|}$ and $g_{\perp}$ are the Landé g factors for each orientation [48, 50]. Then, to correlate $\Delta_{\perp}$ and $\Delta_{\|}$ with $\Delta$ and $D$, the following expressions [50, 51] are used

$$\Delta_{\|} = \Delta + 2\kappa D \tag{2.16}$$

$$\Delta_{\perp} = \Delta - \kappa D \tag{2.17}$$

where $\kappa = 1/3$ for $S = 1$ and $\kappa = 2$ for $S = 2$.

Yamamoto and Miyashita extended their QMC studies, mentioned earlier, to include finite anisotropy. At $T = 0$, their staggered magnetization results show an increased or decreased correlation length depending on if the magnetic field orientation is parallel or antiparallel to the easy axis, respectively. The easy axis is defined by the sign of $D$. Furthermore, $C_V(T)$ and $\chi(T)$ results show effects of finite $D$, but they did not fit a function to their results, making comparisons with experimental data difficult. Nevertheless, Jolicœur [51] performed high temperature series expansions to arrive at the expressions given in Appendix A. Since the expressions are expansions near a phase transition, minute errors in the fit parameters cause huge discrepancies, so the method of Padé approximants must be used for each value of $D$.

## 2.4 Measurement Theory

One challenging part of any research program is connecting the theory to experimentally measured quantities. Some less than obvious theoretical work has been used to connect the experimental technique of ESR and the above theory. This section overviews the essential theory needed to understand the measurements.

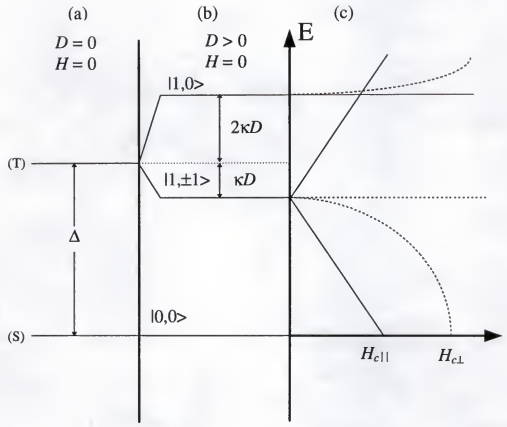


Figure 2.10: Energy level diagram showing the Haldane gap for (a) $H = 0$, $D = 0$ (b) $H = 0$, $D > 0$ (c) $H \neq 0$, $D > 0$. The values of the splitting are explained in the text. Please note that this is a generalized and corrected version of Figure 4 appearing in Reference [97].

### 2.4.1 Electron Spin Resonance

Part of this thesis reports on measurements involving end-chain spins in NINAZ. One way to detect free spins is through electron spin resonance (ESR). If a paramagnetic spin is placed in a DC magnetic field, $H$, it will align itself such that the magnetic moment of the ion precesses about $H$ in a manner similar to a toy top in the gravitational field. Since the system is a damped harmonic oscillator, the system will absorb a large amount of energy when driven at its resonance frequency, $\omega_0$. This resonant frequency is dependent on the size of the applied magnetic field as

$$\hbar\omega_0 = g\mu_B H \tag{2.18}$$

where $g$, $\hbar$ and $\mu_B$ follow their standard definitions. A convenient driving field for an electronic spin is the magnetic field component of electromagnetic radiation in the microwave (X-band) frequency regime. Several microscopic phenomena can be interpreted from the characteristics of the observed absorption peak. The area under the absorption peak is one property of interest for this thesis. Any spin resonance technique measures energy absorbed by the change in magnetization, $\Delta M$, of the sample for the oscillating field, $\Delta H$, as a function of $H$. Since $\chi$ is defined by $\frac{\Delta M}{\Delta H}$ in the limit where $\Delta H \ll H$, this technique measures the lossy component $\chi''$ of the complex magnetic susceptibility, $\chi_{AC} = \chi' + i\chi''$. Since $\chi''$ is sharply peaked near the resonance frequency, $\chi'$ can be determined at any frequency through the Kramers-Kronig relations [52–54]. Specifically, the DC magnetic susceptibility is [53]

$$\chi_{DC} = \chi'(\omega = 0) \propto \int_0^\infty \chi''(\omega')d\omega'. \tag{2.19}$$

Experimentally, ESR is performed by holding $\omega$ constant and varying $H$; therefore, by Equation 2.18, $\chi_{DC}$ becomes [54]

$$\chi_{DC} = \chi'(\omega = 0) \propto \int_0^\infty \chi''(H')dH'. \tag{2.20}$$

This result means that the area under the resonance line is simply proportional to $\chi_{DC}$ [53,54]. This completes a short introduction to the ESR technique. There are many excellent texts on ESR, if more detailed theory is required [52,53,55,56].

The above discussion has been a general overview of ESR for standard paramagnetic spins. There are several features unique to end-chain spins that are observed with ESR. Mitra, Halperin, and Affleck propose a simple model to explain the ESR response of the end-chain spins in NENP [57]. They begin by assuming chains with fixed ends which reflect a magnetic excitation back to the other end of the chain. These excitations are described by bosons in agreement with NL$\sigma$M predictions. When one of these excitations interacts with an end-chain spin, either the excitation can change energy levels or there will be a slight phase shift that would cause a small change in energy. Generally, their expression for the intensity of the ESR spectra is

$$I(\omega) = \frac{1}{4} tanh\left(\frac{\hbar\omega_0}{2k_BT}\right) e^{-z_1} 2\pi\delta\left(\omega - \omega_0\right)$$
$$+ \left(1 - e^{-\frac{\hbar\omega}{k_BT}}\right) \frac{e^{\frac{\hbar\omega_0}{2k_BT}}}{8\, cosh\left(\frac{\hbar\omega_0}{2k_BT}\right)} e^{-z_1}$$
$$\times \sum_{n,m} \left[ e^{-\frac{\epsilon_+^n}{k_BT}} 2\pi\delta\left(\omega - \omega_0 + \frac{\epsilon_+^n - \epsilon_-^m}{\hbar}\right) | < n, +|m, - > |^2 \right.$$
$$\left. + [+ \leftrightarrow -] \right] ... \qquad (2.21)$$

where the first term is the ESR line for the end-chain spin alone, and the second term includes effects resulting from interactions with the bosons. In the second term, the + indicates that the boson spin and the end-chain spin are parallel and the − indicates that they are antiparallel. Figure 2.11 shows the energy level diagram for three boson levels. The heavy solid line shows the transition corresponding to the ESR line when the bosons do not change energy levels. The thin lines show typical transitions between energy levels where the open arrows indicate transitions to higher energy levels and the filled arrows represent transitions with lower energy levels. Notice that the transitions would produce symmetric lines around the peak if the frequency of the microwaves is large enough to see the transition at lower fields. Nevertheless, the higher field transition should always be observable if a sufficient magnetic field is applied to the sample. The processes where the end-chain spin does not flip are forbidden transitions. If the boson changes energy levels, then the change in energy for a chain of length, $L$, is

$$\epsilon_+^n - \epsilon_-^m = \delta\epsilon \approx \frac{(\hbar\pi c)^2}{2\Delta L^2} \qquad (2.22)$$

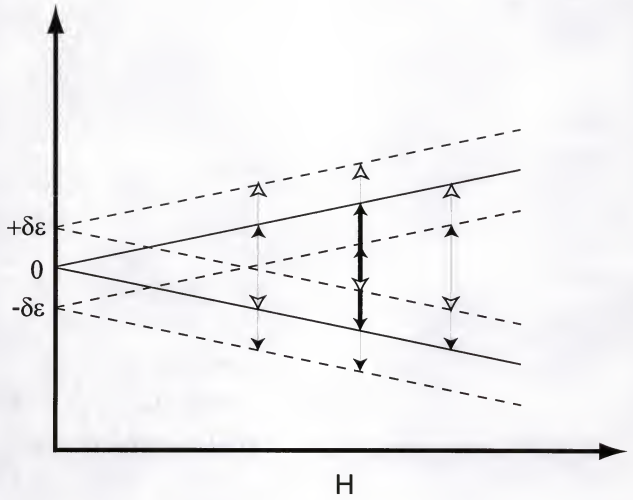


Figure 2.11: Allowed transitions between end-chain spin states. Energy level diagram showing the allowed transitions that should be observed in ESR. Each transition is signified as a line with an arrow on each end. The heavy line signifies a resonance signal where a boson does not change energy levels. The open ended arrows indicate transitions with a higher boson energy level and the closed arrows signify transitions with a lower boson energy level. All arrows are of a length $E = \hbar\omega_0 = \text{constant}$.

where $c$ is the spin wave velocity. If $L$ is too short (*e.g.* $\sim$ 100 spins for NENP), the side peaks are not within the observation limits of the typical X-band ($\nu = 9$ GHz) ESR experiment. Therefore, to calculate the intensity of the ESR line, the second term in Equation 2.21 can be neglected. Therefore, the chains that significantly contribute to the central intensity are those without bosons on them. Since the probability of a magnetic excitation existing on a chain at any one time is an exponential function of temperature, the number or spins participating in the ESR line is temperature dependent. As a result, the ESR line intensity increases faster than a Curie law with decreasing temperature. The temperature dependence of these intermediate length chains is given by

$$I(T) = I_0 \, tanh\left(\frac{\hbar\omega_0}{2k_BT}\right) e^{-<Z_1>} \tag{2.23}$$

where $< Z_1 >$ is the partition function averaged over the distribution of chain lengths as given by

$$Z_1 = \left[\frac{< L >}{\pi^{1/2}\lambda_T} - 1\right] e^{-\frac{\Delta}{k_BT}}. \tag{2.24}$$

The de Broglie thermal wavelength of a boson is

$$\lambda_T = \hbar c \left[\frac{1}{2\Delta k_BT}\right]^{1/2}. \tag{2.25}$$

Mitra, Halperin and Affleck [57] finish their calculation by assuming a distribution of $P(L) \propto exp(-L/L_0)$ with a cutoff of $L_{min}$. This distribution provides the analytical solution

$$I(T) = I_0 \, tanh\left(\frac{\hbar\omega_0}{2k_B T}\right) \frac{exp\left[-\left(\pi^{-1/2} L_{min} \lambda_T^{-1} - 1\right) e^{-\frac{\Delta}{k_B T}}\right]}{1 + \pi^{-1/2} L_0 \lambda_T^{-1} e^{-\frac{\Delta}{k_B T}}}. \tag{2.26}$$

Calculating other quantities for the ESR end-chain spin is less trivial because the second term in Equation 2.21 contributes to the line width of the central peak even when the boson does not change energy levels. To approximate the line width, consider the potential that a boson sees as it traverses the chain. At distances far away from an end-chain spin, the potential is essentially flat, but as the boson approaches an end-chain spin, it sees a finite potential, and therefore, its wave vector shifts slightly. This shift of the boson's wave vector can be characterized by a phase shift $\delta(k)$ defined by

$$k = \frac{n\pi}{L} - \frac{\delta(k)}{L}. \tag{2.27}$$

To parameterize this effect, Mitra, Halperin, and Affleck used the expression

$$\delta(k) \approx \mathcal{D} k \xi, \tag{2.28}$$

where $\mathcal{D}$ is a constant of order 1. In their paper, they conclude that this effect is not observable because the line width would be controlled by the very short chains in the sample. It is important to recall that their discussion focused only on NENP where several phenomena (*i.e.* staggered magnetization and thermally excited bosons) could effect the linewidth. For this thesis, we will apply this analysis to NINAZ where there is no staggered magnetization and $J$ is large enough that the quantum limit is easily accessible. The line widths in NINAZ are consistent with this phase shift, see Chapter 6.

# CHAPTER 3
# REVIEW OF EXPERIMENTAL STUDIES

This chapter reviews the status of experimental studies of phenomena related to the Haldane state. The main emphasis is placed on materials that are not part of this thesis since these systems will be discussed in their own chapters. This chapter begins with a discussion of the material properties of Haldane gap systems. Next, a discussion of the different techniques used to measure the Haldane gap, and other information gained by these methods, will be given. Third, experimental results from the study of end-chain spins will be provided. To complete the review, a few relevant subtopics will be discussed.

## 3.1 Haldane Gap Materials

In order to study the phenomena related to the Haldane state, materials are needed which are closely approximated by the theoretical model. There are two main properties that must be met for a material to exhibit a Haldane gap. Firstly, the system must have a coupling along the chains much stronger than a coupling between the chains so the material exhibits 1-D behavior. Secondly, any anisotropies, that give the spins a preferential orientation (*i.e.* single-ion anisotropy or exchange anisotropy), must be small enough so the material remains in the Haldane phase, see Figures 2.8 and 2.9. The first part of this section

discusses issues related to fabricating antiferromagnetic chain materials and the second part deals with the anisotropy.

Materials that provide a realization of integer spin antiferromagnetic chains have been available for several decades [58]. Chemically these systems are characterized by their composition as being either metal-organic compounds or purely inorganic compounds. For both groups of materials, each metal ion has strong $\sim 180^o$ bond overlap with the bridging ligand that mediates the superexchange along the chain. Bond angles near $180^o$ are characteristic of antiferromagnetic compounds since the strength of the superexchange is controlled by the bond angle [54, 59]. There are two ways that the chains are separated from each other. For some materials, the chains have a slight net positive charge which is balanced by a counter ion between the chains. Therefore, no bond overlap exists to provide a superexchange pathway between chains. Thus, only dipolar interactions magnetically couple the chains. The other class of chain materials relies on the contrast between strong antiferromagnetic bonds along the direction of the chain and very weak $90^o$ bonds, ferromagnetic in nature, between the chains. Both types of materials posses an interchain coupling that is four orders of magnitude smaller than the intrachain coupling. The local environment around the magnetic ion determines the anisotropy of the chain material. Generally, if chemical bonds are uniformly distributed around the magnetic ion, the anisotropy is low. However, completely isotropic bonding is rare because Jahn-Teller distortions favor at least some slight anisotropy. Fortunately, there are many materials where

| material | S | J | D/J | E/J | $\Delta$ | references |
|---|---|---|---|---|---|---|
| | | (K) | | | (K) | |
| $CsNiCl_3$ | 1 | 16.6 | 0.003 | | 5.25 | [60] |
| NENP | 1 | $46 \pm 2$ | $0.18 \pm 0.01$ | $0.02 \pm 0.01$ | 14 | [22, 45, 61–70] |
| NINO | 1 | 47 | 0.34 | 0.03 | 9.81 | [62, 65] |
| TMNIN | 1 | 10 | 0.003 | | 3 | [71–77] |
| $AgVP_2S_6$ | 1 | 400 | 0.01 | $\leq 3 \times 10^{-4}$ | 300 | [62, 78–80] |
| NINAZ | 1 | 125 | 0.16 | | 41.9 | [73, 77, 81–83] |
| $NiC_2O_4$·2MIz | 1 | 39.7 | | | 20.3 | [84] |
| $NiC_2O_4$·2DMIz | 1 | 42.9 | | | 19.0 | [84] |
| $Y_2BaNiO_5$ | 1 | 285 | 0.16 | | 100 | [85–94] |
| $MnCl_3$(bipy) | 2 | 35 | $0.010 \pm 0.003$ | | $2.3 \pm 0.8$ | [95–97] |

Table 3.1: The Haldane gap materials and their properties. The parameters that describe each system are the intrachain exchange, $J$, the single-ion anisotropy, $D$, the orthorhombic anisotropy, $E$, and the Haldane Gap, $\Delta$. The empty spaces indicate that the parameter has not been experimentally determined. Note that $CsNiCl_3$ has a transition to an antiferromagnetic long-range ordered state at $T_N = 4.6$ K.

the bonds are sufficiently isotropic for the Haldane phase to be realized, as seen by Table 3.1.

## 3.2 Experimental Tests of the Haldane Gap

A large portion of this thesis is concerned with measurement of the Haldane gap, and this section overviews experimental tests of this state. The macroscopic magnetic susceptibility is usually the first property tested for a new 1-D antiferromagnetic material. The standard SQUID magnetometer has sufficient sensitivity to test for undesired magnetic properties, *i.e.* long-range order or gross impurities, even in very small samples ($\sim$ 10 mg). Such tests are necessary to determine if the system merits further exploration. All of the samples in Table 3.1

display, with decreasing temperature, a broad peak, demonstrating 1-D antiferromagnetism, followed by a sharp decrease, consistent with an activated gap. In addition, many materials display a low temperature paramagnetic tail consistent with either end-chain spins or impurities in the sample. Another macroscopic measurement, better suited to measure the size of the Haldane gap, is the magnetic field, $H$, dependent magnetization, $M$, at a temperature well below the gap. While the material is in the Haldane state, the magnetization is zero, and as $H$ is increased such that the lower branch of the triplet excited state crosses the ground state (Figure 2.10), a finite magnetization develops. This technique has been used in many of the materials [63,64,75,97]. The experiments in TMNIN and $MnCl_3$(bipy), as part of this thesis, will be discussed in Chapters 5 and 7, respectively. The first $M$ vs. $H$ measurement to identify the Haldane gap was performed on NENP [63,64]. As can be seen in Figure 3.1, there are critical fields defined by the intersection of a constant, weakly magnetic state with an increasing magnetic state. These critical fields provide values of the Haldane gap, $\Delta$, and the single-ion anisotropy, $D$, consistent with the values given in Table 3.1. Notice that for a magnetic field oriented parallel to the $a$ axis ($b$ is the chain axis), a finite magnetization was observed below the gap. Katsumata *et al.* [63] attributed this property to impurities. Subsequent NMR [98] and high field ESR measurements [19,99,100] show that it results from non-equivalent magnetic sites as will be discussed in Section 3.4.

Though macroscopic measurements can detect the presence of a gap and their careful use can eliminate any possibility of other physical processes opening a gap,

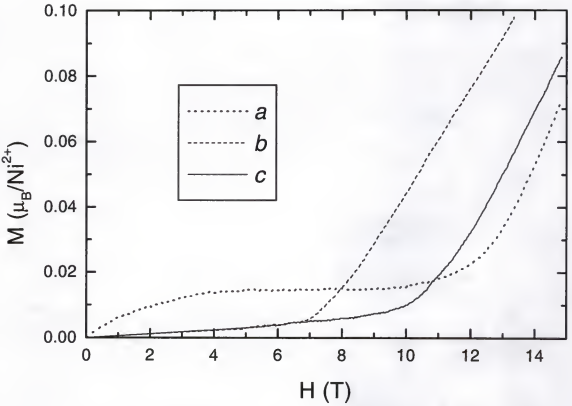


Figure 3.1: $M(H)$ for NENP. There are clearly defined critical fields for all three orientations. The finite magnetization for $H \parallel a$ results from a staggered magnetization of the Ni sites. The data are from Reference [63].

a direct measure of the gap is needed to test additional properties. Inelastic neutron scattering is the probe most often used and has had great success. The general idea behind inelastic neutron scattering is to measure the energy and momentum change for neutrons after they have scattered from the sample. Since the Haldane gap is a low temperature phenomenon, any energy and momentum changes by phonons are negligible. Therefore, all energy and momentum changes correspond to the creation or annihilation of magnetic excitations. When neutrons of the energy equivalent to the gap at a certain value of $Q$ are sent into the sample, the neutrons excite the system over the Haldane gap, producing resonant scattering. For neutron energies below the gap, the system is not excited, so magnetic scattering is not observed. When energies above the gap are measured, the magnetic scattering is not observed. Furthermore, neutron scattering is a $Q$ dependent measurement. Therefore, by taking energy sweeps at different values of $Q$, the dispersion can be measured. As an example, Figure 3.1 shows the magnetic neutron scattering near $Q = \pi$ corresponding to a Haldane gap in $Y_2BaNiO_5$ [90]. The most prominent feature, *i.e.* the peak around zero energy, originates from incoherent elastic scattering, and this feature is always observed.

The first unambiguous measurement of the Haldane gap was in NENP by Renard *et al.* [61] from which $\Delta$ and $D$ could be determined. Later measurements [45], with better resolution, were able to determine $E$ as well. Near $Q = \pi$, several measurements have determined the dispersion. Two groups [45, 67] measured the dispersion for a larger range of $Q$, but the scattering intensity decreased rapidly below $Q = 0.3$, so the $Q = 0$ gap of $2\Delta$ has eluded confirmation.

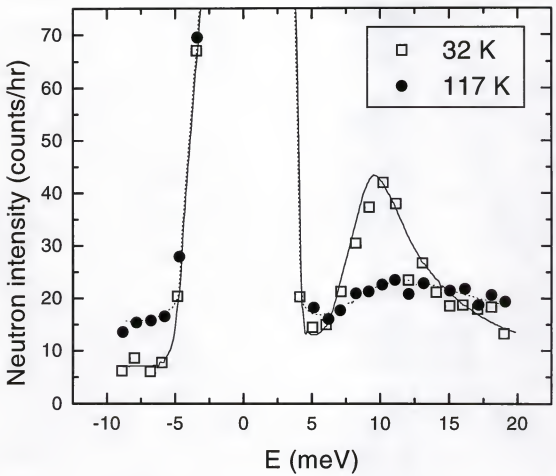


Figure 3.2: Inelastic neutron scattering intensity for $Y_2BaNiO_5$. Constant $Q \approx \pi$ scan showing the peak due to incoherent elastic scattering and the peak resulting from the Haldane gap for $T > \Delta$ and $T < \Delta$. The data are from [90].

Nevertheless, this loss of scattering intensity for decreasing $Q$ is consistent with the model of a two particle continuum near $Q = 0$ [26]. In addition, these experiments do not have sufficient resolution to observe the crossing of the $\Delta_{\|}$ and $\Delta_{\perp}$ components of the dispersion [28]. Nevertheless, the empirically determined dispersion agrees with the QMC predictions of Takahashi [26].

NMR is another microscopic probe useful to test for the existence of the Haldane gap. Of course, if the gap is present, additional information can be obtained. Since the purpose of this chapter is to demonstrate how NMR is used for probing the Haldane gap, only spin-lattice relaxation times and the Knight shift will be discussed. In an NMR experiment, a uniform magnetic field is applied to a sample, resulting in the precession of the nuclear spins. When an rf pulse is applied to the sample to flip the nuclear spins, the local magnetic environment affects how long it takes for the spin to return to equilibrium. The contribution to this relaxation time by the crystal lattice is known as the spin-lattice relaxation time, $T_1$. In magnetic systems, where the electronic moments are large and long-ranged (compared to the nuclear moments), $T_1$ is the dominant relaxation process. Clearly $T_1$ is related to how correlated the local moments are with each other or, in other words, are related to the spin-spin correlation function. Since the experiment is performed in frequency space, the Fourier transform of the correlation function, or the dynamic structure factor $S(q, \omega)$, is the quantity measured. It has been shown [10, 12, 101, 102] that

$$\frac{1}{T_1} \propto S(q, \omega) \propto e^{-\frac{\Delta}{T}} \tag{3.1}$$

for $T \ll \Delta$. Therefore, the slope of a $ln(T_1^{-1})$ vs. $T^{-1}$ plot of the data provides a microscopic measure of $\Delta$. If the sample has conduction electrons, the Knight shift can be measured as well. This effect is a shift in frequency of the resonance line due to the nuclei observing a background of mobile spin polarized electrons. A detailed discussion [53] shows that the Knight shift is proportional to the local spin susceptibility of the sample. Therefore, it is a microscopic measure of the magnetic susceptibility of the chain.

Since there are numerous hydrogen atoms in typical organo-metallic compounds, proton NMR is often performed. Several groups [66, 69, 103, 104] have measured the proton spin-lattice relaxation time in NENP, and all of their results are consistent with Equation 3.1. Nevertheless, these proton sites are somewhat removed from the magnetic nickel site. To use a probe closer to this site, Reyes *et al.* [102] performed NMR using the naturally abundant $^{13}C$ of NENP. Besides measuring the gap, they also observed features in $T_1^{-1}(T)$ that are absent in the proton NMR data [66,69,103,104]. These observed features may be interpreted by adding a temperature dependent gap to the standard analysis. In $AgVP_2S_6$, $^{51}V$ and $^{31}P$ were used as probing nuclei, whereas $^{89}Y$ was used in $Y_2BaNiO_5$ [105]. In addition, both of these samples possess conduction electrons, so the Knight shift was the measured quantity. Since the Knight shift measures the local magnetic susceptibility, any end-chain spin effect is negligible, and it is a good measure of the chain contribution alone. Takigawa *et al.* [80] fit their Knight shift data for $AgVP_2S_6$ with the expressions of Jolicœur *et al.* [10] which produced gap values consistent with the inelastic neutron scattering results [79]. Furthermore, by

examining the orientational dependence of the Knight shift, they measured $D$ and found an upper bound on $E$. Similar techniques were applied to $Y_2BaNiO_5$ [105], but these workers interpreted their results as being inconsistent with the energy level diagram including anisotropy as described by theory [47, 48].

Finally, ESR has been used to examine the microscopic magnetic susceptibility and to map out portions of the energy-magnetic field diagram. As explained in Section 2.4.1, the area under the ESR absorption curve is proportional to the static magnetic susceptibility. Unfortunately, as antiferromagnetic correlations increase, the ESR line broadens and loses intensity, resulting in a loss of resolution. Therefore, if conduction electrons exist in the system, the NMR Knight shift is a better probe of the local magnetic susceptibility because the NMR line is not degraded by the antiferromagnetic correlations. Nevertheless, in the organo-metallic compounds, there are no conduction electrons, so there is no NMR Knight shift. Since an ESR line is the result of the resonant absorption of energy between two states split by the magnetic field, high field ESR has been an effective tool for mapping out the energy vs. magnetic field diagram. This experimentally determined diagram has confirmed the theory used to assign critical fields in $M$ vs. $H$ experiments.

Date and Kindo [65] measured the ESR line at a frequency of 47 GHz as a function of temperature in NENP and NINO. They found that the area under the absorption curve as a function of temperature fits the expected magnetic susceptibility with the exponential activation. Recent measurements have been performed on $Y_2BaNiO_5$ [106] with similar results. Several groups have examined

the energy-magnetic field diagram using ESR [19, 99, 100, 107]. These results for both NENP and NINO are consistent with the theory for finite anisotropy [47,48], assuming a staggered magnetic field is considered in the analysis. Discussion of the staggered magnetic field is given below.

## 3.3 Studies of End-chain Spins

The other main topic of this thesis involves the properties of end-chain spins, and therefore, this section will provide an overview of the research of other workers. As predicted by the VBS model [13,14] described in Section 2.1.2, the spin value at the termination of a chain is expected to be one half the value of a spin site. To test this prediction, finite chains are needed. The first and most predominant way of breaking the chains was by doping the materials. Initial evidence of the presence of end-chain spins was an enhanced impurity tail in the magnetic susceptibility of NENP doped with $Cu^{2+}$ magnetic impurities [62]. Later, using X-band ESR on a similar sample, Hagiwara *et al.* [108] observed hyperfine interactions that could be attributed to the interaction between $S = 1/2$ variables and the $Cu^{2+}$ $S = 1/2$ impurities. Furthermore, the temperature dependence of the ESR peak, *i.e.* the peak attributable to the end-chain spins, was fit with an empirical equation whose form was later confirmed by Mitra *et al.* [57]. To study an even simpler system by avoiding magnetic impurities, Glarum *et al.* [109] studied samples of NENP doped with Cd, Zn, and Hg. These workers observed a single asymmetric ESR peak, and this asymmetry was attributed to the staggered magnetization present in the sample. Ajiro *et al.* [110] recently extended this

work with a detailed study of the same system. All of the samples mentioned so far in this section were lightly doped, but heavily doped samples exhibited Curie tails [111] that increased faster than if each dopant caused only one chain break. Several possible explanations of this effect have been tested in different ways. First, NENP does not have a non-magnetic isomorph, so naturally, beyond a certain doping level, the sample being doped is not necessarily NENP. To avoid these problems, primarily two materials have been tested, $NiC_2O_4 \cdot 2DMIZ$ [112] and $Y_2BaNiO_5$ [91, 113].

The sample $NiC_2O_4 \cdot 2DMIZ$ is isomorphically related to $ZnC_2O_4 \cdot 2DMIZ$. Therefore, Zn dopants in $NiC_2O_4 \cdot 2DMIZ$ should enter the crystal uniformly. Nevertheless, magnetic susceptibility measurements reveal paramagnetic tails that increase faster than is consistent with the doping level [114]. Kikuchi *et al.* [114] explain these variations in terms of an energy gap between states inside the Haldane gap. They explain the existence of states in the gap as resulting from interactions, mediated through chain, between end-chain spins as described by the numerical work of Yamomoto and Miyashita [24]. Nevertheless, their chains are too long to observe in-gap states, and the simple explanation may be that the Zn dopants are not entering the crystal uniformly. Careful X-ray studies are needed to test the Zn distribution in the crystal. Furthermore, the analysis has neglected any change in the magnetic susceptibility due to the interaction of the end-chain spins with magnetic excitations.

The material $Y_2BaNiO_5$ can be doped in two ways: either Zn can replace the Ni, generating chain breaks, or Ca can replace the Ba, creating weak bonds

and charge carrying holes [91, 113]. Furthermore, extensive X-ray and electron scattering studies [88] of doped samples have demonstrated that $Y_2BaNiO_5$ can be uniformly doped. Ramirez *et al.* measured the specific heat of a Zn doped powder sample and observed a Schottky anomaly consistent with the presence of $S = 1$ end-chain spins. They attributed this effect to differences between chains with odd and even numbers of sites. Once again, these workers have ignored any effect of the interactions between the magnetic excitations on the chains and the end-chain spins. However, the temperature dependence of the ESR signal intensity in NENP [108–110], TMNIN [115], and NINAZ (Section 6.3.4 of this thesis) suggests that these interactions should be considered. In addition, recent work by Kimura *et al.* [106] shows ESR lines consistent with chain breaks caused by $Ni^{3+}$ ions which act as $S = 1/2$ impurities between two $S = 1/2$ end-chain spins, and this situation is similar to the $Cu^{2+}$ work in NENP [108]. The final evidence that interactions between magnetic excitations on the chains and the end-chain spins correctly explain the behavior of Zn doped $Y_2BaNiO_5$ is provided by theoretical work of Hallberg *et al.* [116] that reconciles the specific heat results in $Y_2BaNiO_5$ with ESR results in NENP. DiTusa *et al.* [91] concentrated on the Ca doped samples which exhibited a greatly reduced resistivity which is consistent with the assertion that this material is a 1-D metal. More importantly, inelastic neutron scattering measurements revealed magnetic scattering inside the Haldane gap for the Ca doped samples but not for the Zn doped samples. Dagotto *et al.* [117] theoretically illuminated these observations by qualitatively describing the in-gap states as resulting from coupling between the mobile holes and the $S = 1$ Ni sites.

There are other ways to observe end-chain spins besides breaking chains with dopants. Two methods have been tried, the first will be discussed here and the second will be discussed in Chapter 6. The first method does not involve creating chain breaks, but rather measures the end-chain spins already present in the sample from crystal imperfections. Hagiwara and Katsumata [118] performed ESR and magnetization experiments on a quickly grown sample of NENP. Their results are consistent with the existence $S = 1/2$ end-chain spins. However, when compared to samples grown by other groups, this sample has an enormous number of natural chain breaks. Therefore, a study should be performed on how crystal growth rate affects the number of crystal imperfections. A traditionally grown sample was used for the experimental *tour de force* of measuring the magnetic susceptibility over six orders of magnitude in temperature space as shown in Figure 3.3 [119, 120]. Three separate experimental apparatuses were used to map out three regions of temperature space: a SQUID magnetometer for 300 K $> T >$ 4 K, a mutual inductance coil cooled by a homemade dilution refrigerator for 4 K $> T >$ 50 mK, and an AC SQUID susceptometer cooled by the Cu nuclear demagnetization stage of cryostat number 1 at the University of Florida Microkelvin Facility for 50 mK $> T >$ 400 $\mu$K. The portion of Figure 3.3 related to the end-chain spin discussion is the paramagnetic tail observed below $\sim$ 200 mK. This tail has a Curie constant consistent with the natural chain length expected for the material [119, 120].

Since the main topics of this thesis are $S = 2$ Haldane gap materials and end-chain spin effects in NINAZ, an $S = 1$ material, it would be amiss not to mention

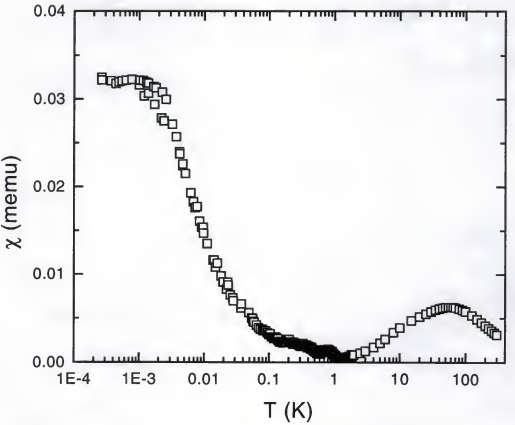


Figure 3.3: $\chi(400\,\mu\mathrm{K} < T < 300\,\mathrm{K})$ for pure NENP. The data are from References [119,120].

the first evidence for free $S = 1$ end-chain spins in an $S = 2$ material. Yamazaki and Katsumata [121] used ESR, magnetic susceptibility, and heat capacity to study end-chain spins in $CsCrCl_3$ doped with Mg. This material possesses long-range magnetic order below 16 K, so one of their points was that the presence of $S = 1$ end-chain spins constituted the existence of the Haldane state.

Measurements of NINO, NINAZ, and TMNIN have also been performed to study end-chain spins. The techniques used in NINO [125] are similar to those discussed above, and the discussion of NINAZ and TMNIN will be given elsewhere in this thesis.

## 3.4 Other Experimental Results

Two other topics that have been addressed experimentally must be mentioned. First, the differing magnetic sites in NENP and NINO will be discussed because a similar phenomena might explain unresolved issues in TMNIN and $MnCl_3$(bipy). The existence of two different magnetic sites might relate to a small anomaly in the magnetic susceptibility in $MnCl_3$(bipy) [97]. Both NENP and NINO consist of Ni sites bridged by an $NO_2$ group. For a specific Ni site, the exchange path is directed through the nitrogen and one oxygen of the $NO_2$ group on one side of the Ni. On the other side of the Ni, the exchange path is directed through the other oxygen of the $NO_2$ group (see Figure 3.4). This asymmetric bonding causes a slight shift in the magnetization of each site. As a consequence, neighboring Ni sites differ slightly in their transverse magnetization. The existence of these differing magnetic sites is necessary to explain the NMR line shape of

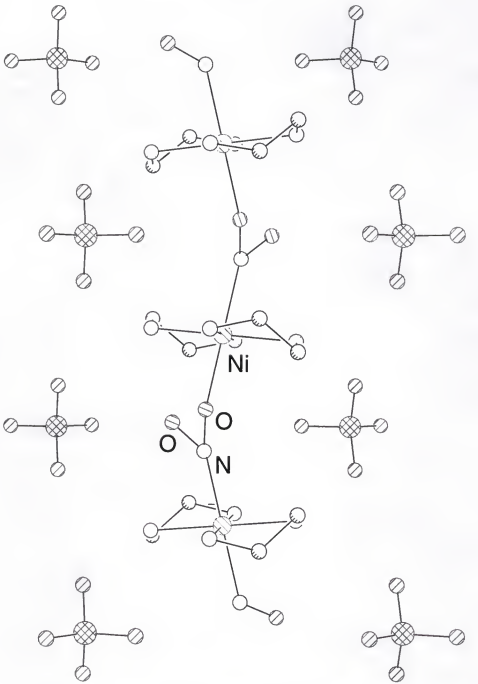


Figure 3.4: The crystal structure of NENP. Notice the different oxygen sites which bridge the Ni [22].

Chiba *et al.* [98]. This property also explains the finite magnetization observed below the critical field in $M$ vs. $H$ measurements [63,64] and explains the shape of the magnetic field diagram as measured by ESR [19,99,100,107].

The second topic of discussion is the coexistence of the Haldane gap and three-dimensional long-range order. Since this topic is historically significant but is far afield from the topic of this thesis, only the materials and the references will be mentioned. The first material to exhibit evidence of a Haldane gap was $CsNiCl_3$ [60], but with a gap of 5 K and a Néel temperature of 4.4 K, this assignment was disputed in the literature [122–124]. Nevertheless, this material provided an environment to study the coexistence of the Haldane gap and three-dimensional long-range order [126]. To provide a smooth transition to materials with three-dimensional long-range order, extensive work has been done on $R_2BaNiO_5$, where R=Y, Nd, Pr or some doping mix of Y and Nd. The pure Pr [127] and Nd [128–130] compounds have magnetically ordered ground states, and the doped materials [131] allow a variation of the interchain interaction.

Another technique to force interactions between the samples is to apply pressure. Recent inelastic neutron scattering measurements reveal a reduced single-ion anisotropy in NENP under a pressure of 2.5 GPa [132]. Furthermore, heat capacity measurements in NENP are consistent with an increase in $\Delta$ with increased pressure [133]. Nevertheless, pressure studies have been unable to increase the interchain exchange enough to cause the sample to exhibit long-range magnetic order.

# CHAPTER 4
# EXPERIMENTAL MEASUREMENT TECHNIQUES

This chapter describes the experimental techniques used to study the materials described in this thesis. Magnetometry using SQUID and cantilever magnetometers is discussed first. Next, both high field and X-band ESR are discussed because they provided a microscopic probe of the end-chain spins. The third major technique to be reviewed is neutron scattering. I have used both powder neutron diffraction analyzed by Reitveld refinement to obtain low temperature crystal structures and inelastic neutron data collected by time of flight methods to look for the characteristic features of the Haldane gap in $MnCl_3$(bipy). Finally, I will discuss several measurement techniques used in the creation and analysis of our pulverized NINAZ samples.

## 4.1 SQUID Magnetometer

A SQUID magnetometer is a sensitive device for measuring the magnetization of a sample over a range of magnetic fields and temperatures. In addition, knowledge of the applied magnetic field allows the DC magnetic susceptibility to be determined as well. Professor J. R. Childress, of the Department of Materials Science and Engineering at the University of Florida, kindly allowed us to use his MPMS SQUID magnetometer, made by Quantum Design, for magnetization and magnetic susceptibility measurements. The main component of this SQUID

magnetometer is an rf SQUID. A SQUID is a small superconducting ring with a weak link. As magnetic flux is applied to a SQUID, a supercurrent is induced in the ring to cancel the flux until the phase of the electron wave function matches across the weak link. Once this happens, a flux quanta enters the loop and the supercurrent goes to zero. If the flux keeps increasing, the supercurrent increases again until another flux quanta enters the SQUID. In the magnetometer, an rf signal on top of an applied flux provides a changing flux in the SQUID with a bias such that the system oscillates about the point where one flux quanta enters the ring. As the flux from the sample changes, a feed back loop controls the bias flux, canceling the flux from the sample, so the SQUID remains near the one flux quanta point. The flux needed to keep the SQUID at this point is proportional to the flux from the sample. Therefore, a calibration will provide a measure of the magnetization. The particularly challenging part about making a practical device work in a magnetic field is ensuring that the SQUID measures the flux change of the sample and not of the magnet. Quantum Design conquers this challenge by coupling the SQUID, which is outside and shielded from the superconducting magnet, to the sample through a flux transformer that measures the second field gradient of the sample [134]. Thus, a signal is only observed in the SQUID when $dm^2/dx^2$ is non-zero. The second derivative is chosen over the first derivative in order to eliminate noise arising from slow drifts in the magnetic field. Recovery of the sample magnetization is accomplished by moving the sample through the gradient coils in a manner to doubly integrate the signal. This motion requires exact positioning which is accomplished through the use of a

stepper motor and through initial positioning of the sample. Detailed discussion of the physics behind a SQUID are beyond the scope of this thesis, for a brief overview see Reference [135].

The samples were mounted in standard number 4 or number 5 gelatin capsules (gel-cap) that were held inside a plastic straw. Depending on the sample, different mounting arrangements were used. If the sample was a single crystal or an aligned single crystal packet, it was placed in the gel-cap and oriented in the desired direction with respect to the magnetic field. Small pieces of gel-cap were used to secure the sample. If the sample was a powder, it was poured into the larger diameter portion of the gel-cap, and the smaller diameter portion was inverted and used to press the sample, thereby stabilizing its position. Usually $\sim 50$ mg of sample was measured to provide a signal well above the background, although samples as small as $\sim 2$ mg were successfully measured. Several arrangements of this type have been measured *sans* sample to determine the background contribution of the gel-cap and straw. A typical $H = 0.1$ T background is shown in Figure 4.1, along with fits for three temperature regions. The expressions for the three temperature regions are given by

$$M(T) = \begin{cases} -1.221793 \times 10^{-5} + \frac{1.2534219 \times 10^{-5}}{0.1091171 + T} \\ -1.8067205 \times 10^{-8} T & 2\,\mathrm{K} < T < 40\,\mathrm{K} \\ \\ 1.2156003 \times 10^{-5} - 1.6642177 \times 10^{-8} T \\ +1.5027333 \times 10^{-10} T^2 - 6.5003915 \times 10^{-13} T^3 \\ +7.1854421 \times 10^{-14} T^4 & 40\,\mathrm{K} < T < 200\,\mathrm{K} \\ \\ -1.423403 \times 10^{-4} + 2.0092364 \times 10^{-6} T \\ -1.1421511 \times 10^{-8} T^2 + 2.7916376 \times 10^{-11} T^3 \\ -2.4700249 \times 10^{-14} T^4 & 200\,\mathrm{K} < T < 380\,\mathrm{K}. \end{cases} \tag{4.1}$$

Similarly, Figure 4.2 shows the background for magnetic field sweeps at $T = 2$ K with the fit curve given by

$$M(H) = -3.5256 \times 10^{-5} H - 4.3195 \times 10^{-5} H^2 + 9.0369 \times 10^{-6} H^3 \\ -6.8631 \times 10^{9} H^4 \tag{4.2}$$

where $H$ is in units of Tesla. Clearly, the background shows the expected diamagnetism and, at the lowest temperatures, a tail showing the presence of some free spins. Nevertheless, the contributions are on the order of 10 $\mu$emu, which is negligible when compared to the magnetic response of most samples. Several specimens consisted of a conglomeration of aligned single crystals that were glued together with fingernail polish on a piece of weighing paper. To check the background, similar quantities of weighing paper and fingernail polish were placed

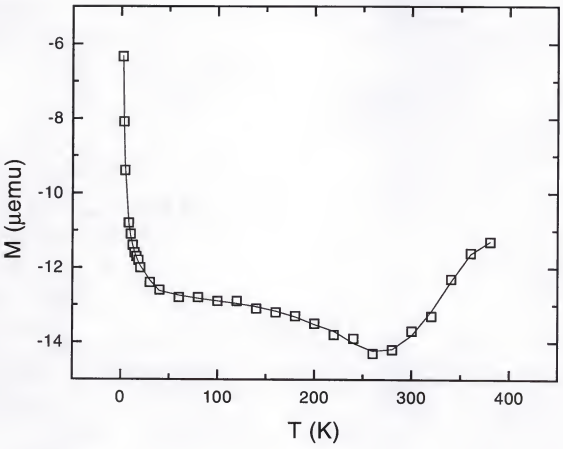


Figure 4.1: $M(T)$ SQUID background for an empty gel-cap and straw in $H = 0.1$ T. The solid lines are fits given by Equation 4.1.

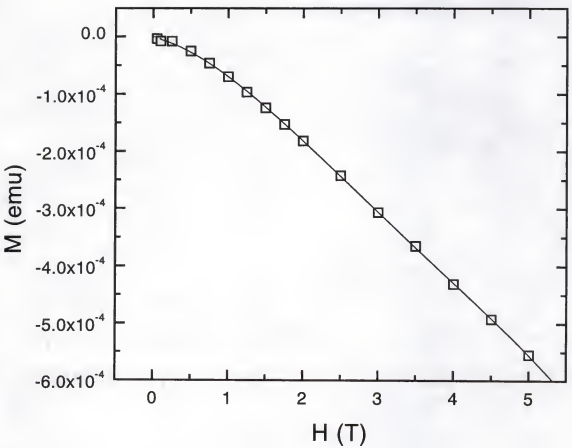


Figure 4.2: $M$(H) SQUID background for an empty gel-cap and straw at $T = 2$ K. The solid line is the fit given in Equation 4.2.

in a gel-cap. This control was then measured, and the resultant background subtracted from the corresponding data.

## 4.2 Cantilever Magnetometer

The cantilever was developed by Chaparala *et al.* [136] to provide a sensitive magnetometer at high magnetic fields, and it is capable of simultaneously measuring transport properties. The operational technique was refined at the National High Magnetic Field Laboratory partly through our measurements as will be discussed in later chapters. The result of this instrumental improvement is the cantilever magnetometer commercially available from Oxford Instruments. A schematic diagram of the cantilever is shown in Figure 4.3. There are several features to observe. The four leads down the middle are used if transport measurements are desired along with magnetic measurements. To each side of the transport leads, other leads form two square loops, which can be used for calibration if absolute magnetization units are required. The sample is mounted between the two loops, as shown in the figure. Not shown is the bottom of the cantilever where a gold plate forms one half of a capacitor. The other half is a plate fixed below the cantilever. The experimental quantity measured is the capacitance between the two plates. Typically, the sample was attached to the cantilever with a small quantity of vacuum grease. This grease has a diamagnetic background which may need to be subtracted. The determination and removal of this background will be discussed later with the experimental results.

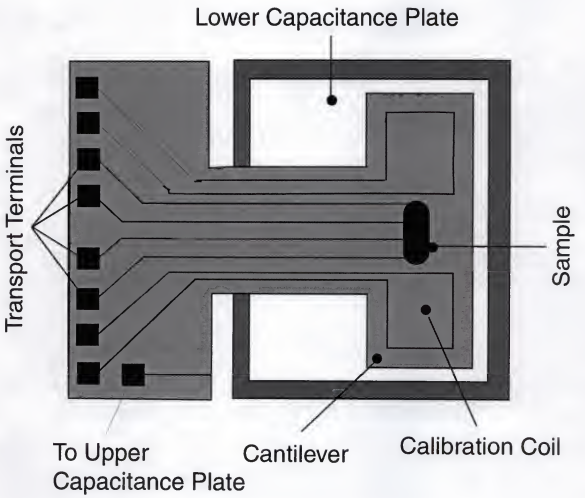


Figure 4.3: Cantilever magnetometer diagram. This figure is adapted from [137].

The cantilever can work either in force mode or in torque mode. Only the force mode will be discussed here because a discussion of the torque mode [136] is beyond the scope of this thesis. For the force mode of operation, the plane of the cantilever is positioned perpendicular to $H$. The force on a magnetic sample, $F$, in a magnetic field gradient, $\nabla H$, is proportional to $M\nabla H$. Since the sample is affixed to the cantilever, both items experience the same force. Following Hook's law, the cantilever opposes $F$ with a force proportional to the amount it bends, causing the distance $x$ between the plates to change by a quantity $\Delta x$. This change causes the capacitance, $C$, to change by an amount $\Delta C$. Therefore, any change in the force may follow from $\Delta F \propto \Delta x \propto \Delta C$. In other words, by knowing $\Delta C$, the change in the force on the cantilever is known to within a calibration constant. Furthermore, since $\nabla H \propto H$, the change in magnetization from a reference is $\Delta M \propto \Delta F/H \propto \Delta C/H$. The reference is defined by the fact that $F(H = 0) = 0$. The $\nabla H$ needed to apply a force on the sample is obtained by positioning the sample slightly above the center of the field. Table 4.2 gives field gradient specifications for the magnet (SCM1) used at the National High Magnetic Field Laboratory. For typical runs, the cantilever was placed 27.0 mm or 52.4 mm above the center of the field, but for initial runs, it was placed as far as 152.4 mm off the center of the field.

Sensitivity is gained by working far off the center of the field because $\nabla H$ increases until approximately 160 mm away from the center of the field. However, the peak field decreases as the cantilever is moved away from the center of the field. For example, the 152.4 mm length maximizes the cantilever response

| $Z$ (cm) | $B_Z$ (T) | $dB/dZ$ (T/cm) |
|---|---|---|
| 0.000 | 20.000 | 0.000 |
| 0.500 | 19.986 | 0.028 |
| 1.000 | 19.946 | 0.080 |
| 1.500 | 19.877 | 0.138 |
| 2.000 | 19.779 | 0.196 |
| 2.500 | 19.651 | 0.256 |
| 3.000 | 19.491 | 0.320 |
| 3.500 | 19.300 | 0.382 |
| 4.000 | 19.064 | 0.472 |
| 4.500 | 18.792 | 0.544 |

Table 4.1: Field and gradient at distances off the center of the field along the axis of the magnet SCM1.

but only provides a field of 8 T on the sample when the center field is 18 T. The 52.4 mm distance provided the optimal maximum field and sensitivity, although there are occasions when it is experimentally prudent to place the sample closer to, or farther away from, the center of the field.

As with any technique, certain limitations must be considered to effectively use the cantilever magnetometer. First, the magnetic response of the apparatus is difficult to calibrate. A slightly different background response is observed for every sample, arising from differences in mass and the magnetic response of the mounting material. Therefore, a calibration must be run *in situ* for each different sample mounting. This procedure is time consuming and is often infeasible for the time allotted at the National High Magnetic Field Laboratory. Furthermore, our attempts at calibration were too coarse to be useful. Nevertheless, an absolute measure of magnetization is not essential for identifying critical fields.

Therefore, the cantilever is an excellent device for studying the Haldane gap. Second, since the force is divided by the magnetic field to obtain the magnetization, the error bars in the magnetization grow quickly at fields below 1 T, obscuring low field features. In addition at low fields, superconducting magnets, which have been run above $H_{c1}$ of the superconducting wire, spontaneously expel magnetic flux trapped in the wire, and this effect causes noise in the measurement known as flux jumps. Therefore, the issue of a usable low field region is a combination of the limitation of the technique and the apparatus used. Third, the force is always measured relative to the zero magnetic field state. Therefore, a constant force or magnetization can not be distinguished from no magnetization. For example, at millikelvin temperatures, where paramagnetic spins saturate at a few mT, a paramagnetic contribution can not be distinguished from the zero ground state in a Haldane system.

To ensure that the limitations on the experiment result from the cantilever alone, a low noise set of electronics, shown in Figure 4.4, was used to acquire data. The dark grey and light grey shading identifies the portions of the apparatus that are inside the mixing chamber of the dilution refrigerator and immersed in the liquid helium bath, respectively. The dotted box indicates a device that was tested, found to provide negligible improvement, and subsequently removed. The temperature controller used a four wire measurement to regulate the temperature. At the time of our experiments, the thermometer was calibrated for zero magnetic field only. Therefore, the resistance of the thermometer at the start of the run was compared to the resistance at the end of the run to be sure that thermal

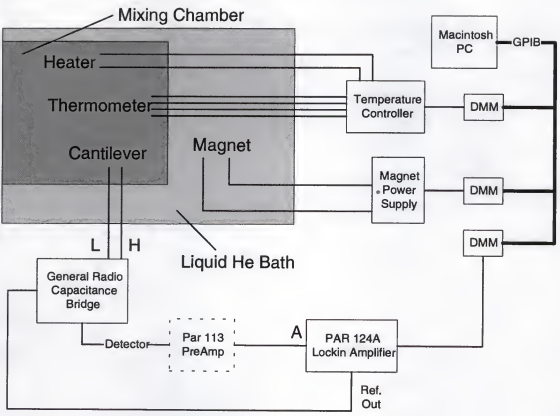


Figure 4.4: Cantilever magnetometer electronics schematic. The dark grey and light grey shading identifies the portions of the apparatus that are inside the mixing chamber of the dilution refrigerator and immersed in the liquid helium bath, respectively.

stability was maintained throughout the run. A heater provided the necessary temperatures above base temperature, although it was rarely needed. Several different digital multimeters were used as analog to digital converters, and all of them added negligible amounts of noise to the measurement. To reduce noise, a lock-in amplifier was used for phase sensitive detection. The Princeton Applied Research model 124A lock-in amplifiers, PAR 124A, were chosen since their signal to noise ratio was at least an order of magnitude better than any other instrument tested. The PAR 124A has an internal voltage controlled oscillator that was operated at $\sim$ 10 kHz. In order to reduce coupling from the outside environment as much as possible, the wires from the General Radio capacitance bridge to the top of the insert were a twisted pair of coaxes. Finally, all data was collected by a Macintosh personal computer, using a general purpose interface bus (GPIB) and the LabView software package.

To cool the samples to temperatures well below the Haldane gap, an Oxford Instruments Kelvinox top loading dilution refrigerator was used. The top loading nature of the cryostat allows samples to be mounted while the refrigerator is at $\sim$ 4 K. Once the sample is in the mixing chamber, condensation and circulation can begin, and within 6 hours, the sample is at a base temperature of $\sim$ 30 mK. The magnet used was SCM1, a superconducting magnet provided by Oxford instruments. The maximum center field is 18 T at $T = 4.2$ K, and 20 T can be reached through the use of a lambda refrigerator that reduces the temperature to $\sim$ 1.4 K. The current/field ratio is known to be 10 A/T, so the magnetic field on the sample is determined by the output current of the magnet power supply.

## 4.3 Electron Spin Resonance

Electron spin resonance is a powerful microscopic probe of magnetic properties. Its use provided a wealth of information on the end-chain spins in NINAZ. There were two experimental apparatuses used for the ESR work presented in this thesis. The most extensively used instrument was a Brueker X-band spectrometer working at $\sim 9$ GHz. Professor D.R. Talham of the Department of Chemistry at the University of Florida graciously provided the use of this spectrometer and its support staff. Figure 4.5 shows a schematic diagram of the apparatus. A standard (*i.e.* iron yoke and water cooled) split coil magnet applied a DC field to the sample in a direction perpendicular to the direction of the microwave propagation. Since this spectrometer uses a resonance cavity and a Klystron for a microwave source, it is more convenient to vary $H$ instead of $\omega$, as is the standard practice [55]. This resonance cavity is coupled with an Oxford ESR 900 Flow Cryostat, which cools the sample down to $T \sim 4$ K. The temperature is measured by a AuFe/Ch thermocouple with the reference junction kept at 77 K. Figure 4.6 is a schematic diagram illustrating the flow of the helium gas and the sample and thermometer positions. Single crystal samples were affixed to the end of a quartz rod using Apiezon L grease and inserted directly into the flow of the helium gas. On the other hand, powder samples are placed in a quartz tube, so the sample is thermally coupled to the helium gas through the tube. The heater is placed well away from the sample to avoid any interference in the measurement. However, this arrangement lengthens the thermal equilibration time of the sample. Therefore, one should wait at least five minutes, after a temperature

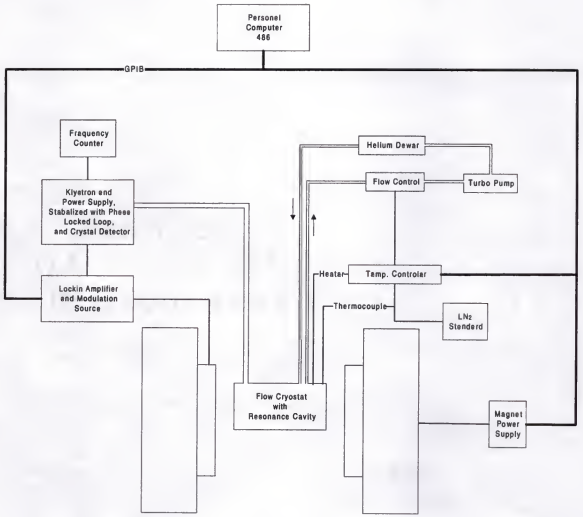


Figure 4.5: Schematic diagram of the X-band ESR spectrometer.

change, for the system to thermally equilibrate. Additional care should be taken with powder samples, or samples of low thermal conductivity, as the thermometer directly measures the temperature of the helium gas and not the temperature of the sample. To ensure proper thermal conductivity between powder samples and the quartz tube, a syringe was inserted into the rubber stopper at the end of the tube, and this arrangement was evacuated via a mechanical pump while initially cooling the cryostat. When the base temperature was reached, pumping was stopped, and helium exchange gas was injected into the sample tube. Not shown in Figure 4.6 is the room temperature coupling which allows the sample to be rotated without leaking air to the cryostat. A homemade goniometer was used to determine the orientation of the magnetic field with respect to the crystal axes.

To accommodate for the signal to noise improvements offered by a phase-locked loop, a small modulation field was added to the DC field. Introducing the modulation has the added affect of differentiating the absorption signal. Returning the data to an absorption signal from the derivative signal was accomplished using a second-order, Runge-Kutta numerical integration routine [138] with an automatic baseline adjustment procedure. The code was written in Microsoft Visual C++ Version 4.0 and ran on a PC running Windows95.

Since a measure of absolute signal intensity was required, a room temperature calibration against $\alpha,\alpha'$-diphenyl-$\beta$-picrylhydrazyl (DPPH) was performed following standard procedures [55, 139]. A 0.1 mg single crystal purchased from the Aldrich Chemical Company was used for the calibration. With a molecular

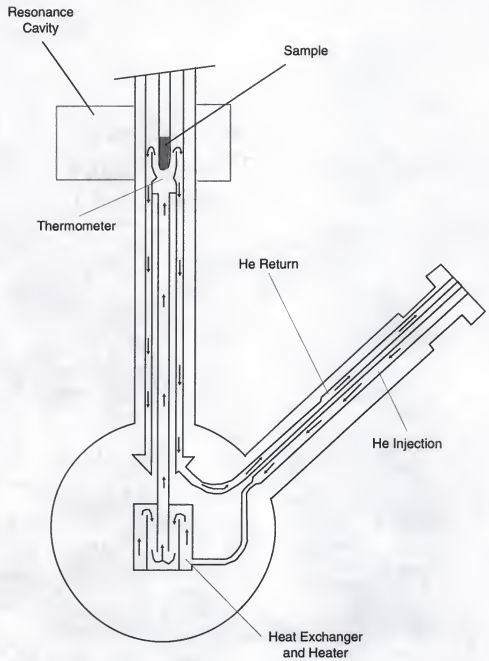


Figure 4.6: Cross-sectional schematic view of the ESR flow cryostat. Adapted from [140]

weight of 394 g/mol and 1 free spin per molecule [139], our sample contained $1.52 \times 10^{17}$ spins. Figures 4.7 and 4.8 show the derivative signal and the integrated absorption signal, respectively. The incident microwave power used for the calibration was -30 dB of 300 mW at a frequency of $\nu = 9.5453$ GHz. The area under the intensity, $I$, vs. $H$ data is $2.279 \times 10^8$ Iunits·kG which results in $6.67 \times 10^8$ spins/Iunit·kG. This procedure has effectively calibrated the area under the ESR spectrum to the number of spins. In order to determine the intensity of the DPPH signal at lower temperatures, a Curie law was assumed, and the corresponding number of spins calculated. The procedure avoids the non-Curie law behavior, observed in DPPH below $\sim 50$ K [55], because the calibration was performed at room temperature where correlations between DPPH spins are negligible.

Preliminary high frequency ESR work was done using the high field transmission spectrometer in the laboratory of Professor L.C. Brunel at the National High Magnetic Field Laboratory. The spectrometer has four changeable Gunn oscillator sources with Schottky based harmonic generators and appropriate filters which allows harmonics of these sources to be used. The available frequencies are given in Table 4.2. The 25-130 GHz source does not have sufficient power for use with the harmonic generators. The magnetic field is supplied by an Oxford Instruments 17 T superconducting magnet oriented with the field longitudinal to the microwave beam. The spectrometer measures the microwave radiation transmitted through the sample, so the beam comes out of the source, passes through

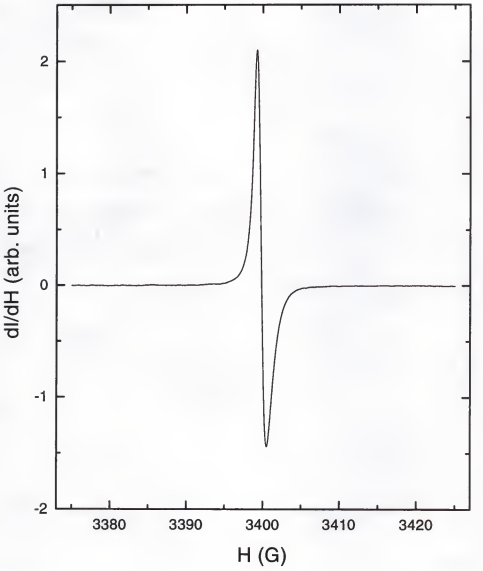


Figure 4.7: $dI/dH$ vs. $H$ for a 0.1 mg sample of DPPH at $T = 293$ K.

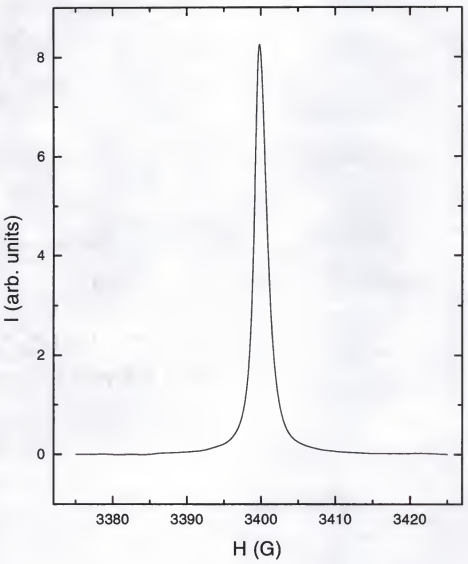


Figure 4.8: $I$ vs. $H$ for a 0.1 mg sample of DPPH at $T = 293$ K.

| Source | Harmonics | | | |
|---|---|---|---|---|
| 25-130 | - | - | - | - |
| 75 | 150 | 225 | 300 | 375 |
| 95 | 190 | 285 | 380 | 475 |
| 110 | 220 | 330 | 440 | 550 |

Table 4.2: Frequencies available for microwave transmission at the National High Magnetic Field Laboratory, in units of GHz.

the sample, and then is reflected back to a detector, usually a bolometer, which records the data on a Macintosh personal computer.

## 4.4 Neutron Scattering

To extend our studies of the Haldane gap, inelastic neutron scattering has been used as an additional microscopic probe. Precise measurements of the reciprocal lattice vectors are required for inelastic neutron scattering measurements, so neutron diffraction was used to determine them. In any neutron scattering experiment, both elastic (neutron diffraction) and inelastic scattering is observed. A full analysis separates the received scattering intensity into four components: elastic coherent scattering, elastic incoherent scattering, inelastic coherent scattering, and inelastic incoherent scattering [141]. Elastic coherent scattering is typified by Bragg peaks that are usually the largest contribution to the received intensity. The next largest contribution results from incoherent scattering. If a large incoherent scattering peak is observed, it arises from randomly oriented nuclear magnetic moments. Therefore, careful isotope selection during sample synthesis will greatly reduce this contribution. For example, the samples studied

for this thesis possess large organic ligands, so hydrogen would be the largest incoherent scatterer because the single proton has a rapidly moving nuclear magnetic moment of $I = 1/2$. On the other hand, deuterium has no nuclear moment, so full deuteration of the samples eliminates the largest source of incoherent scattering. Generally, in properly deuterated samples, the incoherent scattering component is negligible when compared to the coherent elastic scattering and can be neglected for structure refinements. In addition, inelastic components are generally much smaller than elastic components and can be neglected in neutron diffraction experiments.

When inelastic neutron scattering measurements are performed, coherent elastic scattering is the most troublesome component. The simplest way to eliminate the contribution due to these Bragg peaks is to avoid measuring regions of $Q$ space where they exist. In addition, the incoherent elastic component is usually much larger than the coherent inelastic component and must be avoided. There are two ways to avoid this contribution. Firstly, reduce the contribution as much as possible by choosing appropriate isotopes, and secondly, since incoherent scattering is always around $Q, E = 0$, inelastic scattering at sufficiently large wavevectors and energies are unaffected by the incoherent scattering peak.

A mixed blessing and curse of neutron scattering experiments is that the neutrons interact weakly with the material. Therefore, at least 1 g of materials is needed for sufficient experimental resolution [142]. The metal-organic materials used for these measurements usually do not grow in single crystals this large. Therefore, an added complication to the work was that a collection of randomly

oriented microcrystallites was used for the measurement. Fortunately, the microcrystalites were small enough to effectively act as a symmetric powder as will be described in Section 7.3. Therefore, to determine the lattice parameters, the powder neutron diffraction pattern was analyzed by Rietveld refinement.

Rietveld refinement is essentially a non-linear least squares fit between an assumed crystal structure, whose Bragg peaks are powder averaged, and the actual data. Since Rietveld, who developed the method, believed strongly in the free dissemination of information, his computer routines [143–145] have been freely distributed and used to develop excellent public domain analysis software. The package used by the author is GSAS from Los Alamos National Laboratory which has a user friendly interface for the personal computer running Microsoft Windows. This program runs sufficiently fast on a Pentium based machine with copious quantities of memory. Insufficient memory space (*e.g.* 24 megabytes is not enough) causes program crashes which require restarting the refinement from the raw data. Generally, the technique is extremely powerful and up to 193 parameters have been refined, 161 of them simultaneously [146, 147]. As with any non-linear least squares fitting, one must have some feel for the right answer before starting, otherwise the fit of the naive user will be stuck in a local minimum in the multiparameter hyperspace. The method used to avoid local minima was to examine the resultant crystal structure for physical plausibility on the basis of the known chemical composition. Furthermore, several different quantities can be used to quantify the quality of the refinement [147]. The primary test statistic used was $\chi^2$ reduced by the number of parameters being varied, and the total

$\chi^2$ was used as a secondary test to confirm that changes in the reduced $\chi^2$ were significant.

The spectrometer used was the high resolution powder diffractometer on beam tube HB-4 of the High Flux Isotope Reactor (HFIR) at Oak Ridge National Laboratory. The wavelength of the neutron beam is selected by orienting a (115) Ge single crystal. This monochromator provides the sample with wavelengths of 1.0, 1.4, 2.2, or 4.2 Å. The beam passes through the sample to 32 $^3$He detectors that are equally spaced at 2.7° apart. These detectors can be scanned over a range of 40° so the total angle covered is 11° to 135°. A collimator in the beam reduces the beam size from the maximum $3.75 \times 5\ cm^2$ to the desired size. Typically, the flux at the sample is $2 \times 10^5\ \frac{\text{neutron}}{\text{cm}^2\text{s}}$ [148]. Using a glove box, the sample is placed inside a vanadium can in a helium atmosphere. The can is sealed with an indium o-ring before removing it from the glove box. If two sample batches need to be kept separate inside the vanadium can, each batch is placed in an aluminum foil pouch. For room temperature measurements, the sample is rotated while in the neutron beam to average out any asymmetry in the powder. For temperature dependent measurements, a displex was used with aluminum vacuum cans, and this refrigerator was capable of achieving 11 K.

The main goal of the neutron scattering study is to examine the magnetic excitation spectrum with inelastic neutron scattering. There are several factors to consider when choosing an instrument for inelastic neutron scattering. Firstly, the incident neutron energy must be selected so that the desired features are resolvable. As a general rule of thumb, the resolution is related to the incident

energy by $\Delta E \approx 0.02 E_i$ [142]. Therefore, neutrons from a water moderated reactor (thermal neutrons) have $\Delta E \approx 0.5$ meV, but the Haldane gap is expected to be around 0.2 meV. Consequently a source of lower energy neutrons (cold source) is required. Once the cold source is identified as necessary, there are several instruments from which to choose to make the measurement.

Since the sample used is a powder sample, a technique which could collect data for a broad range of Q values simultaneously is desirable. This requirement means a time of flight spectrometer is ideal. For inelastic neutron scattering, four quantities must be known: the initial energy, the initial momentum, the final energy, and the final momentum. Assuming the initial quantities can be tuned, only the final energy and momentum have to be measured. For time of flight, the energy and the magnitude of the momentum are determined by the time required for the neutron to travel a known distance. A pulsed source of neutrons provides a $t = 0$ reference for the time measurement. To determine the final angle of the momentum, the detectors are equally spaced at known angles. Since the detectors are fixed, data for multiple Q values is collected simultaneously.

The time of flight spectrometer (TOF) on the cold source at the National Institute of Standards and Technology was chosen for the measurement. A liquid $H_2$ moderator is used as the cold source to provide a distribution of neutrons peaked around an energy of 5 meV. Neutrons from the cold source are directed to the instrument in neutron guide NG-6. Once at the instrument (Figure 4.9), two pyrolytic graphite monochromators select neutrons of the desired energy. Next, a cooled Be and pyrolytic graphite filter removed neutron beam compo-

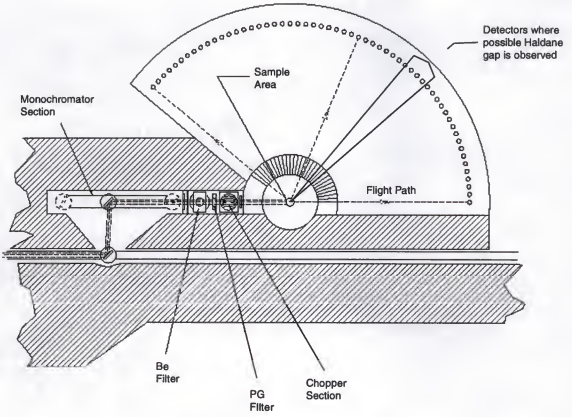


Figure 4.9: NIST TOF spectrometer from Reference [149]. Notice the region of detectors used to identify hints of the Haldane gap in $MnCl_3$(d-bipy).

nents remaining from higher order reflections in the monochromator crystals. In addition, a Fermi chopper sets the length of the time pulse. Finally, a flux of $2.4 \times 10^4 \frac{\text{neutron}}{\text{cm}^2\text{s}}$ interacts with the sample, passes through an oscillating radial collimator, and is detected by $^3$He detectors. The detectors are equally spaced at $2.546^o$ for angles from $1.7^o$ to $130^o$. Unfortunately, the detectors for angles less than $22^o$ are too noisy for use on this experiment. For future reference, the region of detectors used to identify hints of the Haldane gap in $MnCl_3$(d-bipy) is indicated in Figure 4.9.

## 4.5 Mechanical Ball Milling

For part of this thesis, the antiferromagnetic chains were broken by mechanical methods. Mechanical ball milling was used to produce the finest ground powder using the ball mill of Professor J. H. Adair in the Department of Materials Science and Engineering at the University of Florida. To perform the milling, the material is placed in a polypropylene bottle with zicronia balls and fluid, hexane in this case, which efficates the crushing process. The bottle is then rotated for 36 hours to perform the pulverization. The resulting particle size distribution usually follows a log-normal distribution (Figure 4.10) [150].

## 4.6 Centripetal Sedimentation

A method was needed to determine the characteristic particle size of various samples. To this end, centripetal sedimentation was performed in the laboratory of Professor J. H. Adair in the Department of Materials Science and Engineering

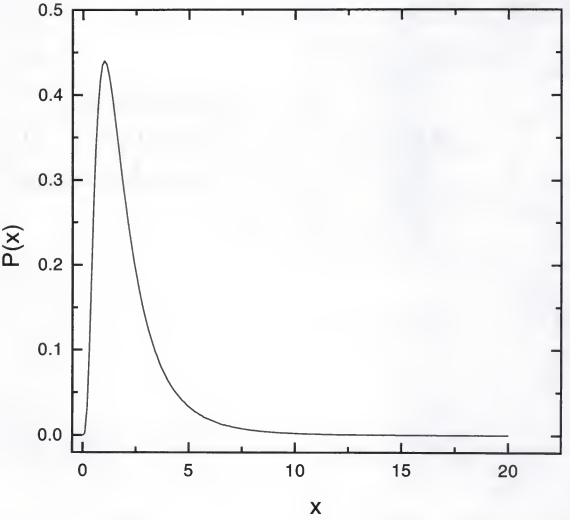


Figure 4.10: A normalized log-normal distribution of width 1 centered at x = 1. This is the theoretically predicted particle size distribution for a ball milled sample.

at the University of Florida. The main idea is to measure the spatial distribution of the particles in a medium of known viscosity when a known force is applied to them for a certain length of time. In our case, the viscous medium was hexane as it did not react with the material being studied. To measure the spatial distribution of distances, a laser light is passed through the particle-fluid mixture, and the relative intensity is directly proportional to the particle size distribution. The applied force arises from the centripetal acceleration from spinning the mixture [151].

## 4.7 Inductively Coupled Plasma Mass Spectrometry

Since this thesis claims that the end-chain spins are intrinsic impurities, a technique was needed to ensure that the extrinsic impurities in the sample were negligible. Therefore, inductively coupled plasma mass spectrometry, ICP-MS, was performed in the laboratory of Dr. D. H. Powell in the Department of Chemistry at the University of Florida. Figure 4.11 is a schematic of a typical ICP-MS system [152, 153]. It consists of a silica plasma torch which maintains the plasma by a continuous feed of gas (usually Argon) through radio frequency coils which couple to the plasma. The sample to be measured is introduced directly into the plasma and is ionized by the intense heat. Two small orifice cones are placed in series, approximately 10 mm from the edge of the torch, to remove ions from the useful part of the plasma. Once the ions are removed, they are sent into a standard quadrapolar mass spectrometer for analysis. Then, the ions are deflected by the charged plates in the quadrapolar mass spectrometer providing a distribution of the elements according to their molecular weight.

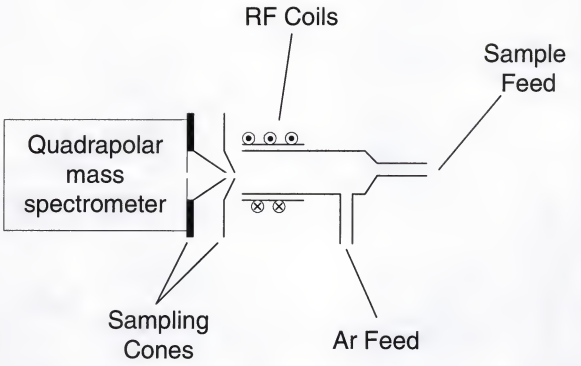


Figure 4.11: Schematic diagram of an ICP-MS system. The size of the torch and the cones is greatly exaggerated with respect to the mass spectrometer for illustrative purposes.

# CHAPTER 5
# TMNIN

This chapter covers magnetic measurements on $(CH_3)_4N[Ni(NO_2)_3]$, commonly known as TMNIN. Initial magnetic susceptibility measurements displayed the characteristics of a 1-D chain with a small exchange energy. Furthermore, magnetization, $M$, vs. magnetic field, $B$, measurements revealed a Haldane gap small enough to be reached by high resolution NMR magnets. Therefore, a program was started to grow and characterize single crystal specimens for NMR experiments. To this end, $M$ vs. $B$ measurements were performed at millikelvin temperatures in order to characterize the gap and single-ion anisotropy. These measurements revealed a small value of $D$ and are the main topic of this chapter.

## 5.1 Synthesis and Structure of TMNIN

Tetramethylammonium nickel nitrate (TMNIN) was first grown by Goodgame and Hitchman [71], and initial attempts at the crystal structure were made by Gadet *et al.* [72] using twined single crystals. Their results confirm that TMNIN is an antiferromagnetic chain with adjacent $Ni^{2+}$ ions bridged by three $NO_2^-$ groups. The tetramethylammonium group, $[(CH_3)_4N]^+$, sits between the chains to space them and provide charge neutrality. These features are clearly observed in Figure 5.1. Nevertheless, one feature of the crystal structure remained illusive until the single crystal X-ray diffraction studies by Chou *et al.* [74, 83].

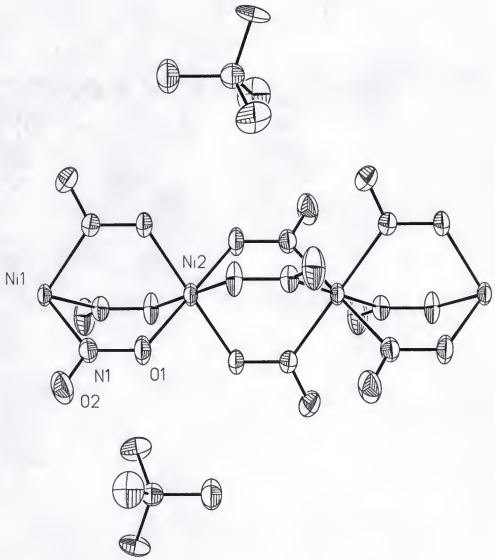


Figure 5.1: TMNIN Crystal Structure [74, 83]. Note that Ni1 is octahedrally coordinated with nitrite nitrogens, and Ni2 is octahedrally coordinated with nitrite oxygens.

More specifically, the Ni1 is octahedrally coordinated with six nitrite nitrogens, and Ni2 is octahedrally coordinated with six nitrite oxygens. Different Ni sites may slightly affect the magnetic properties of the chain, as will be discussed later in the chapter.

The single crystals used for the X-ray studies and the magnetization measurements, to be detailed below, were produced following the synthesis procedure of Goodgame and Hitchman [71], but modified to allow the crystals to grow undisturbed in a 284 K environment for 4 months. The synthesis procedure starts by slowly adding solutions of $NiBr_2$ and $(CH_3)_4NBr$ to a solution of $NaNO_2$. After 4 months, large single crystals were harvested from the sides of the container. Fifty of these single crystals were oriented and glued together with clear finger nail polish to produce a 2.1 mg packet. Both this packet and a few single crystals of approximately 1.1 mm in length and 0.11 mm in diameter were used in the magnetization studies to be described below.

## 5.2 Magnetization Measurements on TMNIN

Initial magnetization measurements on the TMNIN packet were performed on a SQUID magnetometer at 1.8 K and 30 K for magnetic fields from 0 to 5.5 T oriented parallel to the chains. As can be seen in Figure 5.2, a hint of the critical field associated with the Haldane gap is observed at $\sim$ 2.7 T. However, since the sample temperature is close to the size of the gap, the signature of the critical field is thermally smeared. The $T = 30$ K ($T \gg \Delta$) data provide additional circumstantial evidence for the presence of the gap since no critical field

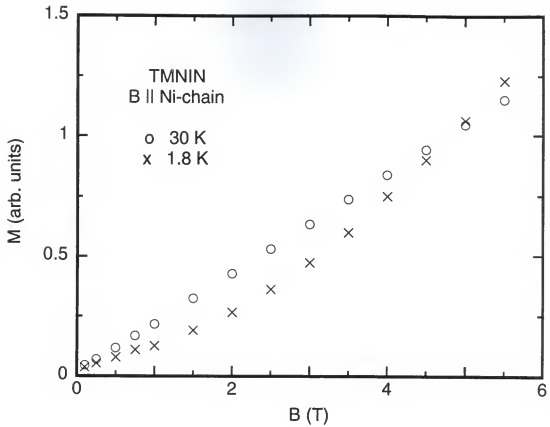


Figure 5.2: SQUID $M$ vs. $B$ for TMNIN at temperatures of 1.8 K and 30 K [75].

is observed. For both temperatures, the chain axis of the packet was oriented parallel to the magnetic field. Similar results were obtained by other workers [72, 77] for a powder sample.

To better resolve the critical magnetic field, subsequent measurements were performed at lower temperatures. The facilities of the National High Magnetic Field Laboratory were ideal for this purpose. Magnetization as a function of magnetic field was measured with the cantilever magnetometer described in Section 4.2. Millikelvin temperatures at high magnetic fields were provided by a

top loading dilution refrigerator in the superconducting magnet SCM1. Since our only concern was the value of the critical field, a quantity not requiring an absolute determination of the magnetization, the complicated and time consuming calibration process was bypassed. Two runs were made, the first on the above described packet and the second on a single TMNIN crystal. The packet was attached to the cantilever with silver paint, and the cantilever and sample were placed a distance of 16 cm from the center of the field. This position produced an ample field gradient for the cantilever to operate but reduced the maximum magnetic field at the sample by a factor of 2.5. Figure 5.3 shows both the force on the cantilever and the magnetization of the sample for sweeps from 0 to 8 T with the magnetic field oriented perpendicular to the chain axis. A critical field, associated with the Haldane gap, can be extracted as $B_{c\perp} = 2.90 \pm 0.15$ T. In addition, the uncertainty in the magnetization data increases greatly below 1 T. This increase is an artifact of the technique since magnetization is derived from the data using $M = F/B$, as described in Section 4.2. This effect emphasizes the need to examine the raw force data. Figure 5.4 shows data for the same sample with the field oriented perpendicular to the chain axis. Several sweeps are displayed. Again the critical field can be extracted as $B_{c\|} = 2.40 \pm 0.15$ T. The other striking feature in Figure 5.4 is the continuous bend in the data, starting near 4 T and continuing to the end of the data. This experimental artifact results from the diamagnetic contribution of the silver paint. For low and high fields, the sample and the diamagnetic background control the cantilever response, respectively. Therefore, at intermediate fields the observed data result from a competition between the

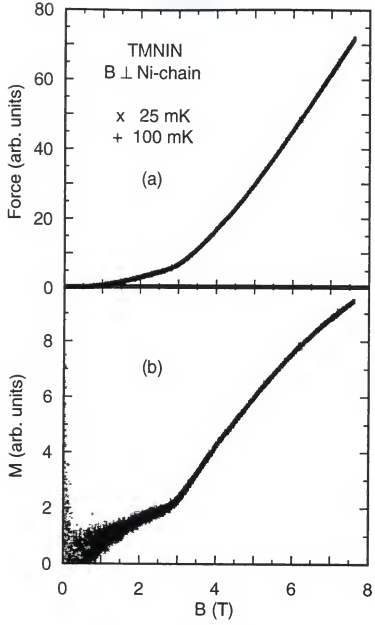


Figure 5.3: (a) $F$ and (b) $M$ vs. $B_\perp$ for TMNIN packet 16 cm off the center of the field [75]. The packet weighed 2.1 mg and was tested at $T = 25$ and 100 mK using the cantilever magnetometer.

sample behavior and the diamagnetic background. A couple of unique features are observed when the data in Figures 5.3 and 5.4 are compared. First, the data in Figure 5.3 exhibit a finite magnetization below the critical field. To see if this finite magnetization resulted from paramagnetic impurities, scans were performed at temperatures of $25 \pm 5$ mK and $100 \pm 5$ mK. There is no discernible difference between the data at the two temperatures, suggesting the absence of paramagnetic impurities. However, paramagnetic impurities saturate at a few mT for temperatures in the millikelvin range, and, therefore, a finite magnetization below the gap would result. Nevertheless, since this finite magnetization is absent for the other field orientation and any effect from paramagnetic spins should be isotropic, another explanation is needed for this effect. By comparisons of several runs on TMNIN, and further studies on other samples, we have determined this effect originates from slight differences in the mounting material from one run to the next. Later, the same sample packet and the cantilever were moved closer to the center of the field to improve the response of the system. The results are shown in Figure 5.5. Clearly there is a strong reaction to the magnetic field, such that above 6 T the cantilever responds nonlinearly. Nevertheless, a critical field of $B_{c\perp} = 2.60 \pm 0.15$ T can be extracted. To reduce the nonlinear effects, a second run on a single crystal of TMNIN was performed. The data are displayed in Figures 5.6 and 5.7. These data are consistent with the packet data, albeit with slightly different critical fields. This difference might be caused by internal stresses present in the packet, due to thermal contraction differences between the fingernail polish and the sample, that are absent in the single crystal.

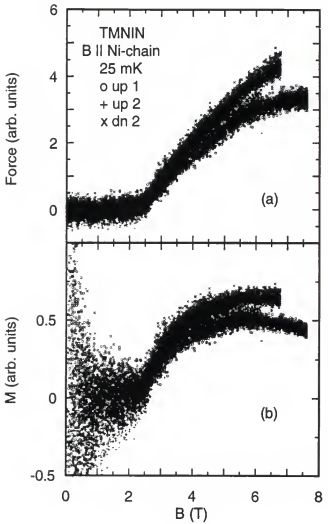


Figure 5.4: (a) $F$ and (b) $M$ vs. $B_{\|}$ for TMNIN packet 16 cm off the center of the field [75]. The results of several magnetic field up and down sweeps for this 2.1 mg packet using the cantilever at $T = 25$ mK are shown.

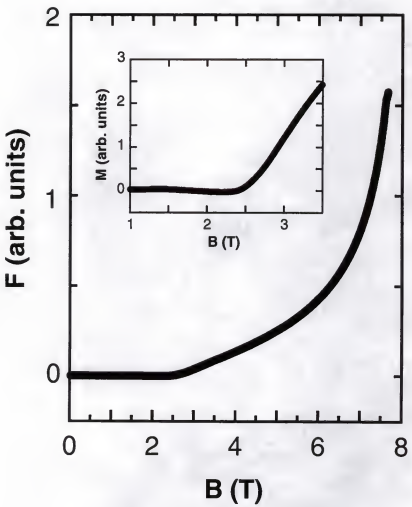


Figure 5.5: (a) $F$ and (b) $M$ vs. $B_\perp$ for TMNIN packet 5 cm off the center of the field [76]. The cantilever magnetometer made the measurement on this 2.1 mg packet at $T = 60$ mK.

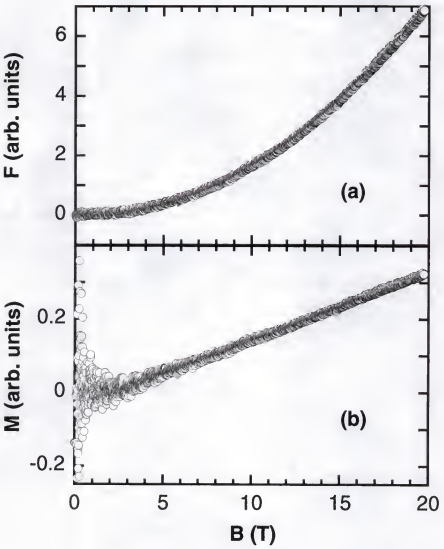


Figure 5.6: (a) $F$ and (b) $M$ vs. $B_\perp$ for TMNIN single crystal using the cantilever magnetometer placed 5 cm off the center of the field [76].

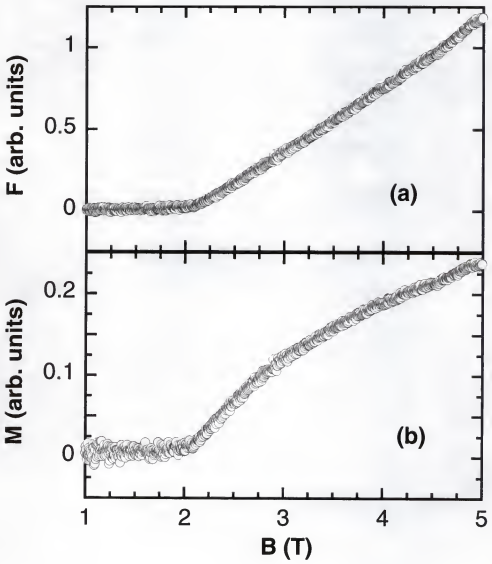


Figure 5.7: (a) $F$ and (b) $M$ vs. $B_{\|}$ for TMNIN single crystal using the cantilever magnetometer placed 5 cm off the center of the field [76].

The validity of this assertion is strengthened by the experimental results on NENP that demonstrate an increased gap with increased pressure [133].

As mentioned in Sections 2.3.1 and 3.2, the critical fields can be used to determine the Haldane gap and the single-ion anisotropy. The critical fields with the least uncertainty were obtained from Figures 5.5 and 5.4. Using Equations 2.14, 2.15, and $g = 2.09$ from previous work [75, 83], the corresponding gaps are $\Delta_\perp = 3.34 \pm 0.21$ K and $\Delta_\parallel = 4.88 \pm 0.28$ K. Solving Equations 2.17 and 2.16 simultaneously, with the above values and $\kappa = 1/3$, provides $\Delta = 3.5 \pm 0.2$ K and $D = 0.6 \pm 0.3$ K. The ratio $D/J = 0.06$, where $J = 10.11 \pm 0.05$ K, shows that TMNIN has the lowest single-ion anisotropy of any $S = 1$ material known to posses a Haldane gap, see Table 3.1.

## 5.3 Comparison with Other Experiments

Several other groups have performed measurements on TMNIN using several techniques. Comparisons between all of the studies provide insight into global features of the system.

Most of these experiments also provide measurements of $\Delta$. Gadet *et al.* [72] made several tests on powdered specimens of TMNIN, all of them consistent with a Haldane gap of 3.5 K. Notably, they performed proton NMR, and the temperature dependence of $T_1$ behaves in a manner consistent with similar measurements in NENP (Section 3.2). Nevertheless, their resolution of the gap was greatly reduced by thermal smearing since their lowest temperature was 2 K. The magnetic field dependent magnetization measurements of Takeuchi *et al.* [73] exhibit

a critical field of $\sim 2.5$ T, which is also consistent with our results. Furthermore, using magnetic fields up to 40 T, they saturated the spins of the chain. TMNIN has been studied by several groups using high field ESR [154,155]. The results for powder samples show an asymmetric line shape with a large peak and several small features. The large peak is clearly attributable to the Haldane phase and is consistent with our measured value for the gap. However, the line shape and additional peaks are consistent with a picture of large single-ion anisotropy, $D \approx 0.5$, in sharp disagreement with the magnetization results presented here for single crystals. A simple explanation could be provided by sample differences because the strongest point for large single-ion anisotropy is a peak attributable to a transition between $\Delta_{xy}$ and $\Delta_z$, but this line is small. Therefore, it could be due to an impurity phase in the powder. The existence of an impurity phase in powder samples is not unprecedented since early growth batches by our research group displayed impurities when checked by magnetic susceptibility measurements [156]. However, if good quality is assumed for all the samples, the existence of two magnetically different Ni sites is another possible cause for this discrepancy. The alternating coordination of the Ni sites would be the likely origin of these non-equivalent sites. Though no measurements have been made to definitively test this assumption, unexplained details of several experiments suggest that this effect warrants further investigation. Magnetically different Ni sites could produce additional local magnetic fields that would cause additional ESR lines and an asymmetric line shape. Another detail to examine is the ESR spectrum for Zn doped samples of TMNIN. Deguchi *et al.* [115] doped TMNIN

with Zn to study end-chain spin effects by ESR and magnetization. The significant feature of their data is the unexplained ESR line shape. Clearly their 1.7 K trace shows two peaks. These two peaks could originate from the two distinct Ni sites. However, further analysis is needed to eliminate other sources, *e.g.* the dopants, of multiple lines. Neither of these reasons alone or combined are convincing evidence for magnetically different Ni sites in TMNIN, yet they provide a sufficient argument to pursue further tests. One possible test would be to continue this work with proton NMR. The observed line shape below the gap could confirm or deny this staggered magnetization as was the case in NENP [98]. However, the protons are far removed from the Ni sites in TMNIN, so the effects of these sites on the line shape may be unresolvable.

# CHAPTER 6
# NINAZ

After the magnetic susceptibility results on NENP showed a possible magnetic transition at approximately 4 mK, a search for a material with a larger exchange energy was commenced. The material chosen was $Ni(C_3H_{10}N_2)_2N_3(ClO_4)$, which is commonly known as NINAZ. Although this material has a larger $J$, to date no evidence of a transition, reminiscent of the possible transition in NENP (see Section 3.3), has been observed down to $T \approx 40$ mK. Nevertheless, NINAZ is ideal for the study of end-chain spins because it has a structural transition that naturally causes chain breaks. In addition to these numerous natural chain breaks, NINAZ posses several other qualities that make it a good model system. For example, the interaction energy scale is large enough to study the quantum properties of end-chain spins at 4 K, and there is no staggered magnetization to affect the symmetry of the ESR line shape as was observed in NENP [109, 110]. The primary focus of this chapter is a description of the behavior of end-chain spins as studied by macroscopic and microscopic probes. To introduce this topic, a description of the material will be given, followed by a discussion of experimental work on NINAZ prior to this thesis.

## 6.1 Material Description

The sample NINAZ, properly called *bis*(propylenediamine)azidonickel(II) perchlorate, is an ionic-covalent salt where the Ni chain is the cation and the perchlorate is the counterion. The antiferromagnetic chain is made of $Ni^{2+}$ ions bridged by azido ligands ($N_3$ bridge) providing a Ni-Ni distance of 5.849 Å. The N atoms of two propylenediamine ligands fill the four remaining bonding sites of each Ni ion. The room temperature crystal structure is shown in Figure 6.1. Gadet *et al.* [81] were the first researchers to resolve this crystal structure. At approximately 255 K, NINAZ has an irreversible structural transition which causes the sample to shatter. The room temperature phase has an orthorhombic unit cell with $a = 5.86$ Å, $b = 8.28$ Å, and $c = 15.15$ Å. For the lower temperature phase, the structure changes to monoclinic, where the $b$ axis becomes $a = 16.22$ Å, the $a$ axis becomes the $c = 31.04$ Å, the $c$ axis becomes the $b$ axis with no change in magnitude, and $\beta \approx 95°$. Since the chain axis is the low temperature $b$ axis (high temperature $c$ axis), the structural transition does not cause any dimerization. Neutron scattering studies of a deuterated crystal cooled through the transition temperature reveal that the low temperature phase has two domains [82]. A detailed crystal structure of these domains is still unavailable. The structural transition is an order to disorder transition. At room temperature, both the perchlorate counter ion and the propylenediamine ligands are disordered. Therefore, there are two possible order to disorder transitions to cause the observed structural transition. For similar salts, the counter ion orders, and this assignment is made by Gadet *et al.* [81]. Nevertheless, our research with similar materials

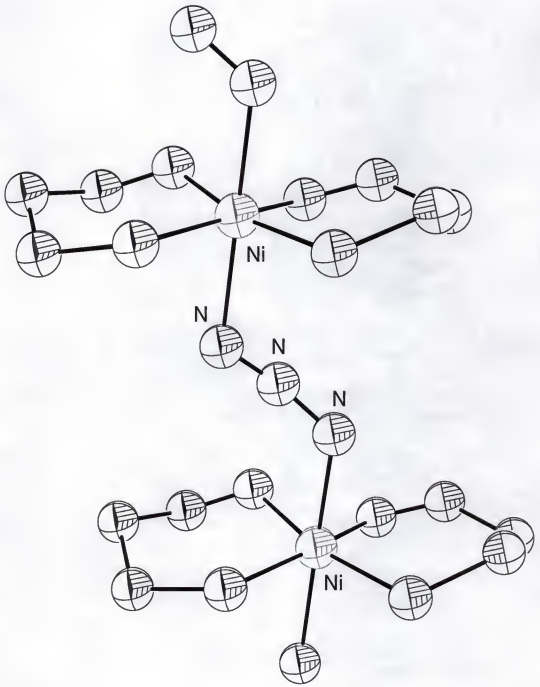


Figure 6.1: Room temperature NINAZ crystal structure [81]. The $N_3$ ligand provides the superexchange pathway between Ni sites. The ($C_3H_{10}N_2$) ligands and the ($ClO_4^-$) ions, which are not shown for clarity, space the chains.

suggests ordering in the propylenediamine group. For example, the material $Ni(C_3H_{10}N_2)_2N_3(PF_6)$ also shatters when cooled to 77 K, suggesting that the transition is independent of the counter-ion. Further evidence is provided by the fact that the related material $[Ni(C_4H_{12}N_2)_2(\mu- N_3)]_n(ClO_4)_n$, where the spacing organic ligand is different and the Ni sites are bonded with *cis* rather than *trans* bonds, does not shatter. More specific details of these two materials will be given below.

Chou improved upon the procedure for the formation of NINAZ which is described elsewhere [81, 83, 157], so the process is only sketched here. During the synthesis procedure, intermediate materials may be explosive. Therefore, small amounts of material should be synthesized, and the standard references [81, 83] should be consulted prior to synthesis. A stoichiometric amount of the reactant $H_2N(CH_2)_3NH_2$ is added in a drop wise fashion to the green solution of $Ni(ClO_4)_2 \cdot 6H_2O$ dissolved in water. The product of this reaction is a deep blue solution of $Ni(H_2N(CH_2)_3NH_2)_2(ClO_4)_2$. Then a stoichiometric amount of $NaN_3 \cdot H_2O$ is added to the product. After several days in solution, deep blue crystals of NINAZ will begin to form and can be collected by filtration. For the doped samples, 0.5% of the $Ni(ClO_4)_2 \cdot 6H_2O$ was replaced by $X(ClO_4)_2 \cdot 6H_2O$, where X = Hg, Zn, or Cd. In addition, Ward made a batch of $Ni(C_3H_{10}N_2)_2N_3(PF_6)$ by substituting $Ni(ClO_4)_2 \cdot 6H_2O$ with $Ni(PF_6)_2 \cdot 6H_2O$.

## 6.2 Other Experiments

Initially the magnetic susceptibility of NINAZ was characterized by Renard *et al.* [62] and Gadet *et al.* [81]. As shown in Figure 6.2, the broad peak, characteristic of a 1-D antiferromagnetic Heisenberg chain, followed by the sharp drop which fits an exponential excitation over an energy gap characteristic of a Haldane gap, are observed by these workers and ourselves. The subtle differences between the magnetic susceptibility measurements of each of the three groups will be discussed below. Later, high field $M$ vs. $H$ measurements [73], performed on a powder sample, identified a critical field of 30.0 T. The inelastic neutron scattering measurements of Zheludev *et al.* [82] provided a microscopic confirmation of the Haldane gap. Figure 6.3 shows several constant $Q$ scans, near $Q = \pi$, which confirm a Haldane gap of $\Delta = 41.9 \pm 0.3$ K. Each scan shows a relatively sharp increase and a broader drop off for higher energies, consistent with the predicted scattering function [45,67]. Furthermore, as $Q$ is moved away from the antiferromagnetic point, the scattering intensity decreases in a manner which is consistent with the existence of the two particle continuum [45,67,159]. As an aside, constant $Q$ scans with data shaped similar to scans in Figure 6.3, albeit on a greatly reduced energy scale, are expected for the inelastic neutron scattering results of $MnCl_3$(d-bipy) to be discussed in Section 7.4. Returning to NINAZ, in addition to the gap and its temperature dependence, Zheludev *et al.* [82] observed the splitting of the Haldane gap due to single-ion anisotropy. This observation determined $D = 21$ K. Other important materials parameters that they measured were the spin wave velocity $c_0 = (1.30 \pm 0.05) \times 10^5$ m/s and $J = 125$ K.

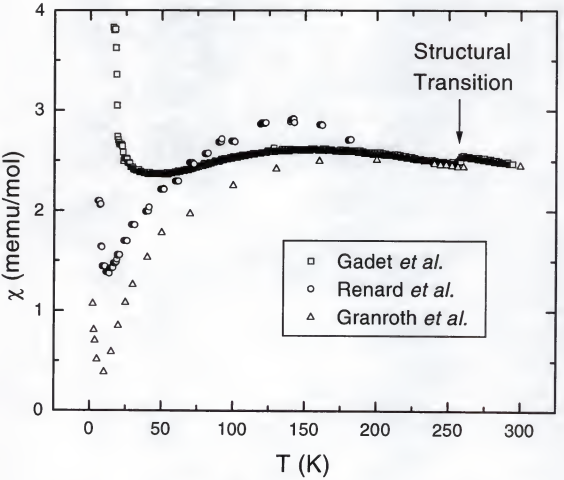


Figure 6.2: DC $\chi(T)$ of NINAZ. The results for powder NINAZ samples of Renard *et al.* [62], Gadet *et al.* [81], and this work are given. Notice the discontinuity at $T = 255$ K indicative of the structural transition.

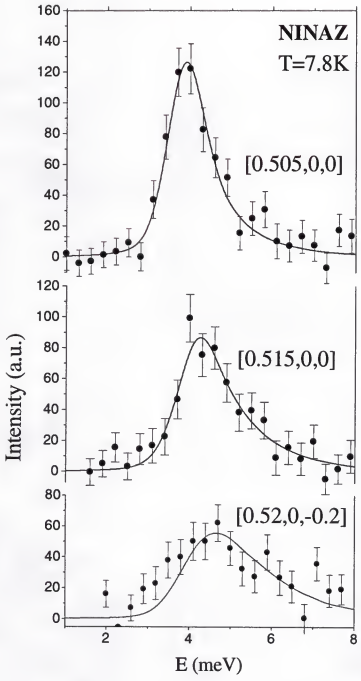


Figure 6.3: Constant $Q \approx \pi$ inelastic neutron scattering data for deuterated NINAZ. Below the Haldane gap there is no magnetic scattering. At the gap, there is a sharp peak characteristic of resonant scattering. The peak intensity decreases in a manner related to the correlation length of each spin. The data are from [82].

## 6.3 Experimental Studies

After the identification of NINAZ as a material with a large energy scale, we made magnetic susceptibility measurements to compare our sample with those of other groups. Since specimens made by our group and by others all displayed similar paramagnetic tails (see Figure 6.2), we came to the conclusion that the shattering processes produce numerous chain breaks as will be explained more fully below. This realization of non-doped end-chain spins motivated the detailed study of NINAZ which is discussed here.

### 6.3.1 Samples

Six types of samples were used in this study: a polycrystalline sample, a powder, an ultrafine powder, and samples doped with Hg, Cd, and Zn. The first three samples were all made without doping the material. The last three samples were measured for comparison with the undoped samples. A polycrystalline sample was a NINAZ single crystal that was cooled through the shattering transition. Even though after shattering it is no longer a single crystal, it remains an ordered conglomeration of microcrystallites with only a $5^o$ mosaic spread [82]. Therefore, the sample can be oriented with respect to the crystal axes. Two batches of NINAZ crystals were generated. Batch 1 was made by Chou and Batch 2 by Ward. This distinction is the same for all samples discussed. To increase the number of end-chain spins, two techniques were used to grind the samples. Initial grindings used a pestle and mortar to produce a sample referred to as *powder*. Subsequent grindings, using a standard ball mill as described in

Section 4.5, produced a sample referred to as *ultrafine powder*. To examine the particle sizes of each pulverized sample, centripetal sedimentation as described in Section 4.6, was performed. There were two powder samples characterized, one from Batch 1 (ground by Chou) and the other from Batch 2 (ground by Ward). Figure 6.4 shows that there is a small but observable difference in particle size distribution of the two batches. Nevertheless, both samples have an average particle size of approximately 5 $\mu$m. Two ultrafine powder samples were prepared as well. The first sample (from Batch 1) was powdered before it was ground in the ball mill. The second sample (from Batch 2) was placed directly into the ball mill. Figure 6.5 shows the difference between the two samples. The particle size distribution for the sample that was powdered before entering the ball mill is peaked at approximately 0.5 $\mu$m, whereas the sample that was not powdered had a particle size distribution broadly peaked around 1.5 $\mu$m. Nevertheless, this slight difference in particle size distribution is not significant enough to produce differences in the magnetic measurements.

One argument of this thesis is that free spins in the sample can be attributed to end-chain spins. Therefore, to confirm that the paramagnetic contribution did not originate from the extrinsic impurities in the samples, inductively coupled plasma mass spectrometry was performed on all the samples. The observed magnetic impurity limits are expressed in Table 6.1. The amount of $^{59}$Co impurities in the system could not be determined because the Ni line was so large. Nevertheless, Co impurities are not expected to exist in the starting materials, and none of the processes should introduce any. In addition, the strength of the Ni line limited the resolution of the Cu line as well.

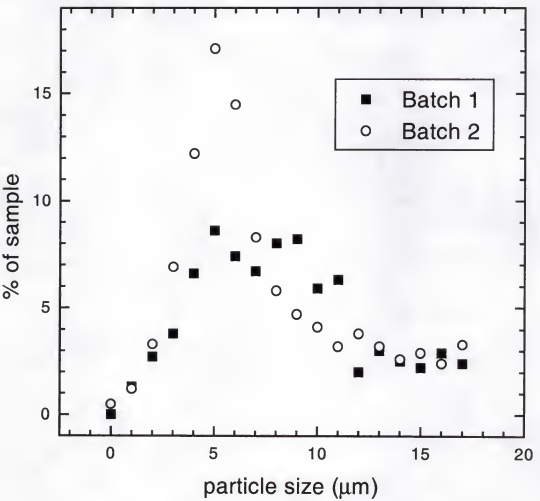


Figure 6.4: Powder NINAZ particle size distributions for a one sample ground by Chou (Batch 1) and another ground by Ward (Batch 2). Though differences are seen, the most probable particle size is approximately 5 $\mu$m for both batches.

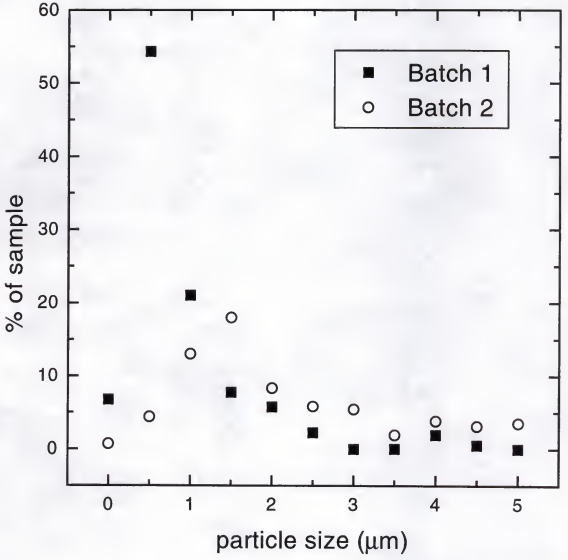


Figure 6.5: Ultrafine powder NINAZ particle size distributions. One sample was ground from powder (Batch 1) and the other was ground from crystals (Batch 2). The most probable particle size is slightly smaller for the sample ground from the powder.

| Element | Concentration |
|---|---|
| $^{55}$Mn | $< 20$ ppm |
| $^{56}$Fe | $< 24$ ppm |
| $^{65}$Cu | $< 160$ ppm |

Table 6.1: Maximum concentration of magnetic impurities in any NINAZ sample.

The shattering transition has an important role in these experiments. Therefore, its origin was tested by examining materials with a slightly different chemical composition. If the shattering transition was caused by ordering of the counter ion, there is a possibility that changing the counter-ion could eliminate the shattering process. To test this idea, the material $Ni(C_3H_{10}N_2)_2N_3(PF_6)$ was made. Nevertheless, when the sample was immersed in liquid nitrogen, it shattered as well. Further tests on this material were not made, but recent work by Monfort *et al.* [158] agree with our results. Another material with a different organic ligand will be discussed in the next section.

### 6.3.2 $[Ni(C_4H_{12}N_2)_2(\mu-N_3)]_n(ClO_4)_n$

(1,2-diamino-2-methylpropane)azidonickel(II) perchlorate or $[Ni(C_4H_{12}N_2)_2(\mu-N_3)]_n(ClO_4)_n$, which we call Ni zig-zag, is closely related to NINAZ, so it will be discussed in this chapter. The main purpose for studying this material was to test it as a candidate for an $S = 1$ spin ladder. A spin ladder is a pair of chains that are strongly coupled to each other but weakly coupled to other neighboring pairs. However, the following discussion will show that Ni zig-zag is actually a spin chain closely related to NINAZ. Therefore, this material lucidates the

structural properties of NINAZ. Ribas *et al.* [160] was the first to synthesize Ni zig-zag and resolve its crystal structure (Figure 6.6). Furthermore, they measured the magnetic susceptibility of a powder sample and characterized the results using the numerical work of Weng [21]. If the sample was actually a spin ladder, subtle discrepancies between the magnetic susceptibility and fits to linear chain theories should exist. Therefore, our goal was to improve the measurement resolution with the SQUID magnetometer to look for these discrepancies [161]. A close look at the crystal structure (Figure 6.6) shows why the material might be a spin ladder. The Ni sites are bridged by the azido ligand in a *cis* fashion. Therefore, the next nearest neighbor sites might have a sufficiently strong dipolar interaction to cause the materials to behave like an $S = 1$ spin ladder. This situation is similar, but not identical, to the coupling proposed for the $S = 1/2$ material $Cu_2(C_5H_{12}N_2)_2Cl_4$ [162, 163]. Unfortunately, there is no bond overlap and the next nearest neighbor dipolar interaction is weak, so this material maps to a linear chain. This determination was made via magnetic susceptibility measurements on a packet of single crystals oriented with the chains first perpendicular and then parallel to the magnetic field. Figure 6.7 shows that the data for the perpendicular orientation and a fit, using the high temperature expansions of Jolicœur given in Appendix A, are in excellent agreement. However, Figure 6.8 shows that this agreement breaks down below 60 K for the parallel orientation. These features are suggestive of an approach to long-range antiferromagnetic order (with $T_N \approx 10$ K) consistent with the observations in other materials [164]. Nevertheless, the results of these fits provide $J_\perp = 25.7 \pm 0.2$ K, $g_\perp = 2.16 \pm 0.03$,

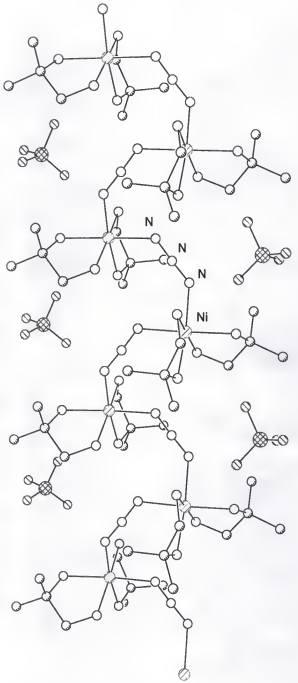


Figure 6.6: The crystal structure of $[Ni(C_4H_{12}N_2)_2(\mu\text{-}N_3)]_n(ClO_4)_n$ [160]. The ligands that connect one Ni site to another are in the *cis* position forming a zig-zag. There is no bond overlap between next nearest neighbor sites to form a ladder.

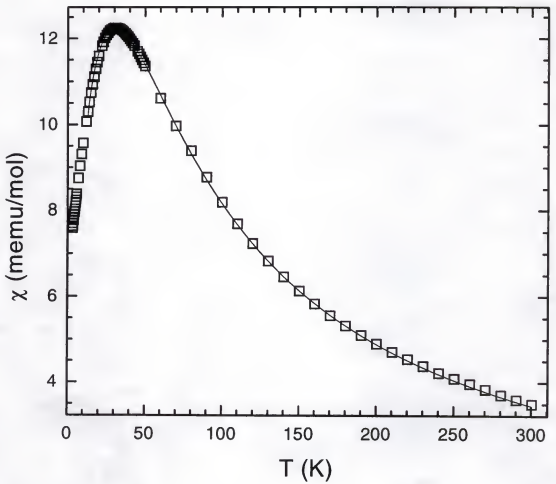


Figure 6.7: $\chi_{\perp}(2\,\mathrm{K} < T < 300\,\mathrm{K})$ for $[\mathrm{Ni}(\mathrm{C_4H_{12}N_2})_2(\mu\text{-}\mathrm{N_3})]_n(\mathrm{ClO_4})_n$ $H = 0.1$ T. The solid line is a fit to the numerical expressions of Jolicœur as discussed in the text.

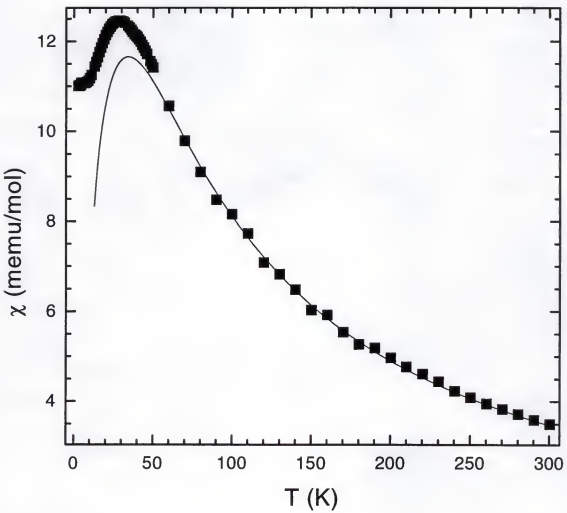


Figure 6.8: $\chi_{||}(2\,\mathrm{K} < T < 300\,\mathrm{K})$ for $[Ni(C_4H_{12}N_2)_2(\mu{-}N_3)]_n(ClO_4)_n$ $H = 0.1$ T. The solid line is a fit to the numerical expressions of Jolicœur as discussed in the text.

$D/J_{\perp} = 0.033 \pm 0.004$, $J_{\parallel} = 26.4 \pm 0.2$ K, $g_{\parallel} = 2.17 \pm 0.01$, and $D/J_{\parallel} = 0.0 \pm 0.1$. As mentioned Section 2.3.1, the fits require the use of Padé approximates. Therefore, the fits were performed using Maple V (release 4) to take advantage of its Padé approximates routines. A non-linear least squares fitting routine using the grid-search method [165] was used to semi-automate the process, but many manual parameter adjustments were required to minimize $\chi^2$.

### 6.3.3 Macroscopic Measurements

As mentioned earlier, magnetic susceptibility measurements were performed on polycrystalline samples of NINAZ to compare them with previously made materials. There are noticeable differences in the shapes of the curves which will be explained later, but the similar paramagnetic tails suggest the presence of end-chain spins. The magnetic susceptibility of both a powder and single crystal sample was measured down to $T \approx 50$ mK, using a standard mutual inductance technique, to see if the pulverization process created more end-chain spins [156]. The sample was cooled by a homebuilt dilution refrigerator. This technique and dilution refrigerator are described in detail in Reference [166, 167]. Figure 6.9 shows no difference in the paramagnetic tails, suggesting that the powder size is larger than the chain-length arising from the shattering process. To examine shorter chains, the magnetic susceptibility for an ultrafine powder sample was measured for $2\,\mathrm{K} < T < 300\,\mathrm{K}$ using the SQUID magnetometer and is shown in Figure 6.10. The increased paramagnetic tail indicates the presence of more end-chain spins. Normally a Curie-law is fit to the paramagnetic tail to determine the number of spins, but the paramagnetic tail is also affected by the magnetic

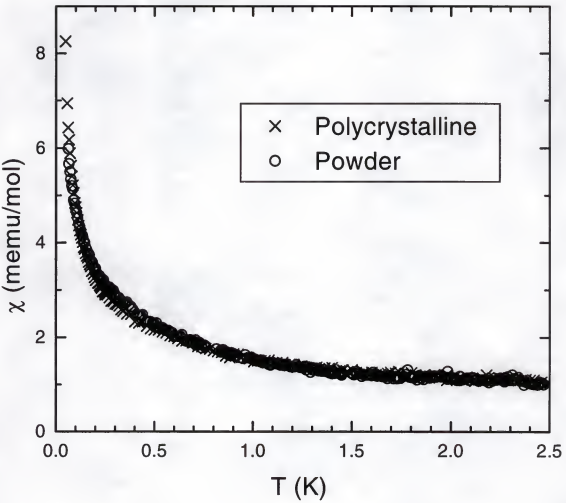


Figure 6.9: $\chi(50\,\mathrm{mK} < T < 2\,\mathrm{K})$ of polycrystalline and powder NINAZ from Batch 1 [156]. Notice that within the noise, there is no difference between the two data sets, implying that the powdering process does not reduce the chain length below that of the shattering process.

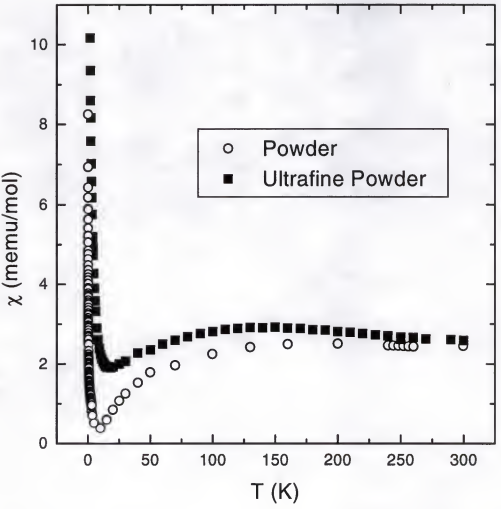


Figure 6.10: $\chi(T)$ for powder and ultrafine powder NINAZ from Batch 1. The ultrafine powder sample shows a increased paramagnetic tail when compared to the powder sample. In addition, the paramagnetic contribution displays effects even for $T \sim J$.

excitations on the chain. Therefore, an expression incorporating these features for $T < 0.2J$, as well as a small contribution resulting from the $S = 1$ chain components, is

$$\chi(T) = \frac{C}{T} f(T) + \sqrt{\frac{8}{\pi}} \left( \frac{\Delta(0)}{T} \right)^{1/2} e^{-\Delta(0)/T} \tag{6.1}$$

where $f(T)$ is some function, to be described later, dependent on the number of thermally excited magnetic excitations and the second term is from Equation 2.4. This expression leaves too many unknown parameters for a reliable determination of the number of spins. Nevertheless, qualitative comparisons to the Monte Carlo work of Yamamoto [24] need to be made. A comparison of the powder and ultrafine powder data in Figure 6.10 shows a significant difference, even at $T \sim J$. This difference is observed, to some degree, in the numerical work of Yamomoto [24]. However, these numerical chains are at least an order of magnitude shorter than our observed lengths, so quantitative comparisons are not possible. A similar change is observed when comparing our measurements to those of Gadet *et al.* [81], suggesting that their sample has shorter chain lengths.

Returning to the problem of determining the number of spins, it is clear that an independent probe is needed, specifically one not affected by thermally excited magnetic excitations nor the temperature dependence of the gap. Magnetic field dependent magnetization studies at $T = 2$ K fulfill this requirement by putting the sample in an environment such that $T \ll \Delta$. The resultant data are shown in Figure 6.11, and the solid lines are fits using

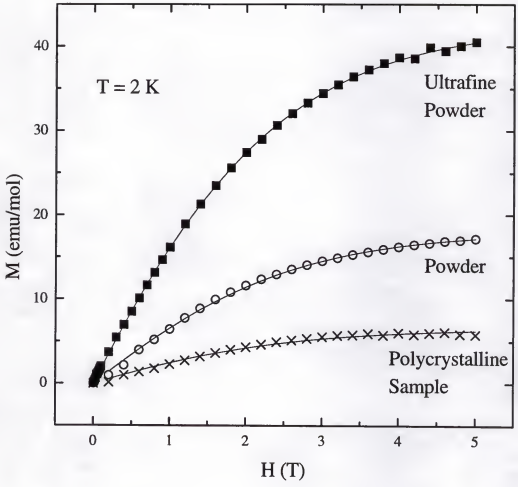


Figure 6.11: $M(H < 5\,\mathrm{T}, 2\,\mathrm{K})$ for polycrystalline, powder, and ultrafine powder NINAZ samples [168]. Notice each curve shows a successive increase in the number of end-chain spins.

$$M(H,T) = N_A g\mu_B \left[(1/2)\, N_{1/2} B_{1/2}(g\mu_B H/k_B T) + N_1 B_1(g\mu_B H/k_B T)\right], \tag{6.2}$$

where $B_{1/2}(g\mu_B H/k_B T)$ and $B_1(g\mu_B H/k_B T)$ are the Brillouin functions, and $N_{1/2}$ and $N_1$ are the concentrations of $S = 1/2$ and $S = 1$ spins, respectively [4]. Table 6.2 shows the results of the fits with $g = 2.174$ and $T = 2.00$ K as fixed parameters and $N_{1/2}$ and $N_1$ as determined by the fit. These results demonstrate

| | Polycrystalline Sample | Powder | Ultrafine powder |
|---|---|---|---|
| $N_{1/2}$ | $1000 \pm 60$ | $2840 \pm 50$ | $6280 \pm 50$ |
| $N_1$ | $20 \pm 10$ | $30 \pm 9$ | $140 \pm 8$ |

Table 6.2: Amount (in ppm) of $S = 1/2$ and $S = 1$ in the polycrystalline, powder and ultrafine powder samples from the $M(H, T = 2\,\mathrm{K})$ data (Figure 6.11) and its analysis described in the text.

that the end-chain spins are predominately $S = 1/2$ and that only trace amounts of $S = 1$, consistent with the presence of some free $Ni^{2+}$, exist in any of the samples. Consequently, we conclude all the end-chain spins are $S = 1/2$.

For comparison, the macroscopic properties of the doped samples were measured as well. Figure 6.12 shows that the magnetic susceptibility is dominated by paramagnetic spins. The inset provides a closer examination of the low temperature regime by plotting $1/\chi$ vs. $T$. This examination shows a non-Curie like susceptibility above $T \approx 20$ K. Nevertheless, below $T \approx 20$ K, all data sets linearly approach zero, suggesting that below a certain temperature the tail is affected only by free spins. Therefore, in order to characterize the number and type of spins while ensuring only end-chain spin effects will be observed,

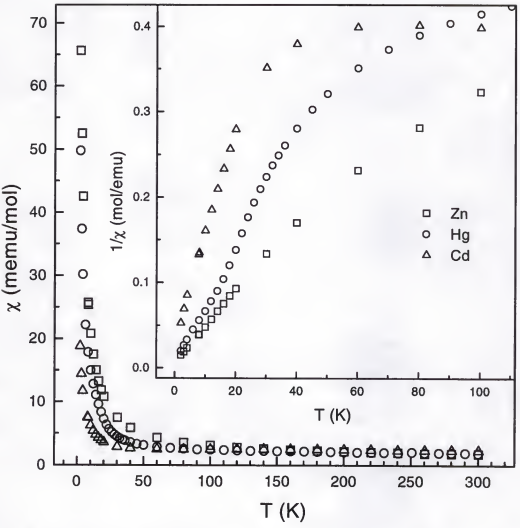


Figure 6.12: $\chi(T)$ for doped NINAZ samples. The doping concentration for each specimen is 0.5% of Cd, Hg, and Zn, respectively. Clearly, a strong paramagnetic increase is observed. The inset shows by a plot of $1/\chi$ that there is more detail to the lowest temperatures than a simple Curie law.

$M(H, T = 2\,\mathrm{K})$ was measured. Figure 6.13 shows the data fit by Equation 6.2 in a manner similar to the undoped case, and the concentrations of spins are given in Table 6.3. The results are astonishing. For example, the magnetization

| | Hg | Zn | Cd |
|---|---|---|---|
| $N_{1/2}$ | $11.6 \pm 0.2$ | $31.3 \pm 0.1$ | $7.0 \pm 0.2$ |
| $N_1$ | $0.54 \pm 0.03$ | 0 | $0.24 \pm 0.03$ |

Table 6.3: Percentage of sample that is the $S = 1/2$ and $S = 1$ paramagnetic contribution for the doped samples of NINAZ from the $M(H, T = 2\,\mathrm{K})$ data (Figure 6.13) and its analysis described in the text.

of a sample doped with only 0.5% Zn implies that approximately 1/3 of the Ni sites are paramagnetic $S = 1/2$ entities. This analysis suggests that the dopant enhances the shattering process, since the simple idea would be that the 0.5% doping would simply add to the $< 0.1\%$ breaks from the shattering process. The concentrations in Table 6.3 suggest average chain lengths of approximately 30, 17, and 6 sites for Cd, Hg, and Zn doped samples, respectively. If this analysis is valid, then chains in the doped samples are clearly short enough to observe interactions between end-chain spins mediated through the chain. In addition, the Zn doped samples should show evidence that a majority of chains are shorter than the correlation length. Furthermore, the size of the paramagnetic tails agree with the tails observed in the numerical work of Yamamoto *et al.* [24] for short chains. Another indication for chains shorter than the correlation length is the destruction of the Haldane phase. No bumps or kinks that can be associated with the Haldane gap are observed in the inset of Figure 6.12 for the Zn doped sample, suggesting that the chain length is shorter than the correlation length.

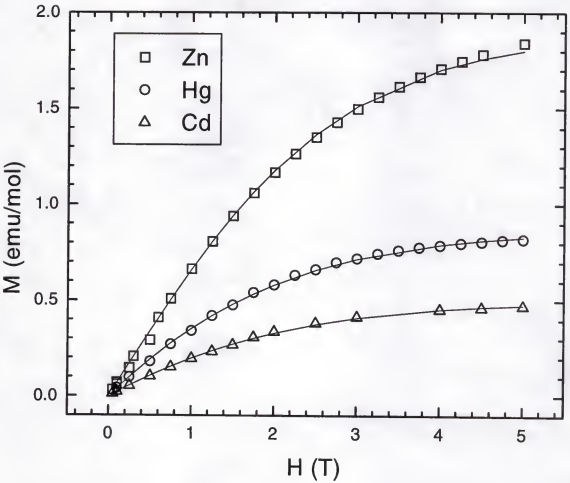


Figure 6.13: $M(H < 5\,\mathrm{T}, 2\,\mathrm{K})$ for doped NINAZ samples. The doping concentration for each sample is 0.5% of Cd, Hg, and Zn, respectively.

However, for the Hg doped sample, where chains are supposedly a factor of 5 longer, a kink is observed around 20 K, consistent with a hint of the Haldane gap. Nevertheless, caution should be taken when assigning any effects in these samples to end-chain spins because a small amount of dopant causes a large increase in the number of paramagnetic spins, and neither the Cd, Hg, nor Zn materials are a non-magnetic isomorph of NINAZ. Consequently, the simple explanation of the above features is that the material is not a chain system. Further clarification of these points is needed before a definite statement can be made. Some helpful information is provided by the ESR measurements, but careful crystal structure refinement of the low temperature phases of doped NINAZ are required. Unfortunately, this test is extremely difficult to perform as even the low temperature phases of the pure material have not yet been identified.

### 6.3.4 Microscopic Measurements: Electron Spin Resonance

Macroscopic measurements alone are insufficient to confirm the existence of the end-chain spins predicted by Affleck, Kennedy, Leib and Tasaki [13]. We used the microscopic measurement of electron spin resonance (ESR) to provide the needed additional information. Most of the work was performed with a resonant spectrometer working at $\nu = 9.25$ GHz, and preliminary studies were performed with a transmission spectrometer at 98 and 189 GHz. These frequencies avoid transitions from other physical phenomena besides end-chain spins because the smallest energy scale for the chains in NINAZ is $D \approx 440$ GHz.

Central to an ESR experiment is the absorption spectrum. The simplest spectrum contains a single peak, but if there is an anisotropic magnetic or electric

environment, then subtle energy shifts may cause multiple peaks. In the measurements on NINAZ, the polycrystalline samples exhibited three peaks, the powder samples exhibited a single peak, and the doped samples exhibited five peaks. Therefore, a discussion of the origin of the observed peaks is provided before the properties of the peak associated with the end-chain spins are discussed.

Figure 6.14 shows ESR lines at 4 K for polycrystalline, powder and ultrafine powder samples. The predominant feature is the central peak which is attributable to end-chain spins with an observed g value of 2.174. This result agrees with $g$ values of $Ni^{2+}$ ions in a paramagnetic environment [169]. Further discussion of the central peak will be provided below. The other dominant feature in Figure 6.14 is an additional peak in the polycrystalline sample, observed as a subtle shoulder at fields slightly above center field, that is absent in the powder and ultrafine powder samples. This peak is attributed to a few neighboring end-chain spins located close enough to each other to permit dipolar coupling. To understand the behavior of each peak independent of the shape of the whole spectra, the polycrystalline line was fit to a sum of standard spectral functions. The best fit was provided by a sum of three Lorentzians as shown in Figure 6.15. The existence of the peak to the left of the central line is debatable since the line shape for end-chain spins is not well determined [57], but comparison with the line shapes of doped samples, given below, suggests that this peak is real. To provide information on the origin of these peaks, the $g$ value of each peak was measured as a function of magnetic field orientation. The magnetic field was applied perpendicular to the chains and the sample was rotated $180^o$ about the

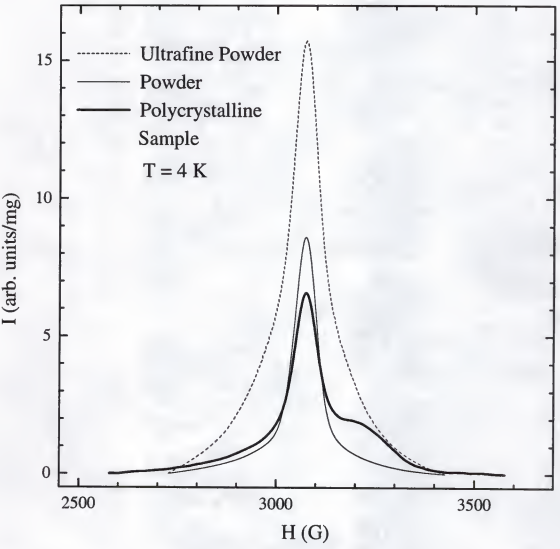


Figure 6.14: Typical ESR lines for polycrystalline, powder and ultrafine powder samples of NINAZ at $T = 4$ K [168]. The central peak is attributed to the end-chain spins, and the subtle shoulder in the polycrystalline data is attributed to a few neighboring end-chain spins located close enough to each other to permit dipolar coupling, as is discussed in the text.

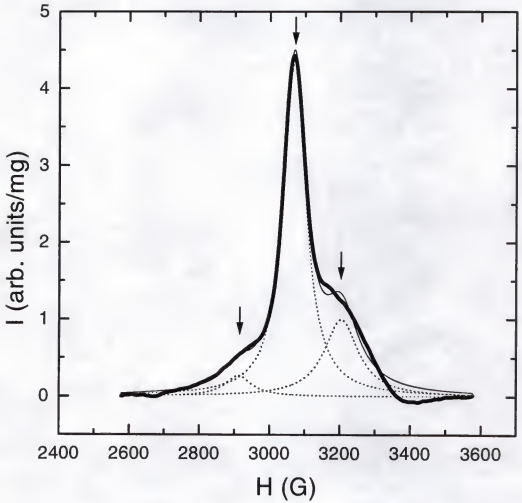


Figure 6.15: ESR line for a polycrystalline sample of NINAZ from Batch 1 of NINAZ at $T = 4$ K. The fine line is the result of a fit to three Lorentzians (dotted curves), as described in the text. The arrows indicate the maximum of each Lorentzian.

chain axis in 15° increments, providing the spectra plotted in Figure 6.16. The angle is measured from an arbitrary zero. If the ESR peaks produced a significant shift, an appropriate fit would fix the zero. Clearly, there are no large shifts in the ESR peaks as a function of rotation angle. The $g$ value of each peak as a function of angle is plotted in Figure 6.17. For the largest $g$ value, there is no observed shift within the noise of the data. For the other two peaks, the shifts are $< 1\%$ of the resonance field, suggesting nuclear moments as their origin. The absence of a shift from electronic moments indicates that the end-chain spins see an effectively isotropic local magnetic environment, eliminating the possibility that this line results from dipolar coupling to extrinsic sources. In addition, if the side peaks originated from a staggered magnetization, as is observed in the spectra of doped NENP [110,118], the line shape would change substantially when rotated. Another property of the side peaks is that they are crystal specific and dependent on the number of thermal cycles through the shattering transition, as can be seen by comparing the spectra in Figures 6.15, 6.16, and 6.20 – 6.23. These facts indicate that the side peaks result from the shattering process. The reason why corresponding spectral weight is not observed in the wings of the powder or ultrafine powder line shapes is that the pulverizing processes homogenize the sample, thereby drastically reducing the intensity of the peaks due to interactions between neighboring end-chain spins. In summary, the only remaining explanation for the side peak is that it arises from a few neighboring end-chain spins located close enough to each other to permit dipolar coupling.

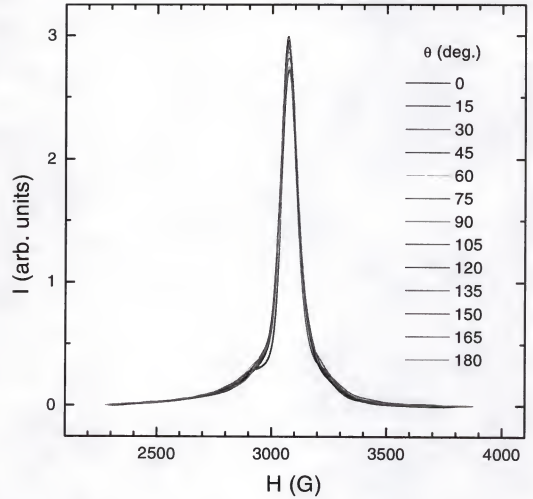


Figure 6.16: ESR spectra for a polycrystalline NINAZ sample as a function of angle about the chain axis at $T = 4$ K. The sample is from Batch 2. Any shift in the ESR peaks can be accounted for by interactions with nuclear moments.

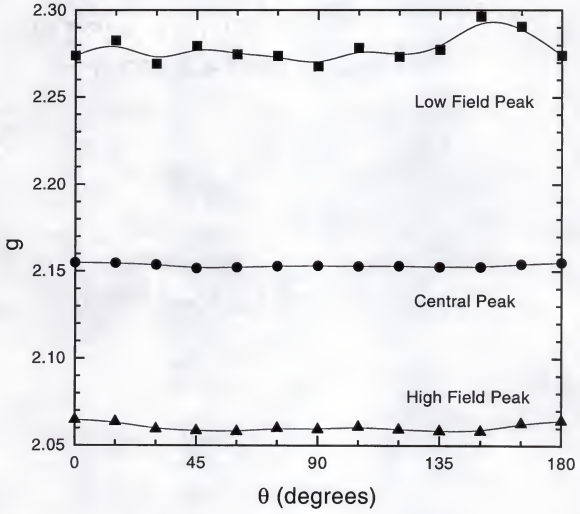


Figure 6.17: ESR peak $g$ values as function of angle in a polycrystalline sample. The angle is measured about the chain axis, with an arbitrary zero as explained in the text. Any slight shift with the $\theta$ can be attributed to interactions with nuclear magnetic moments. Notice there is no significant line shift with rotation. The lines are guides for the eyes.

Another way to experimentally test the line shape of pure NINAZ is to compare it to the line shape of doped samples. Figure 6.18 shows the ESR spectra for Hg doped NINAZ with a fit to five Lorentzians. The reason for choosing this fit will be provided below. Several features not observed in the polycrystalline samples are observed in the doped sample. First, doping has increased the number of observed peaks in the spectra. This result emphasizes that the dopant affects the crystal in a more complex way than simply breaking chains. One possible explanation of the additional lines is that the side peaks in the polycrystalline line are split by an added dipolar or crystalline field. This explanation is supported by the fact that peaks A and E are of nearly equal size and position away from the center line. Furthermore, peaks B and D have similar intensities and are shifted away from the center line by equal amounts. If the two pairs correspond to a splitting, then each member of a pair should shift in a complimentary manner to the other member when the direction of the applied magnetic field is changed with respect to the local field. To test this explanation, the sample was rotated about the chain axis which was oriented perpendicular to the magnetic field at $T = 4$ K. Figure 6.19 shows the orientational dependence of $g$. Peak A shifts, but peak E does not, suggesting that they are of different origins. The behavior of peaks B and D is less definitive. Peak B shifts, as a function of $\theta$, by amounts above the scatter of the data. However, the deviations away from the $g$ value at $\theta = 0$ for peak D may or may not be above the scatter of the data. Therefore, the only conclusion that can be made from these rotation studies is that there are several sources of local magnetic fields in the doped samples that are absent

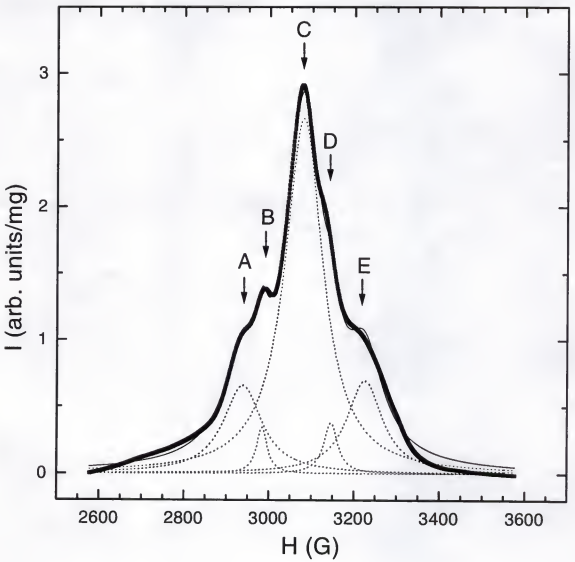


Figure 6.18: Hg doped NINAZ ESR spectrum at $T = 4$ K. Also included is the fit to the five Lorentzian curves. The fit is the narrow line, and each dotted line is an individual Lorentzian. An arrow indicates the maximum of each Lorentzian, which is labeled as A, B, C, D, and E.

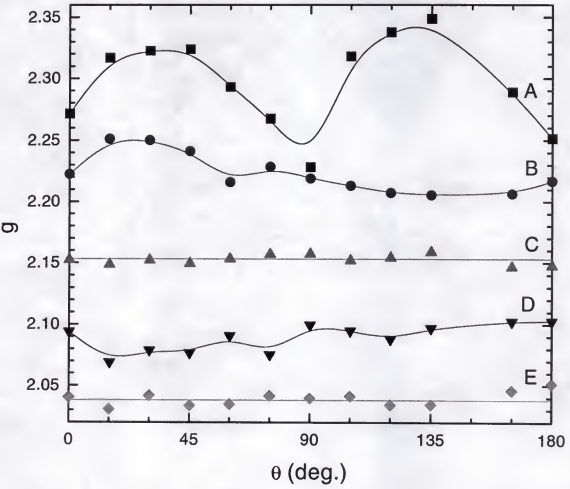


Figure 6.19: Hg doped NINAZ ESR peak $g$ values as function of angle around the chain axis. Each curve is labeled according to the corresponding peak in Figure 6.18. The lines are included as guides for the eye. A description of the shift of the lines with the largest $g$ values is given in the text.

from the pure samples. This conclusion provides more evidence that the dopants have a greater effect than simply breaking the chains.

Another interesting feature of Figure 6.18 is observed by comparing the size of the resonance spectrum with a similar spectrum in the polycrystalline sample (Figure 6.15). The same arbitrary units are used in both figures. The size (*i.e.* the intensity) is the same to within at least an order of magnitude. However, the $M$ vs. $H$ measurements described previously demonstrated a difference in the number of spins by four orders of magnitude. This distinction between the macroscopic and microscopic measurements can be explained by interactions of the magnetic excitations on the chains with the end-chain spins. These interactions shift the ESR line beyond magnetic fields observable by our apparatus. A full discussion of this effect is provided below. In summary, the doped samples exhibit numerous ESR lines which may have a variety of origins. Nevertheless, a significant central peak is present and is consistent with the $S = 1/2$ end-chain peak in the pure samples. In addition, all the spectral weight attributable to the number of end-chain spins obtained with $M$ vs. $H$ measurements is not observed. This result is consistent with the model that the interaction between end-chain spins and the magnetic excitations has shifted it beyond the limits of the experiment.

More information of the microscopic properties of the system can be obtained by the properties of the central ESR peak. There are primarily three properties used to quantify the interpretation of ESR peaks: the intensity, the area under the data, and the line width. Typically, the area is related to the number of

paramagnetic spins in the system, but for Haldane gap systems, the number of spins participating in the observed ESR line is related to the number of thermally excited magnetic excitations on the chain [57]. For this reason, the area under the curve is only approximately proportional to the number of spins and provides no better than an order of magnitude estimate when a calibration is attempted. Furthermore, thermally excited magnetic excitations affect the line width differently than the intensity which causes the area and the peak maximum to be disproportionate [57]. Therefore, the intensity of the ESR spectrum should be quantified by its maximum.

Qualitatively, the ESR signals for polycrystalline, powder, and ultrafine powder samples demonstrate an increase in intensity and line-width for a decrease in chain length (Figure 6.14). To provide a quantitative analysis of these features, comparisons are made to the theory of Mitra, Halperin and Affleck [57] as outlined in Section 2.4.1. Their most easily tested result is the temperature dependent intensity. To test this prediction, we measured the temperature dependence of the ESR signal from 4 K up to the temperature where the signal was unobservable for all the samples. Figures 6.20, 6.21, 6.22 and 6.23 show the ESR lines for both batches of polycrystalline sample with $H$ parallel and perpendicular to the chains, respectively. Clearly, all lines show a temperature dependence. Figures 6.24 and 6.25 show the temperature dependent intensity for both batches of the polycrystalline sample with $H$ parallel and perpendicular to the chains, respectively. Theoretical fits of these data are not meaningful because the error bars are so large, and the side ESR peak plays a significant

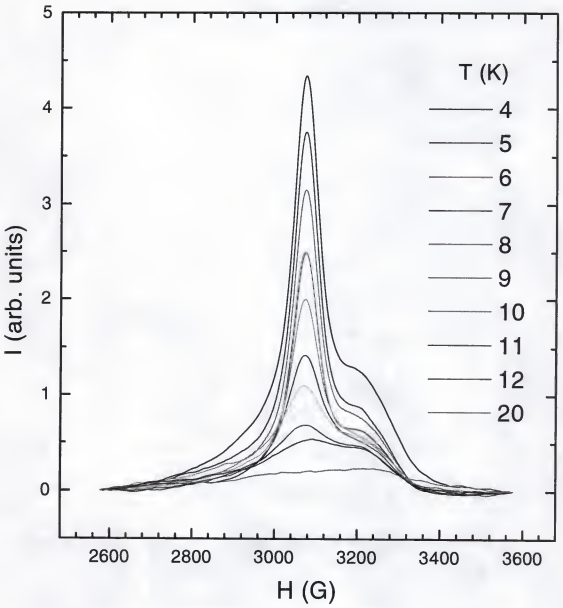


Figure 6.20: $T$ dependence of ESR lines for $H \perp$ to the chains of a NINAZ polycrystalline sample from Batch 1.

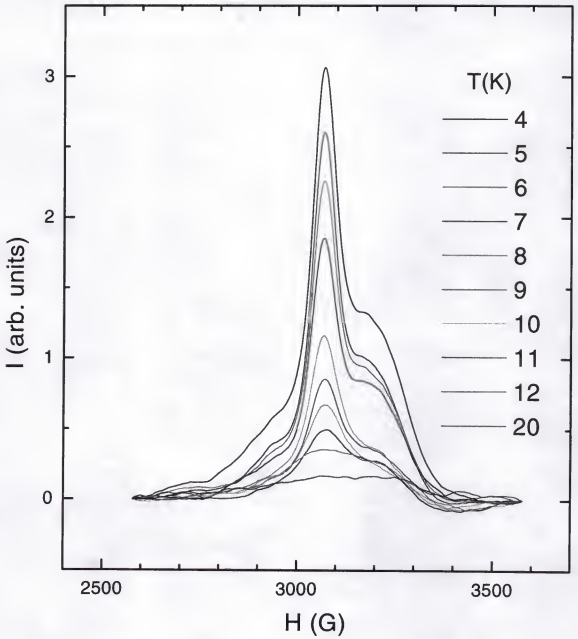


Figure 6.21: $T$ dependence of ESR lines for $H \parallel$ to the chains of a NINAZ polycrystalline sample from Batch 1.

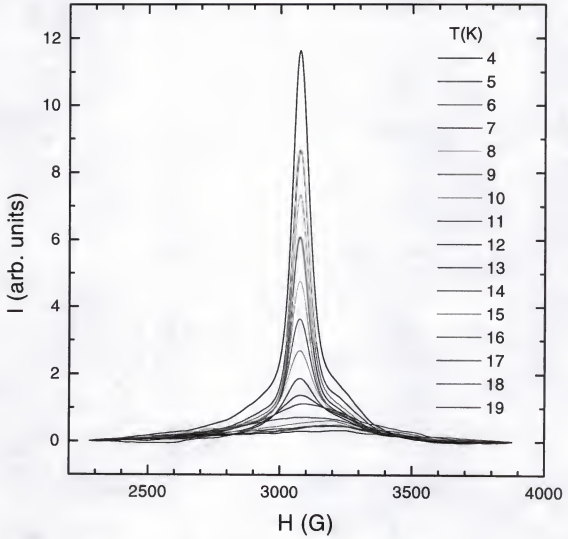


Figure 6.22: $T$ dependent ESR spectra for $H \parallel$ to the chains of a NINAZ polycrystalline sample from Batch 2.

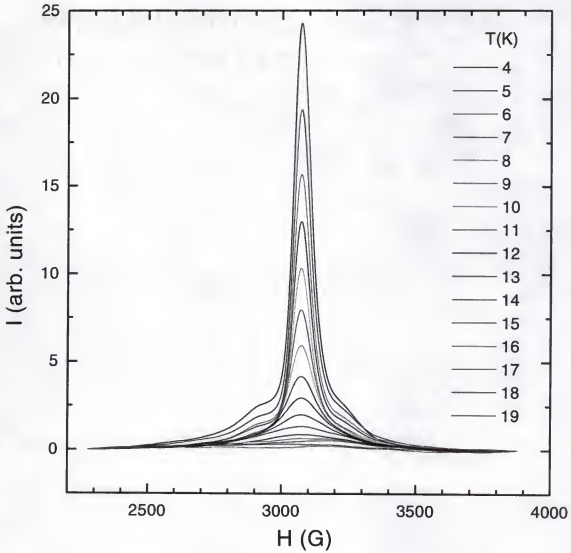


Figure 6.23: $T$ dependence of ESR lines for $H \perp$ to the chains of a NINAZ polycrystalline sample from Batch 2.

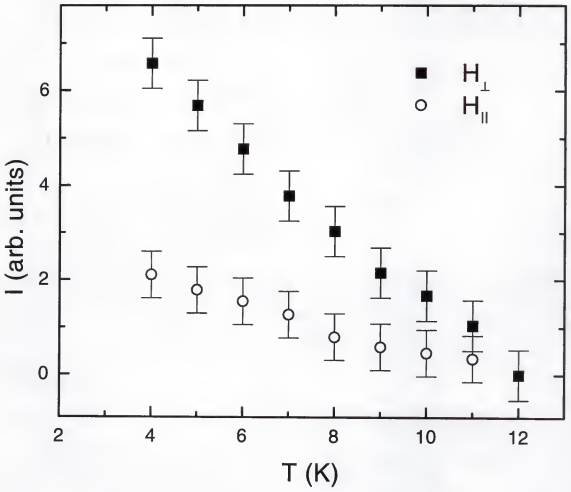


Figure 6.24: ESR $I(T)$ for a NINAZ polycrystalline sample from Batch 1. Both orientations of magnetic field are shown. The data are highly affected by the side peaks, and therefore any assignment of differences between orientations is questionable.

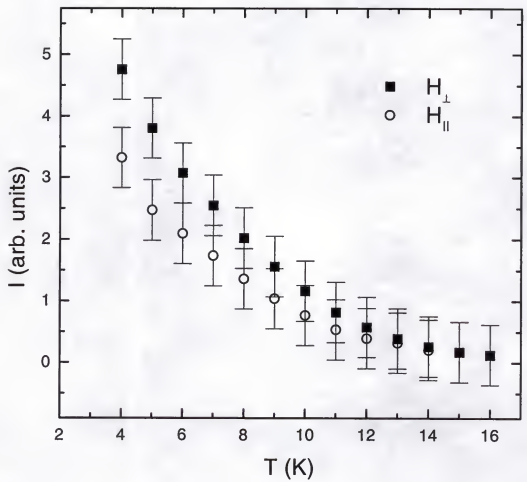


Figure 6.25: ESR $I(T)$ for a NINAZ polycrystalline sample from Batch 2. Both orientations of magnetic field are shown. Again the data are somewhat affected by the ESR side peak.

role. The differences between the data for Batch 1 and Batch 2 show the effect of the side peak contribution. The increased mass of the powder and ultrafine powder samples (64 mg in each case) greatly improves the signal to noise ratio, and the brutal breaking procedures eliminate the side peaks. Figures 6.26 and 6.27 show the ESR lines as a function of temperature for the powder and the ultrafine powder samples, respectively. Again for easier analysis, Figure 6.28 shows the temperature dependent intensity of the ESR lines. The solid lines show fits to Equations 2.26 – 2.25, using the materials parameters given in Section 6.2. The fitting results in average chain lengths of $1600 \pm 50$ sites ($\sim 0.9\ \mu m$) for the powder and $920 \pm 50$ sites ($\sim 0.5\ \mu m$) for the ultrafine powder. Comparison with the particle size analysis (Figures 6.4 and 6.5) shows that the pestle and mortar grinding process does not reduce the average chain length below the length of the polycrystalline domains [156], whereas ball milling produces chains of a length consistent with the particle size.

The other major feature of an ESR spectrum is its line width. To quantify the line width, the full width at half maximum (FWHM) is measured from Figure 6.14, to be $80 \pm 10$ G, $70 \pm 1$ G, and $100 \pm 1$ G, for the polycrystalline, powder, and ultrafine powder samples, respectively. Clearly the line broadens as NINAZ is pulverized. As described in Section 2.4.1, Mitra, Halperin, and Affleck propose two mechanisms [57] which may influence the line width. First, bosons changing energy levels could affect the line width, where this change in energy is quantized in units of $\delta\epsilon$ as given by Equation 2.23. Using the materials parameters cited previously, $\delta\epsilon \approx 1$ kG for the powder sample and 3 kG for the

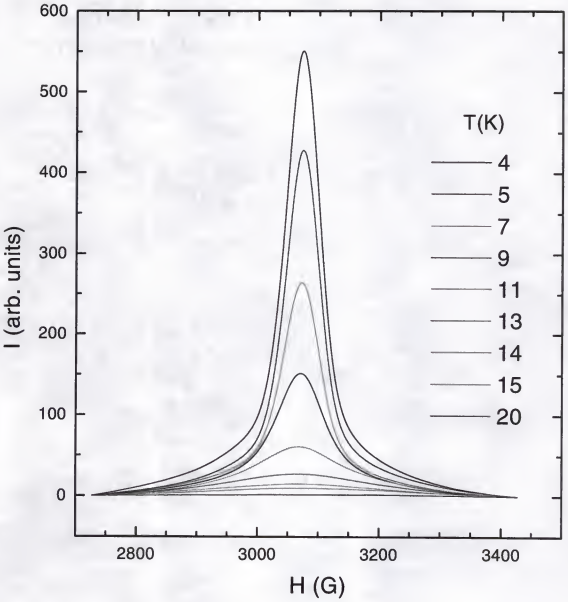


Figure 6.26: $T$ dependence of the ESR line for a powder sample of NINAZ from Batch 1.

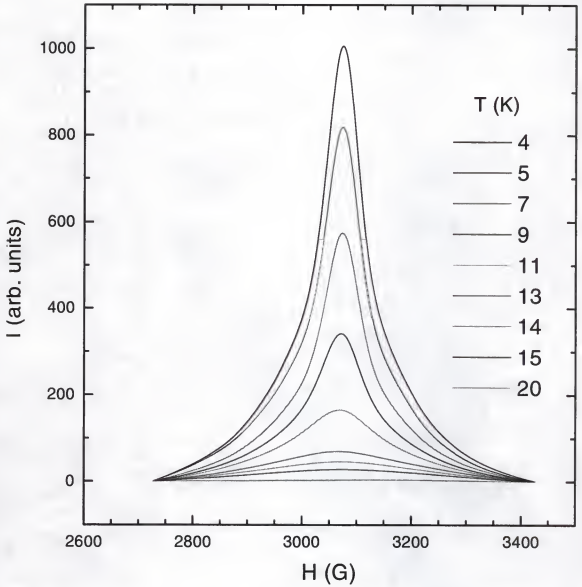


Figure 6.27: $T$ dependence of the ESR line for an ultrafine powder sample of NINAZ from Batch 1.

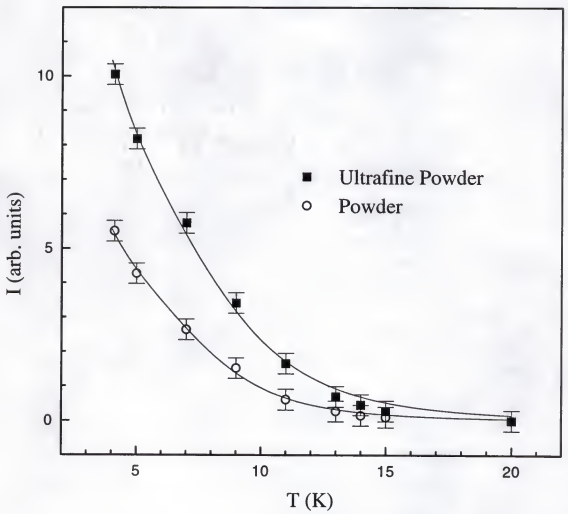


Figure 6.28: $I(T)$ for powder and ultrafine powder NINAZ samples [168]. The solid lines are fits to Equation 2.26

ultrafine powder sample. These estimates of $\delta\epsilon$ are two orders of magnitude too large to explain the line widths shown in Figure 6.14. Nevertheless, this mechanism could cause ESR lines at fields not shown in Figure 6.14. Figure 6.29 shows the energy level diagram as a function of magnetic field for three boson levels in the powder sample. The arrows indicate all the allowed transitions. The heavy arrow indicates the transition where the boson does not change energy levels. The open-ended arrows indicate transitions involving the upper energy level. The closed-ended arrows indicate transitions involving the lower energy level. All arrows are of the length $\nu = 9.25$ GHz, *i.e.* the frequency of the microwave radiation. If transitions from bosons changing energy levels exist, they are either near 2 or 4 kG. However, since these processes involve the creation of a boson on the chain as well as flipping the end-chain spin, they are second order processes and should have a reduced intensity. Therefore, it is not surprising that extended magnetic field sweeps through these fields provided no evidence of these transitions nor did preliminary high field ESR experiments to be discussed below. Consequently, similar to NENP [57], this mechanism has not been observed in our study of NINAZ.

The other possible mechanism is a small change in the energy of a boson that experiences a phase shift, $\delta(k)$. As explained in Section 2.4.1, $\delta(k)$ is defined by Equations 2.27 and 2.28 with the parameters $k$, the wave vector, and $\mathcal{D}$, a constant of order 1, respectively. Starting with the energy given by the line widths (Figure 6.14) and the wavevector ($n = 1$) for the appropriate chain lengths, our experimental value of $\mathcal{D}$ is $\approx 5$ for the powder and $\approx 1$ for the ultrafine powder.

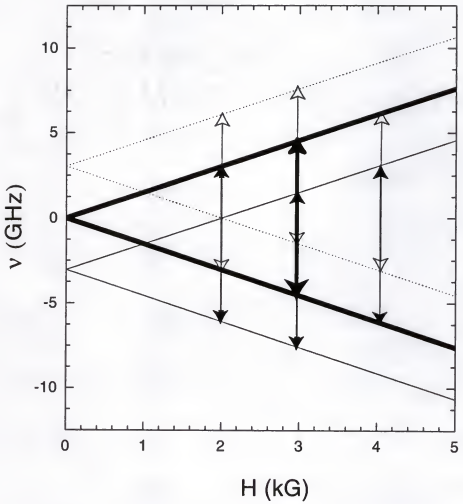


Figure 6.29: Energy level diagram for powder NINAZ showing three boson energy levels. The heavy arrow indicates the transition where the boson does not change energy levels. The open-ended arrows indicate transitions involving the upper energy level. The closed-ended arrows indicate transitions involving the lower energy level. All arrows are of the length $\nu = 9.25$ GHz the frequency of the microwave radiation. A full description of the physical processes is given in the text.

This analysis is in excellent agreement with the theoretical predictions and is the first experimental evidence of magnetic excitations affecting the line width of the end-chain spin. In other words, although typical line broadening processes are still present, the major contribution to the powder and ultrafine powder line widths is the interaction between the magnetic excitations and the end-chain spins. Furthermore, Figure 6.30 shows the FWHM as a function of temperature for the powder and ultrafine powder samples. For both samples, there are two distinct behaviors as a function of temperature. The temperature independent region below 8 K suggests that the excitations that interact with the end-chain spins are due solely to quantum fluctuations. As the temperature is increased above 8 K, the FWHM expands as more thermally excited magnetic excitations are introduced to the chain as is expected by the theory of Mitra, Halperin, and Affleck [57]. This transition of $T^* \approx 8$ K is consistent with a picture of the thermal excitation of magnetic excitations over a barrier of $\Delta$. One might expect a difference in $T^*$ between the powder and the ultrafine powder samples because the different chain lengths cause different energies in the excited state. Unfortunately, this temperature difference should be of the same order as the change in line width between the powder and ultrafine powder sample (25 G $\approx$ 3 mK) which is beyond the temperature resolution of the measurement.

Regardless of the previous analysis, temperature independence alone is insufficient to claim the observation of quantum phenomena. The following arguments will eliminate the other possibilities. The simplest explanation for temperature independence is a line width limited by instrumental resolution, but measurements

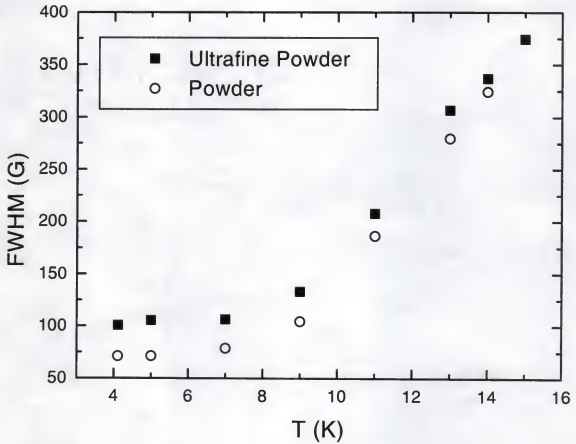


Figure 6.30: ESR FWHM vs. $T$ for powder and ultrafine powder NINAZ from Batch 1. Above $\sim 8$ K, the line width increases as the amount of thermally excited magnetic excitations increases. Below $\sim 8$ K, the number of excitations is limited by quantum fluctuations.

of DPPH show that the linewidth resolution limit is less than 2 G (Figure 4.8). Another possibility is that the sample was no longer coupled to the thermometer, but if this were true, then a temperature independent region would be observed for $I(T < 8\,\mathrm{K})$ (Figure 6.28). Finally, the line width could be limited by the interaction of end-chain spins mediated by the chain, but to produce line widths on the order of 100 G, a majority of the chains must be under a length of 100 sites [57]. Nearly all the chains in our samples are at least an order of magnitude longer than this limit. The only remaining explanation for the temperature independent region in Figure 6.30 is the quantum limit. Therefore, these linewidth results confirm that the $M$ vs. $H$ measurements were performed in the quantum limit.

Further information about this quantum limit is provided by the area under the powder and ultrafine powder curves. As was mentioned in Section 2.4.1, the area under the absorption peak is proportional to the local susceptibility. Figure 6.31 shows the $1/\chi$ data for powder and the ultrafine powder samples, clearly demonstrating that the magnetic susceptibility is more complicated than a simple Curie law. Nevertheless, Figure 6.32 shows that the ratio of the magnetic susceptibility for the powder and the ultrafine powder samples is a constant. Therefore, the magnetic susceptibility can be described by a Curie law multiplied by some function, $f(T)$, which considers the number of end-chain spins not participating in the ESR line because thermally excited magnetic excitations have excited them beyond the experimental limits. To extract $f(T)$, a plot of $\chi \cdot T$ vs. $T$ is shown in Figure 6.33. In a manner similar to the line width in

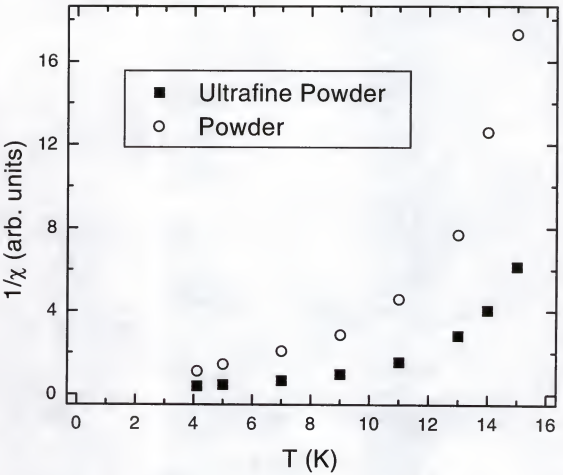


Figure 6.31: $1/\chi$ vs. $T$ for powder and ultrafine powder NINAZ. Clearly, a Curie law is not followed.

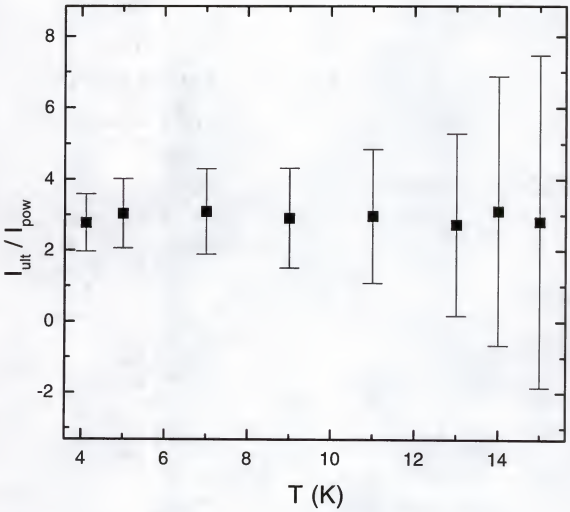


Figure 6.32: The ratio of the area under ultrafine powder data to the area under the powder data for NINAZ as a function of temperature. The value is constant suggesting that $\chi(T) = Cf(T)/T$ as discussed in the text.

Figure 6.30, the data has a distinct change of slope near 8 K. Therefore, $\chi(T)$ can be described by a Curie law below 8 K.

To extend the search for side peaks due to magnetic excitations changing energy levels when interacting with end-chain spins, high field ESR was performed at the National High Magnetic Field Laboratory, on the apparatus described in Section 4.3. Magnetic field sweeps were performed at frequencies of $\nu = 93.934$ GHz and $\nu = 189.866$ GHz. Figures 6.34 and 6.35 are up and down sweeps for 93.934 GHz, and Figures 6.36 and 6.37 are the up and down sweeps for 189.866 GHz. None of the curves show any evidence for other transitions besides the $S = 1/2$ line attributable to end-chain spins. Finally, a comparison of the $g$ values for both the high field and the X-band ESR measurements is provided by Figure 6.38. As the frequency is increased, there is a decrease in the $g$ value. This behavior remains unexplained, and more data are needed to verify it.

*Note added in proof:* Full field sweeps $(0 - 14$ T) for high field ESR at both frequencies show no evidence for $S = 1$ spins. To quantify the resolution of this experiment, the size of the noise was compared to the peak to peak height of the ESR lines in Figures $6.34 - 6.37$. At 93.934 GHz, if more than 100 ppm of the sample were $S = 1$ spins, then a peak would have been observed. Since no peak was observed, the existence of $S = 1/2$ end-chain spins is the only explanation consistent with all the data.

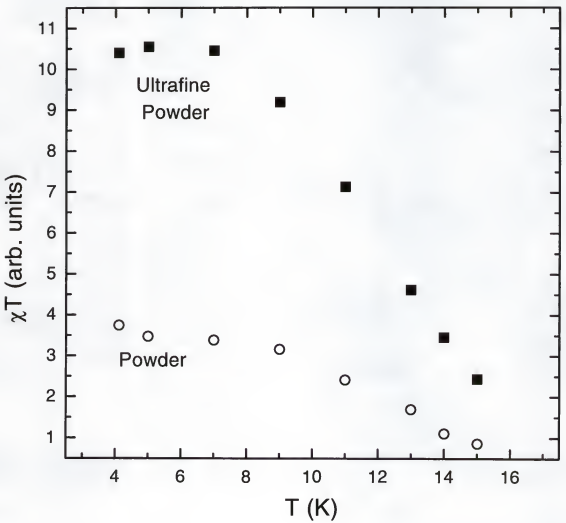


Figure 6.33: $\chi(T) \cdot T$ for the powder and ultrafine powder samples of NINAZ from Batch 1. The high temperature behavior is consistent with the number participating spins controlled by thermally excited magnetic excitations where the low temperature $T < 8$ K behavior is quantum limited.

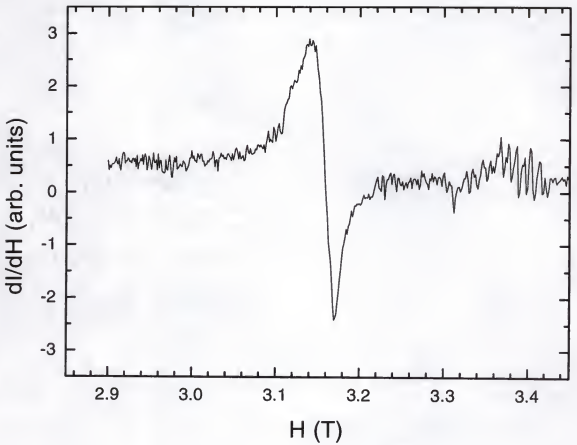


Figure 6.34: NINAZ ESR spectrum at 93.934 GHz, increasing $H$. The samples was from Batch 2. Only the $S = 1/2$ peak corresponding to the end-chain spins is observed. The peaks observed around 3.35 T result from impurities in the sample holder.

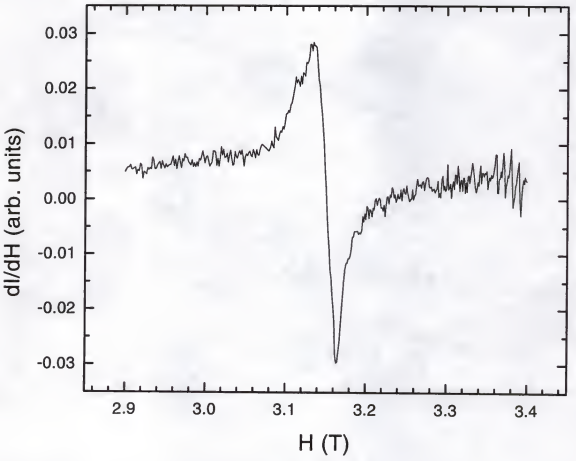


Figure 6.35: NINAZ ESR spectrum at 93.934 GHz, decreasing $H$. The sample is from Batch 2. Only the $S = 1/2$ peak corresponding to the end-chain spins is observed.

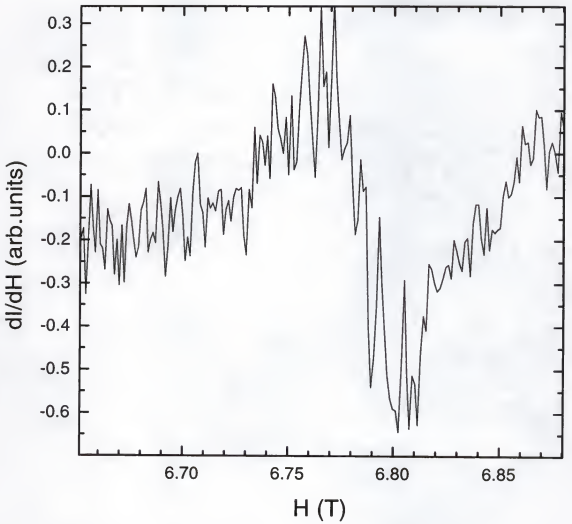


Figure 6.36: NINAZ ESR spectrum at 189.866 GHz, increasing $H$. The sample is from Batch 2. Only the $S = 1/2$ peak corresponding to the end-chain spins is observed.

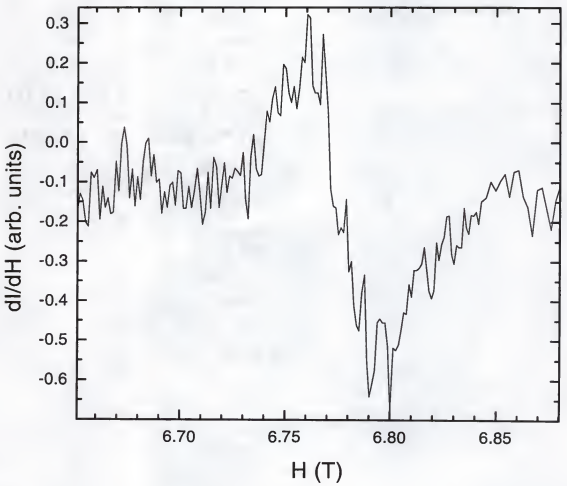


Figure 6.37: NINAZ ESR spectrum at 189.866 GHz, decreasing $H$. The sample is from Batch 2. Only the $S = 1/2$ peak corresponding to the end-chain spins is observed.

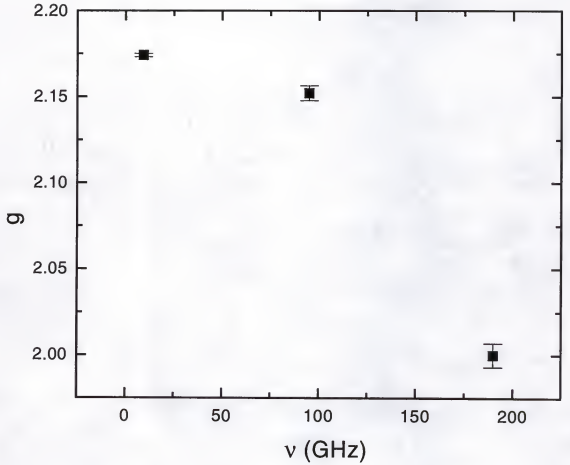


Figure 6.38: $g$ vs. $\nu$ for ESR in a NINAZ powder sample from Batch 2 at $T = 5$ K. The sharp decrease at the highest frequencies remains unexplained.

# CHAPTER 7
# THE $S = 2$ HALDANE GAP IN $MnCl_3$(bipy)

Section 2.3.1 described how the $S = 2$ Haldane gap is small (*i.e.* $\Delta \approx 0.07J$) and highly affected by anisotropies. For our laboratory, the size of the gap is not an issue since we are capable of measurements down to $T \approx 400$ $\mu$K. On the other hand, the theoretically predicted bounds of the single-ion anisotropy required to realize the Haldane state are so small that experimental realization of an $S = 2$ Haldane gap material was doubted. The properties of four materials were tested as potential Haldane gap materials. Azidobis(pentant-2,4-dionato)manganese(III), $Mn(acac)_2N_3$, and (1,10′-phenanthroline)trichloromanganese(III), $MnCl_3$(phen), exhibit long-range order and were excluded from further study. (N,N′-disalicylidene-2-hydroxy-propylenediamine)manganese(III), Mn(salpn)OAc, and (2,2′-bipyridine)trichloromanganese(III), $MnCl_3$(bipy), did not exhibit long-range order. Furthermore, $MnCl_3$(bipy) has a larger $J$ value, so it was chosen for further tests. These tests demonstrated that $MnCl_3$(bipy) is the first $S = 2$ Haldane gap material to be identified.

The first part of the chapter will discuss the structure and synthesis of the aforementioned materials. The rest of the chapter will focus on $MnCl_3$(bipy), since it has properties consistent with the $S = 2$ Haldane gap. First, the macroscopic measurement of magnetization, $M$, vs. magnetic field, $H$, studies will be discussed, and then the results obtained from the microscopic probe neutron scattering will be presented.

## 7.1 $S = 2$ Quasi-linear Chain Materials

All of the materials studied have crystal structures that demonstrate their linear chain nature. Each material, which will be discussed individually, was grown by Brian H. Ward under the direction of Professor Dan R. Talham in the Department of Chemistry at the University of Florida.

### 7.1.1 $MnCl_3(phen)$

The material, $MnCl_3(phen)$, is bridged by Cl atoms, and the chain is spaced by a phenanthroline group, $C_{12}H_8N_2$, as shown in Figure 7.1. Unfortunately, the sample used for the structure refinement was twined, so only an approximate structure was obtained. Nevertheless, the crystal structure was sufficiently refined to confirm the existence of linear chains. Goodwin and Sylva [95] originally measured $\chi(T)$ in the range of $100 - 300$ K and fit their results with a Curie law. However, their work did not extend to low enough temperatures to identify the linear chain behavior of the sample. Therefore, we extended the measurements to $T \approx 2$ K. Figure 7.2 shows the temperature dependent magnetization for a field cooled and zero field cooled sample, and the difference between the two runs. All three traces are consistent with the onset of long-range magnetic order at approximately 22 K. Further work is in progress and will be reported elsewhere.

### 7.1.2 $Mn(acac)_2N_3$

The material $Mn(acac)_2N_3$ has a crystal structure similar to NINAZ, discussed in the previous chapter, with the azido bridge and the ligand spacing the chains.

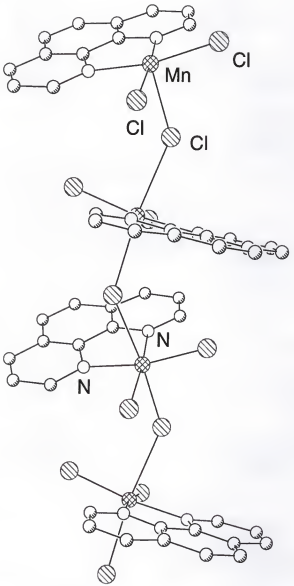


Figure 7.1: Approximate crystal structure of $MnCl_3(phen)$ [170]. The quality of the refinement was hampered by the twined crystal used for the X-ray studies. Nevertheless, the refinement confirms the linear chain nature of the material.

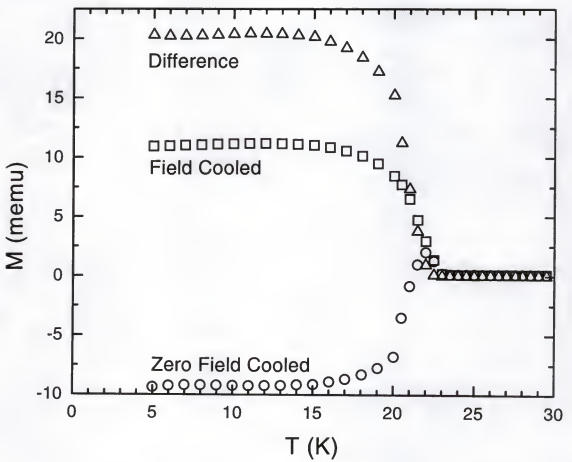


Figure 7.2: $M(T)$ for $MnCl_3$(phen). The measurement was performed on a 44.4 mg powder sample in a magnetic field of 0.01 T using the SQUID magnetometer.

One notable difference between the two materials is that there are no counter ions in $Mn(acac)_2N_3$. The crystal structure [171] is presented in Figure 7.3 which shows a linear chain of Mn ions bridged by the azide ligands and spaced by the acac groups, $C_5H_7O_2$. These same researchers measured the magnetic susceptibility from room temperature to 4 K. They observed broad features characteristic of a 1-D antiferromagnet at high temperatures, but at low temperatures, they saw a few points consistent with a transition to long-range antiferromagnetic order. In an attempt to improve upon their work, we measured the temperature dependence of the magnetization, in a magnetic field of 0.1 T, to test if the features attributed to long-range antiferromagnetic order were sample dependent. Figure 7.4 shows a kink around 11 K in the magnetization of $Mn(acac)_2N_3$. This signature is characteristic of a transition to long-range order and is completely consistent with previous work [171]. No further work is presently planned for this material.

### 7.1.3 Mn(salpn)OAc

The material Mn(salpn)OAc forms linear chains of manganese ions bridged by an OAc group, $CH_3COO^-$, and spaced with salpn ligands, $C_{17}H_{15}N_2O_3$, as shown in Figure 7.5. This crystal structure was solved by Bonadies *et al.* who also performed temperature dependent magnetic susceptibility measurements to 4 K with no evidence of long-range order [172]. Figure 7.6 shows our magnetic susceptibility measurements to $T \approx 2$ K. The inset shows a peak characteristic of 1-D antiferromagnetic correlations at 12 K, which suggests a $J \sim 6$ K. Furthermore, no change between field cooled and zero field cooled measurements supports the

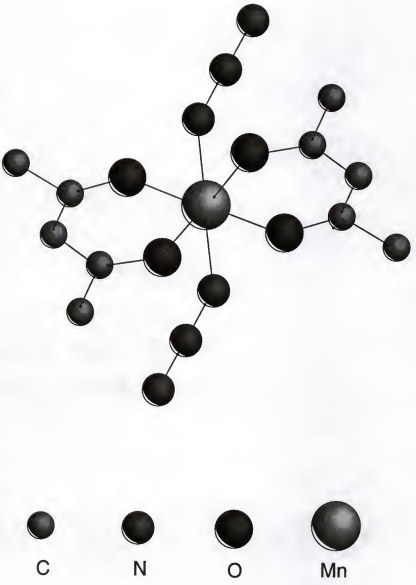


Figure 7.3: Crystal structure of $Mn(acac)_2N_3$ [171].

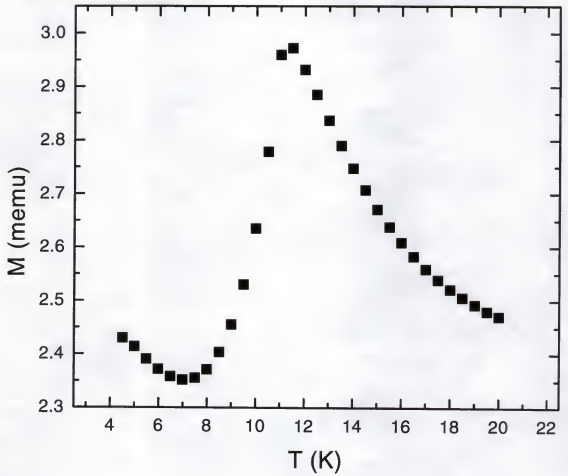


Figure 7.4: $M(T)$ of $Mn(acac)_2N_3$ The measurement was performed on a 40.68 mg powder sample in a magnetic field of 0.1 T using a SQUID magnetometer.

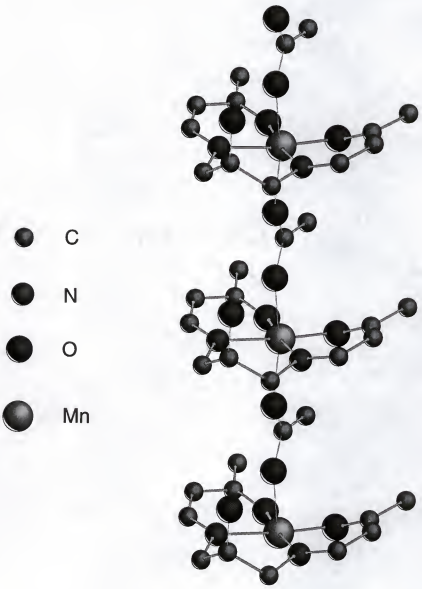


Figure 7.5: Crystal structure of Mn(salpn)OAc [172].

assertion of no long-range magnetic order. Nevertheless, $J$ is quite small, making tests of the gap difficult. Therefore, tests for the gap were first performed with $MnCl_3$(bipy) which, as will be shown below, has a larger $J$. Further research on Mn(salpn)OAc is planned for the future.

### 7.1.4 $MnCl_3$(bipy)

The crystal structure of $MnCl_3$(bipy) was first determined by Perlepes *et al.* [96]. Figure 7.7 shows that the structure, as checked by Ward [170], is very similar to $MnCl_3$(phen). The main difference is that the organic ligand, which spaces the chains, is bipy, $C_{10}H_8N_2$, rather than phen. A careful examination of Figure 7.7 shows a slight staggering of the Mn ions. A comparison of the two structures demonstrates that long-range magnetic order is not a simple function of the size of the organic ligand that spaces the chains since $MnCl_3$(phen), with the larger organic group, exhibits long-range magnetic order while $MnCl_3$(bipy), with the smaller organic group, does not. Extensive work and analysis was performed on $MnCl_3$(bipy); therefore, the magnetic characterization will be discussed in Section 7.2.

### 7.1.5 Synthesis

The materials Mn(salpn)OAc, $Mn(acac)_2N_3$, and $MnCl_3$(phen) were synthesized according to the standard procedures in References [95, 171, 172], and no further discussion will be provided here. On the other hand, $MnCl_3$(bipy) was prepared by the method of Goodwin and Sylva [95], with modifications by Ward [170]. Trimethylchlorosilane was added dropwise to a solution of

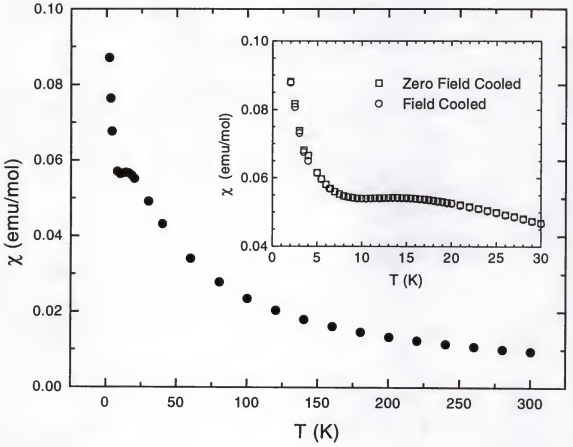


Figure 7.6: $\chi(T)$ of Mn(salpn)OAc. A 30.17 mg powder sample was measured in a magnetic field of 0.1 T using the SQUID magnetometer. The solid black circles are for a zero field cooled measurement. The inset expands the low temperature region for both the field cooled and the zero field cooled runs. No difference is observed between the two runs, suggesting no long-range order. Furthermore, the broad peak reveals a $J \sim 6$ K.

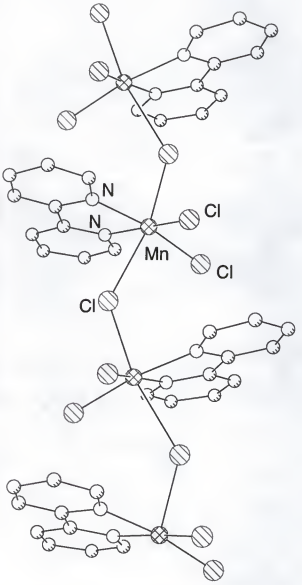


Figure 7.7: Crystal structure of $MnCl_3$(bipy) [96, 170].

$Mn_{12}O_{12}(CH_3COO)_{16}(H_2O)_4 \cdot 2CH_3COOH{\cdot}4H_2O$ in acetonitrile. The resulting solution was filtered, and the filtrate retained. Next, a 2,2′-bipyridine in acetonitrile solution was layered on top of the filtrate. After seven days of undisturbed growth, red crystals of $MnCl_3$(bipy) were filtered out of the solution. The $MnCl_3$(bipy) material was grown first in a protonated form which was used in the macroscopic measurements. For neutron scattering measurements, a fully deuterated specimen is required to reduce the incoherent scattering, as described in Section 4.4. Therefore, starting with 99.98% deuterated materials, several batches of $MnCl_3$(d-bipy) were grown to produce a total of 3 g of material. The magnetic susceptibility as a function of temperature was measured for each batch as a quality check. The typical increase from room temperature down to a value of $J$ was exhibited in all samples although in some samples the low temperature paramagnetic tail became the dominant feature before the peak associated with $J$ was observed. Nevertheless, none of the batches exhibited evidence of long-range magnetic order.

## 7.2 Macroscopic Magnetic Measurements of $MnCl_3$(bipy)

The macroscopic magnetic measurements of $MnCl_3$(bipy) provided the first evidence of a Haldane gap in an $S = 2$ material. Similar to the measurements of the other materials studied, the initial measurements were performed on the SQUID magnetometer as described in Section 4.1. Figure 7.8 shows the temperature dependence of the magnetic susceptibility of a 2.4 mg packet of 90 oriented single crystals for an applied field of 0.1 T. The $\chi(T)$ results show a

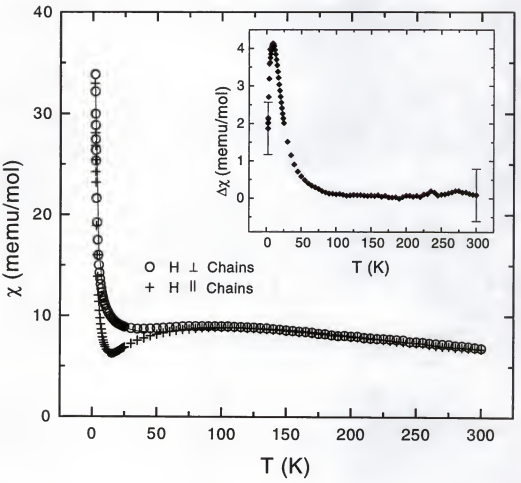


Figure 7.8: $\chi(T)$ of $MnCl_3$(bipy) [97]. A 2.4 mg packet of oriented single crystals was sample used in the measurement which was performed in an applied field of 0.1 T using the SQUID magnetometer. The solid line is a fit to Equation 7.1, where the details are given in the text.

broad peak near 100 K, anisotropy for $T < 80$ K, and a strong upturn at the lowest temperatures. While the broad peak is the expected behavior for linear chain Heisenberg antiferromagnets, the Curie-like increase may be associated with impurities. The anisotropy is such that $\chi_\perp > \chi_\parallel$ which is in contrast to the $Cr^{2+}$ compounds [164, 173] where $\chi_\perp < \chi_\parallel$. Therefore, the anisotropy is not a signature of long-range magnetic order. One possible explanation for this feature is a slight staggered magnetization originating from the staggered Mn positions. Further experimental work is needed to test this hypothesis. Since no explicit expressions exist for $\chi(T)$ of an $S = 2$ linear chain Heisenberg antiferromagnet over a broad temperature range that includes anisotropy terms, we have fit the data of Figure 7.8 to

$$\chi(T) = \chi(0) + C/T + \chi_{LCHA}(S = 2, g, J, T), \tag{7.1}$$

where $\chi_{LCHA}(S = 2, g, J, T)$ is given by Equation 2.12. Another possible expression for $\chi_{LCHA}(S = 2, g, J, T)$ is given by a high temperature expansion of Yamamoto [174]. Unfortunately, he only calculated two terms in the expansion which are not enough for a good fit below $7J$, as shown in Reference [174]. Furthermore, to take advantage of the Padé approximates technique, at least one more term is required. Therefore, Equation 2.12 is the best expression available to date. Since this expression for $\chi_{\mathrm{LCHA}}(S = 2, g, J, T)$ is not expected to be valid when significant anisotropy is present or in a region where a gapped phase might exist (*i.e.* $T < J$), the fitting procedure focused primarily on the region $T > 80$ K, with the exception that the Curie constant $C$ was adjusted to the low

temperature data. The results of the fit, shown by the solid line in Figure. 7.8, yield $\chi(0) = 0.0 \pm 0.5$ memu/mol, $C = 47.5 \pm 0.5$ memu K/mol, $J = 34.8 \pm 1.6$ K and $g = 2.04 \pm 0.04$. The Curie constant could be explained by a small concentration of impurity spins. However, we want to be careful about making this assignment and trying to subtract this "Curie-tail." For example, as previously mentioned, we know that $\chi_{\mathrm{LCHA}}(S = 2, g, J, T)$ is an inadequate description of $\chi(T)$ in this region. Nevertheless, it is noteworthy that various attempts to subtract a reasonable Curie-like contribution always give $\chi(T) \to 0$ as $T \to 0$. To further explore the nature of the magnetic signal at the lowest temperatures, standard 9 GHz ESR was performed on a packet of 5 oriented crystals from 4 to 60 K. The observed signal at 4 K is consistent with a concentration of approximately $0.05 \pm 0.03\%$ $Mn^{2+}$ spins ($S = 5/2$, $g = 2$) that follow a Curie temperature dependence as shown in Figure 7.9. The signal may also contain contributions from trace amounts (at the ppm level) of $S = 3/2$ and $S = 1/2$ extrinsic impurities. However, since the concentration of ESR visible spins is more than an order of magnitude smaller than needed to explain the static susceptibility data, we consider isolated $Mn^{3+}$ ions not in the chain environment and $S = 1$ end-chain spins [35, 37] as the most likely sources of the low temperature behavior.

Since the magnetic susceptibility reveals no evidence for long-range magnetic order in $MnCl_3$(bipy), the next step is to test for the existence of the Haldane gap. To this end, field dependent magnetization measurements were performed at the lowest attainable stable temperature on the SQUID magnetometer. The magnetization for the sample oriented both perpendicular and parallel to the chains

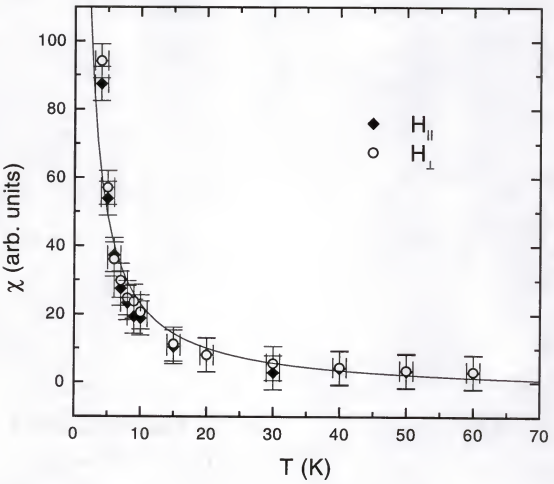


Figure 7.9: 9 GHz ESR signal intensity vs. $T$ for $MnCl_3$(bipy). The solid line shows, that within the error bars, the data follow a Curie law. The sample consisted of 5 oriented single crystals providing a total mass of approximately 500 $\mu$g.

(Figure 7.10) shows strong backgrounds consistent with free spins that saturate at high magnetic field but no clear evidence of a Haldane gap. Nevertheless, if the two sets of data are subtracted from each other, a small hint of a thermally smeared Haldane gap appears (inset of Figure 7.10), but to obtain convincing evidence, measurements at lower temperatures were required.

The cantilever magnetometer at the National High Magnetic Field Laboratory in the top-loading dilution refrigerator was a clear choice for this measurement. The sample was mounted on the cantilever with a small amount of vacuum grease. The cantilever and sample were inserted into a top loading dilution refrigerator to run at a temperature of 30 mK as described in Section 4.2. In an attempt to maximize the signal, initial sweeps were made on three single crystals. Unfortunately, the magnetic response of the sample was so strong that the cantilever was driven into a non-linear region at fields close enough to the critical field to obscure any gap features, as evidenced by the continuous curving of the data from point A to point B as shown in Figure 7.11. Furthermore, point B labels the feature characteristic of the cantilever behaving so nonlinearly as to enter a "blocked" region. To circumvent this problem, a second run was performed on a single crystal. Figure 7.12 shows that the resultant data were dominated by a diamagnetic background. Nevertheless, there is a discontinuity between 1 and 2 T, where the diamagnetic contribution becomes less pronounced, suggesting that a magnetic state above the Haldane gap is competing with the background. Finally, two single crystals were used and provided data that were dominated by neither background nor nonlinear effects. Nevertheless, a diamagnetic term had to be subtracted from the data.

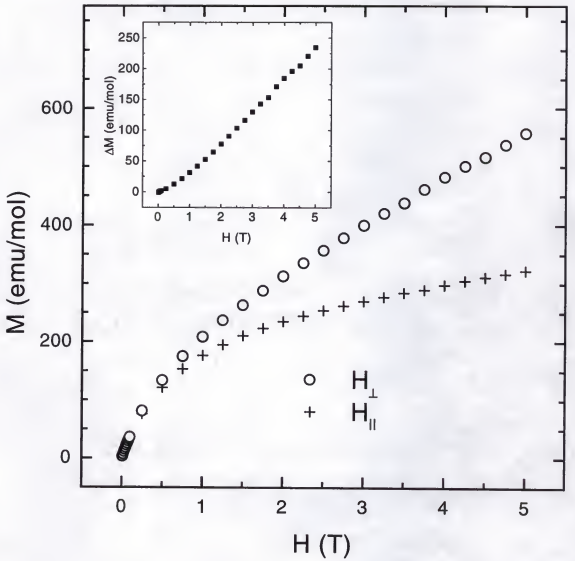


Figure 7.10: SQUID $M$ vs. $H$ measurement of $MnCl_3$(bipy). H was oriented both parallel and perpendicular to the chain axis at $T = 2$ K. The inset shows $\Delta M = M_\perp - M_\parallel$.

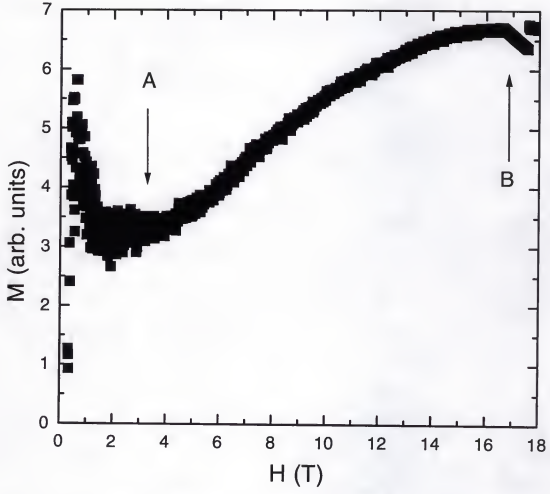


Figure 7.11: Raw $M$ vs. $H$ data for three oriented single crystals of $MnCl_3$(bipy) measured with the cantilever magnetometer. Notice the continuous curve between points A and B showing non-linear behavior over the whole field region. Furthermore, point B labels the characteristic feature of a blocked region caused by extreme nonlinearities in the system.

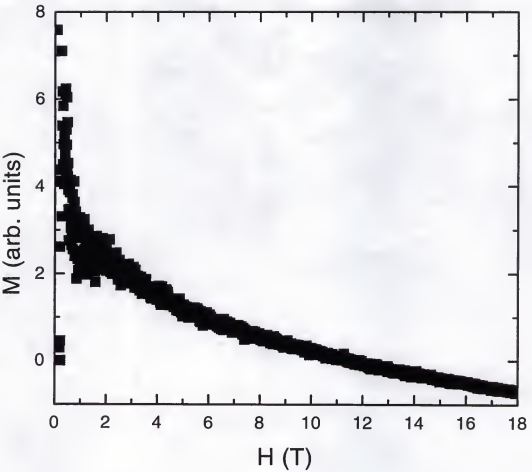


Figure 7.12: Raw $M$ vs. $H$ data for one crystal of $MnCl_3$(bipy) using the cantilever magnetometer at $T = 30$ mK. The data are clearly dominated by a strong diamagnetic background. Nevertheless, the discontinuity between 1 and 2 T is suggestive of a Haldane gap.

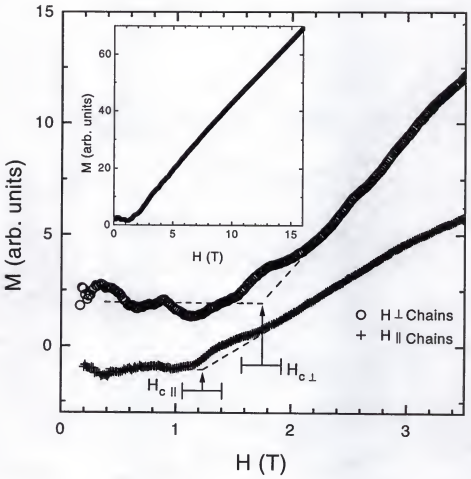


Figure 7.13: $M$ vs. $H$ data for two oriented crystals of $MnCl_3$(bipy) from the cantilever magnetometer at $T = 30$ mK [97]. A diamagnetic background was removed by the procedure described in the text. Data are presented for magnetic field oriented both parallel ($\|$) and perpendicular ($\perp$) to the chain. For each orientation, a critical field is observed providing evidence of the Haldane gap in an $S = 2$ antiferromagnetic chain. The inset shows the data for $H\perp$ chains to 16 T. This trace shows no bumps or kinks that would indicate non-Haldane phase behavior. A full discussion as to why these features can only be associated with a Haldane gap is given in the text.

Since the region below the critical field should exhibit a constant magnetization, any low field slope could be assigned to the diamagnetic background alone. A fit to all the 30 mK data runs using the two crystals provides a diamagnetic term of $M_D(H) = -2.968H$, where the units are the same arbitrary units given in Figure 7.13. The consistency of this diamagnetic correction for the two crystal orientations suggests that this term is independent of the sample since it does not change scale like the properties associated with the Haldane gap. With this diamagnetic term removed, Figure 7.13 clearly shows evidence of critical fields for magnetic fields applied both parallel ($H_{c||} = 1.2 \pm 0.2$ T) and perpendicular ($H_{c\perp} = 1.8 \pm 0.2$ T) to the magnetic fields. These critical fields are the first evidence for a Haldane gap in an $S = 2$ material. Using the values for these critical fields, Equations 2.14 and 2.15, and $g = 2.04 \pm 0.04$, the two gaps are determined to be $\Delta_{||} = 3.7 \pm 0.9$ K and $\Delta_{\perp} = 1.6 \pm 0.3$ K. These orientationally dependent gap values, $S = 2$, $\kappa = 2$, and Equations 2.16 and 2.17 yield an isotropic Haldane gap of $\Delta = 2.3 \pm 0.8$ K and a single-ion anisotropy of $D = 0.3 \pm 0.1$ K. For comparison to the theoretical predictions, the gap and single-ion anisotropies are best written in units of $J$. For $MnCl_3$(bipy), $\Delta/J = 0.07 \pm 0.02$ and $D/J = 0.010 \pm 0.003$, when $J = 34.8 \pm 1.6$ K. The gap value is in excellent agreement with the numerical predictions [34, 35, 37–39], and the value of the single-ion anisotropy places $MnCl_3$(bipy) inside the Haldane phase region (see Figure 2.9). Further comparison with other regions of this diagram show that the Haldane region is the only one consistent with all the experimental data. First, the XY phase is gapless, so the existence of critical fields demonstrates that the system is not in this region.

Second, if the system was in the large D phase, critical fields would be observed in both orientations, but they would be much farther apart in magnetic field. Third, if the material was in a long-range antiferromagnetically ordered state, one of the traces would remain zero until a spin-flop field $H_{SF}$ was achieved [54, 58]. From standard theory [54],

$$H_{SF} = \frac{S}{g\mu_B}\sqrt{4SDJ}. \tag{7.2}$$

Therefore, assuming the single-ion anisotropy is the value provided from the Haldane analysis, $H_{SF} \approx 14$ T. Clearly, this critical field would have been observed in the inset of Figure 7.13, and if $D$ was any larger, evidence of long-range order would have been observed in the SQUID results. The last alternative explanation for discontinuities in $M(H)$ is an effect resulting from saturation of the chain. The saturation field is given by $H_s = g\mu_B SJ$, which for $MnCl_3$(bipy) is 210 T. Clearly, this field is too high to cause an effect at 2 T. None of these alternative explanations are consistent with the experimental data. Therefore, magnetization as a function of magnetic field provides the first confirmation of the Haldane gap in an $S = 2$ system.

## 7.3 Low Temperature Crystal Structure: Preparation for Microscopic Measurements

To provide a direct measure of the Haldane gap in $MnCl_3$(bipy), a microscopic probe is required. The microscopic probe chosen for this work was inelastic neutron scattering which has the added benefit of providing information on the dispersion and the dynamics of the Haldane phase. However, in order to know the proper momentum transfer, $Q$, the reciprocal lattice vectors must be known

precisely. Therefore, neutron diffraction was used to measure the low temperature crystal structure, thus determining the reciprocal lattice vectors. In addition, the background and temperature dependence of the diffraction pattern provide a test of the deuteration and a check for structural transitions, respectively.

Since large single crystals are not available, Rietveld refinement on a powder sample was required. The sample was a 1 g conglomeration of microcrystalites, packed in a vanadium can in a He atmosphere to provide a means of thermal contact between the sample and the displex used to cool the sample. Data were acquired on the HB-4 powder diffractometer associated with the High Flux Isotope Reactor at Oak Ridge National Laboratory. Figure 7.14 shows the powder diffraction pattern and final refinement at 11 K for $MnCl_3$(d-bipy). The refined structure around a Mn site is shown in Figure 7.15, and the quality of the refinement is characterized by a reduced $\chi^2$ of 3.4. To arrive at the final result, successive refinements on groups of approximately ten parameters were performed. After each refinement step, the physical validity of the crystal structure near the Mn site was checked. During this process, there were several local minima in the least squares hyperspace, identified by a carbon or deuterium atom that was shifted unphysically. The procedure of letting the parameters of one of the C or N atoms and all of its nearest neighbors, except the deuterium atoms, vary, and subsequently varying each C with its corresponding deuterium atom, massaged the least squares hyperspace to avoid these local minima. This procedure greatly reduced the difference between the powder pattern and the calculated pattern at several of the Bragg peaks. Further refinement would require the next order

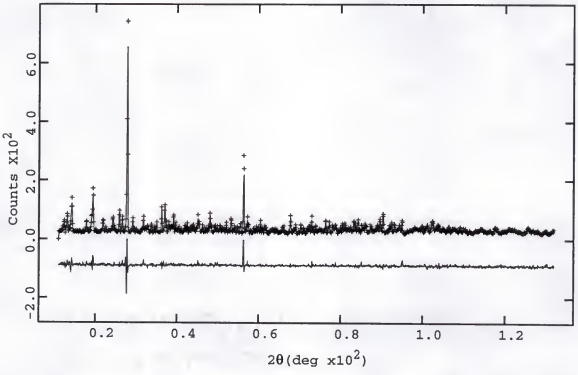


Figure 7.14: Powder diffraction pattern, Rietveld refinement, and difference plot for $MnCl_3$(d-bipy) at $T = 11$ K with neutrons of wavelength $\lambda = 1.4997$ Å.

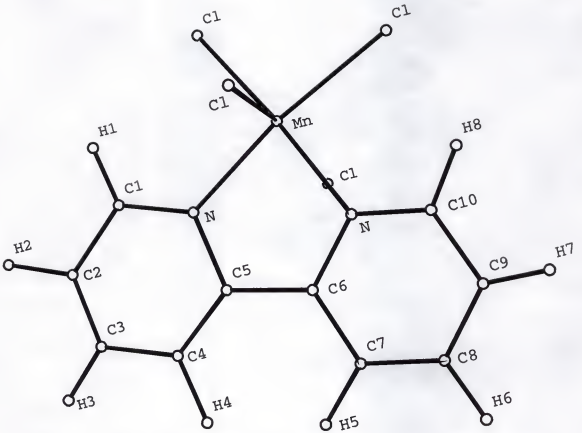


Figure 7.15: Crystal structure near a Mn atom in $MnCl_3$(d-bipy) at 11 K, determined by Rietveld refinement.

effect to appropriately tweak the deuterium atoms slightly out of the plane of the bipyridene group. Nevertheless, the present refinement is more than sufficient to determine the low temperature lattice parameters. The 11 K unit cell parameters are $a = 8.0872 \pm 0.0002$ Å, $b = 16.1394 \pm 0.0006$ Å, $c = 9.5517 \pm 0.00024$ Å, $\gamma = 109.469 \pm 0.002°$, and the distance between Mn sites is $4.80698 \pm 0.00008$ Å. A full presentation of the low temperature crystallographic data are given in Appendix B.

Besides the low temperature crystal structure, other useful information is provided by the neutron diffraction experiments. First, they demonstrate that the sample was fully deuterated. The negligible incoherent scattering background (low angles in Figure 7.14) qualitatively shows the absence of hydrogen in the system. Furthermore, initial refinements were performed with additional parameters to account for a small concentration of hydrogen in the system. As these refinements progressed, this concentration tended to zero within its uncertainty. Therefore, any hydrogen contribution was deemed negligible and excluded from further refinements. The uniformity of the powder was tested in a similar manner. The preferred orientation parameters were allowed to vary during early refinement steps. Successive refinements demonstrated that this effect is negligible. Therefore, it was excluded from the final refinement. Several quick scans (30 minutes in duration) were performed between 11 K and room temperature to examine the temperature dependence of the lattice parameters. These data provide another test for dimerization or other structural transitions which might open a gap in the magnetic excitation spectrum. Figures 7.16 - 7.20 show the

temperature dependence of the lattice parameters and the volume as a function of temperature. The absence of any discontinuities confirms that the chains do not dimerize or experience any other structural transitions.

## 7.4 Inelastic Neutron Scattering Measurements

With the Haldane gap macroscopically confirmed and the low temperature lattice constants determined, the next step is to perform the microscopic measurement of inelastic neutron scattering to directly measure the gap. Time of flight was the measurement technique chosen so that the signal to noise ratio could be increased by adding all detectors corresponding to $Q$ values near the antiferromagnetic point. This technique should provide a sufficient signal to observe the Haldane gap. Furthermore, comparison with scattering from detectors that correspond to $Q$ near zero can provide insight on the $Q$ dependence of the Haldane gap. Therefore, Figure 7.21 was calculated to provide guidance as to which detectors to sum. The detectors corresponding to angles between $23^o$ and $38^o$, represented by the area between the dashed and the solid lines in Figure 7.21, should provide the best resolution of the gap.

The instrument chosen was the time of flight spectrometer (TOF) on the cold source at the NIST reactor discussed in Section 4.4. The 3 mg sample consisted of three packets of powder wrapped in aluminum foil and mounted in an aluminum can flushed with He to remove any air and provide thermal contact to the cryostat. A hefty humdinger of a homemade $^3$He cryostat, appropriately named "Big Blue," was used to cool the sample to approximately 400 mK. To remove

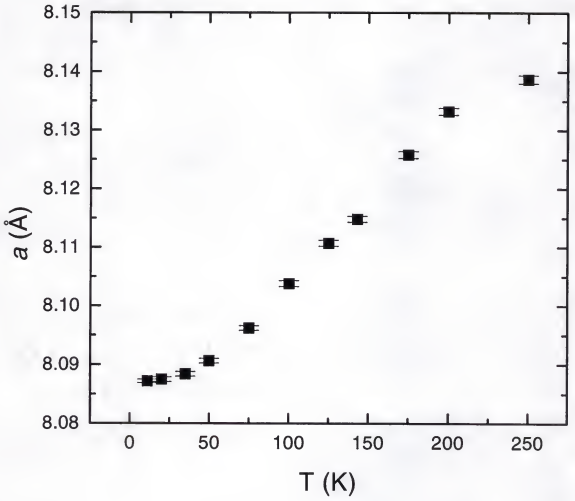


Figure 7.16: $a$ vs. $T$ for $MnCl_3$(d-bipy).

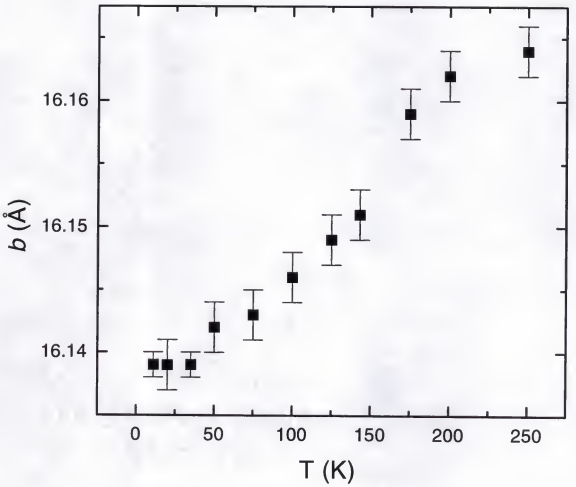


Figure 7.17: $b$ vs. $T$ for $MnCl_3$(d-bipy).

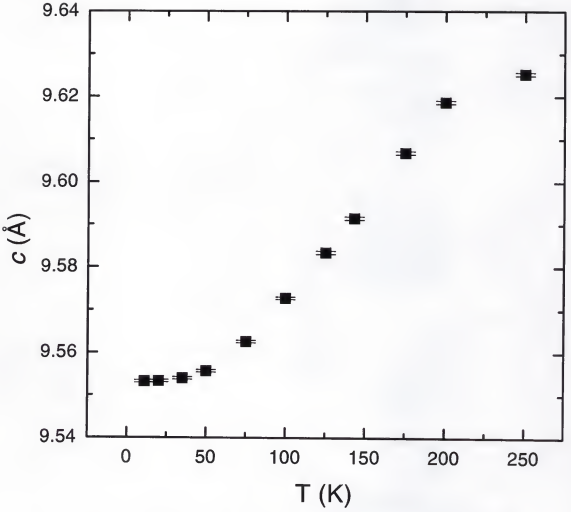


Figure 7.18: $c$ vs. $T$ for $MnCl_3$(d-bipy).

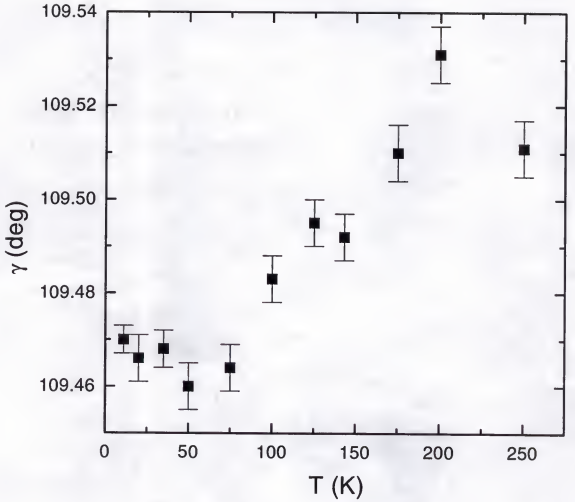


Figure 7.19: $\gamma$ vs. $T$ for $MnCl_3$(d-bipy).

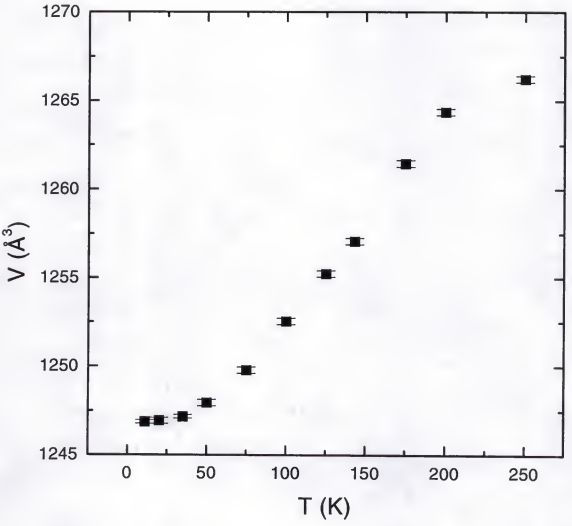


Figure 7.20: V vs. $T$ for $MnCl_3$(d-bipy).

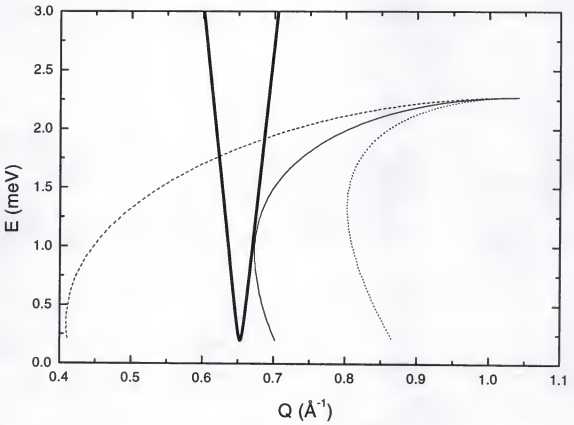


Figure 7.21: Estimated $S = 2$ dispersion for $MnCl_3$(bipy) and theoretical TOF spectrometer behavior. The heavy solid line represents the expected dispersion curve. The dashed line, thin solid line, and dotted line represent the $Q$-$E$ curves for angles of 23°, 40°, and 50°, respectively.

background scattering, Cd shielding was placed on the outside of the vacuum can in locations that should not have blocked any of the detectors. Data were collected on the sample for 40 hours at this temperature using neutrons with a wavelength of 6.0 Å. To be able to compare groups of detectors, the response of these groups had to be normalized against a standard. A good feature of the scattering function to compare for the normalization is the incoherent scattering peak. Consequently, vanadium is an appropriate normalization standard as it is nearly a pure incoherent scatterer. A setup for the normalization was made of a 1/4 inch diameter vanadium rod with precisely positioned Cd shields, placed in an aluminum vacuum can. Figure 7.22 reveals little difference in the incoherent peaks between the different groups of detectors for the vanadium standard. However, for the $MnCl_3$(d-bipy) sample, Figure 7.23 shows that the incoherent scattering peak is significantly smaller for the detectors spanning 23° to 38° when compared to other regions. To quantify the difference between the groups of detectors, the area under the inelastic scattering peak is shown in Table 7.1 for both the vanadium standard and the $MnCl_3$(d-bipy) sample. Furthermore, the ratio between the sample and the standard is also given. For a proper normalization,

| Detector Grouping | V | $MnCl_3$(d-bipy) | $MnCl_3$(d-bipy)/V |
|---|---|---|---|
| $118 - 135^o$ | 0.336 | 0.632 | 1.88 |
| $40 - 50^o$ | 0.325 | 0.440 | 1.35 |
| $23 - 38^o$ | 0.258 | 0.179 | 0.694 |

Table 7.1: Normalization constants for three groups of detectors. Notice only the $23 - 38^o$ range is less than one, indicating problems with the measurement as discussed in the text.

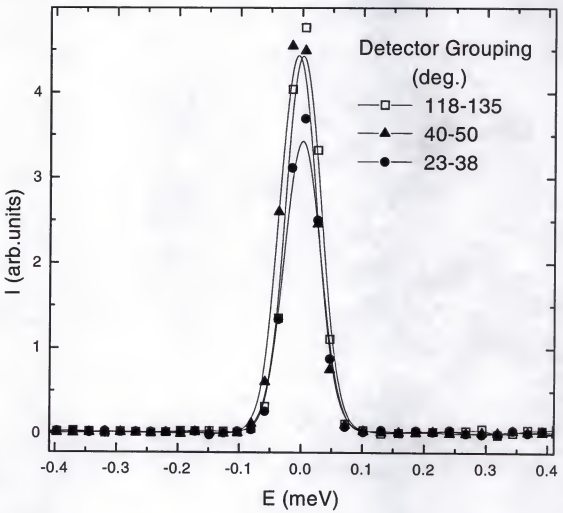


Figure 7.22: Incoherent scattering from a vanadium standard for several groups of detectors on the NIST TOF Spectrometer. The lines are guides for the eye.

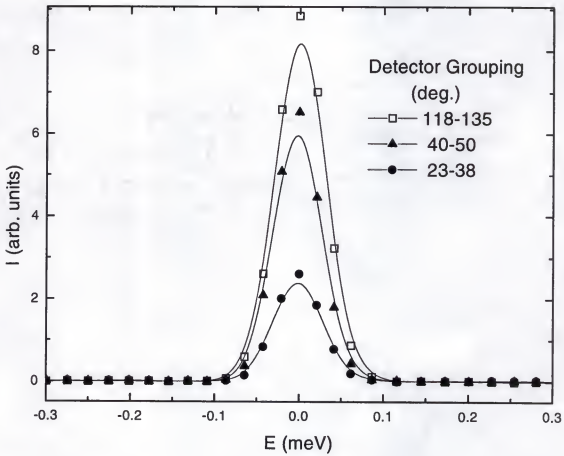


Figure 7.23: Incoherent scattering from the $MnCl_3$(d-bipy) sample for several groups of detectors on the NIST TOF spectrometer. The lines are guides for the eye.

the ratios should be consistently greater or less than one. The $23-38^o$ detectors for the $MnCl_3$(d-bipy) are inconsistent with the other detectors. Therefore, these detectors were probably shadowed by the cadmium shielding. Nevertheless, the range of detectors that covers the angles of $40^o$ to $50^o$ degrees provides hints of the Haldane gap. These detectors are not physically excluded from observing some contribution from the gap since the powder sample provides a spherical average of resultant $Q$ values, which smears the boundary regions of Figure 7.21. For comparison, $Q$ values distant to the antiferromagnetic point, measured by detectors which represent angles of $118^o$ to $135^o$, were checked as well. Figures 7.24 and 7.25 show the scattering intensity for $Q$ values near and distant to the antiferromagnetic point, respectively. Figure 7.24 shows a feature at $\sim 0.3$ meV which is consistent in energy with the Haldane gap. To test this peak for statistical significance, a sum of two Gaussian functions, one function for the inelastic contribution and the other for this subtle feature, was fit to the data as represented by the heavy curve in Figure 7.24. The uncertainty in the curve is represented by the lighter lines above and below the heavy line. Figure 7.25 does not show any increased scattering at $\sim 0.3$ meV which is consistent with the $Q$ dependence of the Haldane gap discussed in Section 2.3. Finally, data were collected at $T = 10$ K in order to confirm that the $\sim 0.3$ meV feature disappears at temperatures well above the Haldane gap. Figure 7.26 shows no statistically significant features consistent with the Haldane gap. To quantify the statistical significance of the 0.3 meV feature, an F-test was performed comparing the variance of a fit with two Gaussian peaks to a fit with one Gaussian peak for

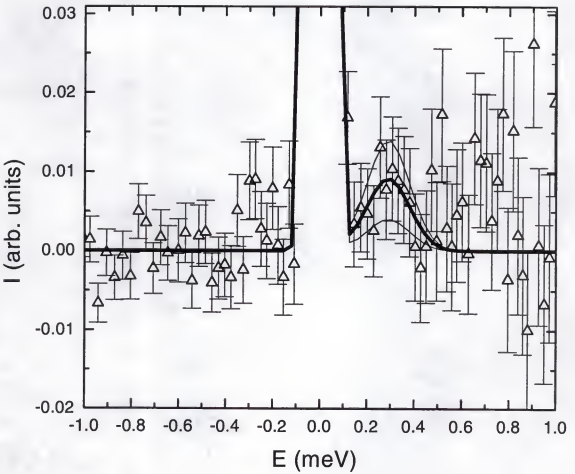


Figure 7.24: Inelastic neutron scattering intensity at $T = 0.4$ K and $Q \approx \pi$ from $MnCl_3$(d-bipy). The heavy line shows a best fit to two Gaussians suggesting magnetic scattering consistent with the Haldane gap. The thin lines show the uncertainty in the fit. Further discussion of the statistical significance of the 0.3 meV peak is given in the text.

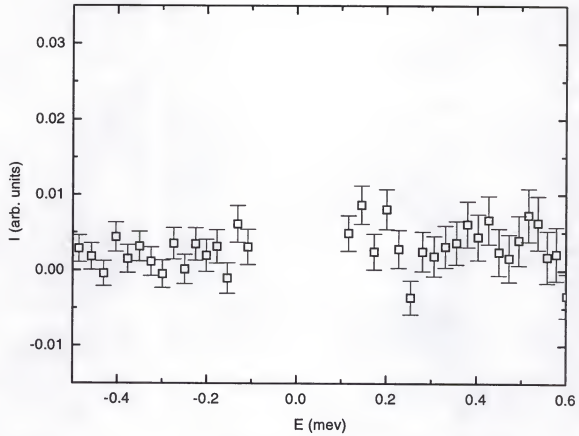


Figure 7.25: Inelastic neutron scattering intensity at $T = 0.4$ K and $Q \ll \pi$ from $MnCl_3$(d-bipy).

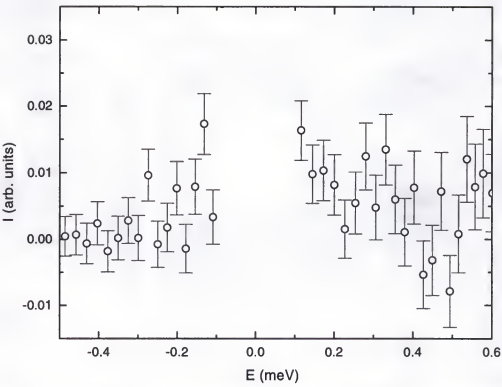


Figure 7.26: Inelastic neutron scattering intensity near $Q = \pi$ at $T = 10$ K from $MnCl_3$(d-bipy).

0.4 K data. Attempts were also made for the 10 K data, but the non-linear least squares fitting routine would not converge with a finite second peak. Unfortunately, the noise in the measurement is too strong to provide an excellent test, as is demonstrated by the fact that $F$ is close to one. For the 0.4 K data, $F = 1.05$ which means the 0.3 meV feature exists above the noise with a 65% confidence level. Clearly, this analysis indicates that better signal to noise is needed to confirm the Haldane gap, but there is a hint that the feature exists. In summary, the inelastic neutron scattering data for $Q$ values near the antiferromagnetic point reveal a subtle shoulder that is consistent with the microscopic presence of the

Haldane gap. Furthermore, comparisons between the scattering intensity in the region of $\sim$ 0.3 meV, for $Q$ values near to and far from the antiferromagnetic point, and for temperatures well below and well above the gap reveal behavior consistent with a Haldane gap. Nevertheless, the signal to noise is not sufficient to model the magnetic scattering according to theoretical models for $S(Q,\omega)$ and, therefore, further work remains in progress.

# CHAPTER 8
# CONCLUSIONS

The experimental work in this thesis has covered unique aspects of three integer spin antiferromagnetic chains. Chapters 5, 6, and 7 described the results on TMNIN, NINAZ, and $MnCl_3$(bipy) respectively. This chapter will review the major results for each material and provide suggestions for future scientific studies.

## 8.1 TMNIN

Measurements of the magnetization as a function of magnetic field on the $S = 1$ antiferromagnetic chain TMNIN revealed critical fields (see Figures 5.3 – 5.7) corresponding to $\Delta = 3.5 \pm 2$ K and $D/J = 0.06 \pm 0.03$, where $J = 10.11 \pm 0.05$ K. Therefore, this material not only exhibits a Haldane gap, but also is very close to a pure Heisenberg model. However, high field ESR spectra [154, 155] possess features that have been associated with $D/J \approx 0.5$. Section 5.3 described the comparisons between the results from magnetization and the ESR studies and introduced a possible solution to the discrepancy, namely the presence of two slightly different magnetic sites, similar to the case of NENP [98]. Although the results from several experiments are consistent with the proposed picture, an experiment is needed to unambiguously confirm it.

Investigations on the NMR line shape at $T < \Delta$ may resolve this issue by providing the information about the local magnetic environment.

## 8.2 NINAZ

The $S = 1$ material NINAZ has been an excellent model system to test end-chain spin effects for several reasons. Firstly, $J \approx 125$ K is sufficiently large so fully developed quantum properties can be tested at $T = 4$ K. Secondly, the material has a structural transition which naturally causes chain breaks. Thirdly, our experimental tests demonstrated that more chain breaks can be introduced by pulverizing the material. Magnetization measured as a function of magnetic field (see Figure 6.11) not only provided macroscopic evidence of this increase, but also demonstrated that the end-chain spins are $S = 1/2$.

Electron spin resonance investigations provided additional information on the system. Firstly, the existence of the X-band ESR signal is another demonstration that the end-chain spins are $S = 1/2$. Secondly, the temperature dependence of the ESR intensity (see Figure 6.28) was fit to the expressions of Mitra, Halperin, and Affleck [57], providing a microscopic measurement of the chain length. Comparisons of this measurement to the macroscopic particle size distributions in Figures 6.4 and 6.5 show that the characteristic particle size for the ultrafine powder and the powder are smaller and larger than the characteristic polycrystalline chain length, respectively. Finally, the line width of the powder and ultrafine powder samples shows the first evidence of an interaction of the magnetic excitations on the chain with the end-chains spins. Furthermore, by

comparison with the theory of Mitra, Halperin, and Affleck explained in Section 2.4.1, the interaction does not cause the magnetic excitations to change energy levels.

Another method used to study the end-chain spins in NINAZ was to compare the response of pure and doped samples. Magnetization as a function of magnetic field (see Figure 6.13) for samples doped with 0.5% of Cd, Hg, and Zn suggests as much as 1/3 of the sample consists of paramagnetic $S = 1/2$ spins. On the other hand, ESR resonance studies observed quantities of spins four orders of magnitude smaller. This result suggests that the majority of the end-chain spin spectral weight has been shifted to fields inaccessible by the X-band spectrometer. To confirm this assumption, high field ESR measurements should be performed on the doped samples. However, since the doping has caused such a large increase in the number of paramagnetic spins observed in the system, the consistency of the crystal structure with the structure of the pure samples is questionable. Therefore, before any other experiments are attempted on the doped samples, careful X-ray studies should be performed to ensure that the system is still NINAZ.

## 8.3 $MnCl_3$(bipy)

The first identification of an $S = 2$ Haldane gap was provided by our magnetization measurements at $T = 30$ mK in $MnCl_3$(bipy). Studies with the magnetic field applied both parallel and perpendicular to the chains exhibited critical fields that provide $\Delta = 2.3 \pm 0.8$ K and $D/J = 0.010 \pm 0.003$, where $J = 34.8 \pm 1.6$ K.

This assignment resulted from a careful elimination of other possible sources (*e.g.*, spin flops, dimerizations, large $D$ transitions) of critical fields. Preliminary attempts to find the Haldane gap using inelastic neutron scattering (see Figure 7.24) provide hints of magnetic scattering at an energy consistent with the magnetization analysis, but further measurements are needed to confirm its existence. Besides additional inelastic neutron scattering studies, other microscopic measurements can provide useful information. High field ESR at temperatures below the gap can map out the energy vs. magnetic field diagram similar to the study performed in NENP [19, 99, 100, 107]. Finally, NMR can provide another identification of the gap by a measurement of $T_1$ vs. $T$, and the line shape would check for a staggered magnetization similar to NENP [98].

# APPENDIX A
## High Temperature Expansions

This appendix contains the high temperature series expansions of Jolicœur [51] performed on the $S = 1$ linear antiferromagnetic chain described by the Hamiltonian

$$\mathcal{H} = J \sum S_i \cdot S_{i+1} + D(S_z)^2. \tag{A.1}$$

When a Padé approximate method is used to evaluate the series, the fit is reliable down to $T/J = 0.2$. In this thesis, Maple V (release 4) was used for the fits as it has a robust Padé approximate routine and numerical precision can be kept to as large as necessary, which is crucial in intermediate steps.

### A.1 Specific Heat

The series for the specific heat is

$$C(T) = \sum a_n/(3^n n!)(1/T)^n \tag{A.2}$$

where the term $a_n$ is a polynomial in $D$, and $T$ is measured in units of $J$. The coefficients $a_n$ are:

1/T-order : 0

D-order :

0 0.00000000000000000000000000000000000

1/T-order : 1

D-order :

0 0.00000000000000000000000000000000000

1 0.00000000000000000000000000000000000

1/T-order : 2

D-order :

0 24.0000000000000000000000000000000000

1 0.00000000000000000000000000000000000

2 4.0000000000000000000000000000000000

1/T-order : 3

D-order :

0 108.000000000000000000000000000000000

1 0.00000000000000000000000000000000000

2 0.00000000000000000000000000000000000

3 12.0000000000000000000000000000000000

1/T-order : 4

D-order :

0 -4320.00000000000000000000000000000000

1 0.00000000000000000000000000000000000

2 -864.00000000000000000000000000000000

3 0.00000000000000000000000000000000000

4 -72.00000000000000000000000000000000

1/T-order : 5

D-order :

0 -48600.00000000000000000000000000000

1 -0.6864997625308918523177755644448520 6E-30

2 -7199.99999999999999999999999999990

3 -7200.00000000000000000000000000003

4 0.00000000000000000000000000000000000

5 -600.00000000000000000000000000000000

1/T-order : 6

D-order :

0 1496880.00000000000000000000000000

1 0.2920971351924722629413480981547887 5E-28

2 534599.99999999999999999999999995

3 -25919.99999999999999999999999999974

4 29159.99999999999999999999999999996

5 0.00000000000000000000000000000000000

6 1260.00000000000000000000000000000000

1/T-order : 7

D-order :

0 32720436.00000000000000000000000000

1 0.3267443028263339867010614767418595 8E-25

2 7810991.99999999999999999999999345

3 4413528.00000000000000000000000430

4 571535.99999999999999999999998882

5 920808.00000000000000000000000098

6 0.00000000000000000000000000000000000

7 37044.00000000000000000000000000000

1/T-order : 8

D-order :

0 -845474112.00000000000000000000000000

1 -0.64116053038295958919011396159358090E-22

2 -459188351.99999999999999999999985512

3 51383807.99999999999999999999882993

4 -57516479.99999999999999999999956877

5 5322239.99999999999999999999926599

6 2346624.00000000000000000000000004640

7 0.00000000000000000000000000000000000000

8 53424.00000000000000000000000000000000

1/T-order : 9

D-order :

0 -32830719120.00000000000000000000000000

1 -0.3881908875989551951736847737538248OE-19

2 -11557017791.99999999999999999903733

3 -4241030400.00000000000000000000899849

4 -1171532159.99999999999999999999586511

5 -1276928064.00000000000000000000099514

6 -47589119.99999999999999999998804783

7 -110014848.00000000000000000000005612

8 0.00000000000000000000000000000000000000

9 -2870640.00000000000000000000000000000000

1/T-order : 10

D-order :

0 675493966080.00000000000000000000000000

1 0.11137744414028595129240481140894957E-17

2 529920160199.99999999999999999714654

3 -94583375999.99999999999999999997182494

4 107062397999.999999999999999999858224

5 -20270865599.999999999999999999602390

6 929912399.999999999999999999993734908

7 -1028764799.999999999999999999948383

8 -1088688600.000000000000000000001721

9 0.000000000000000000000000000000000000

10 -18356220.000000000000000000000000000

1/T-order : 11

D-order :

0 46217135541060.00000000000000000000

1 0.749472423567987463587862746400361 87E-17

2 22067612479440.00000000000000000071546

3 5621958274679.99999999999999997933416

4 3317138256960.00000000000000002036914

5 2471736144239.99999999999999999015087

6 121897781280.00000000000000002589146

7 297137309039.99999999999999999625685

8 2359296720.00000000000000000002773223

9 12122268839.99999999999999999991853

10 0.000000000000000000000000000000000000

11 253061820.00000000000000000000000000

1/T-order : 12

D-order :

0 -658155004927200.00000000000000000000

1 0.986561405270471025413907139386542 08E-13

2 -774510315147360.00000000000016634030

3 212199802379136.00000000000001550494

4 -228063139449551.99999999999987449320

5 66863279070719.99999999999893112749

6 -11844806136767.99999999999958526408

7 6531390049535.99999999999910549341

8 2583589005360.00000000000000011015880

9 212671578239.99999999999999992759574

10 305088179616.00000000000000000196849

11 0.00000000000000000000000000000000000000

12 3917484648.000000000000000000000000

1/T-order : 13

D-order :

0 -86589623748617496.000000000000000000

1 0.16691726314776550857258894622257804E-12

2 -52949249647695648.000000000000158118

3 -9537683865454368.00000000000002814010

4 -10939408222245983.99999999999497409

5 -5811190813634544.0000000000003157060

6 -654690366315647.99999999999989743152

7 -1057737434869440.000000000000186113

8 20932078561056.00000000000001845458

9 -57774974907312.00000000000000087719

10 833185694016.000000000000000000128083

11 -500353757279.999999999999999999873

12 0.00000000000000000000000000000000000000

13 -18869465160.000000000000000000000000

1/T-order : 14

D-order :

0 562412828945822400.00000000000000000

1 0.11850215357582634283041556985597184E-09

2 132806212481717495.9999999998948148

3 -585447359184507456.00000000012492762

4 56121944121465112 8.00000000013708412

5 -250575681395134368.00000000000284687

6 5532960029108 1479.999999999967202634

7 -35218565624092031.999999999989725929

8 -7212097967275655.999999999994161914

9 -1975748425743456.000000000008442731

10 -1418333640318503.999999999998279087

11 -46744454877120.000000000000014911379

12 -81469060447319.999999999999999513042

13 0.00000000000000000000000000000000000000

14 -847702120356.000000000000000000000000

1/T-order : 15

D-order :

0 2070948628571120209 80.00000000000273

1 0.9516409003446240244814189071672 4089E-10

2 1562342215268487743 99.99999999997272

3 1929220383399652979 9.999999999853117

4 4178893539479064840 0.000000000050022

5 1609813768763699100 0.000000000055252

6 3752774819450873999.9999999999737099

7 4104853966504279799.9999999999967599

8 -87072381012355199.999999999996527829

9 375185375401699799.99999999999958078

10 -26373476928632400.000000000000108126

11 4519518512833800.000000000000354381

12 -563922660798000.0000000000000365076

13 -511631087952599.99999999999999987120

14 0.00000000000000000000000000000000000000

15 -1482426909180.000000000000000000000000

1/T-order : 16

D-order :

0 6308796255050131603l9.99999999999272

1 -0.937500065312111467965751786252735O1

2 -230785887087301006079 8.2812499681022

3 19579647408178631270 39.0625000901055

4 -154425074459200875647 9.8437500460423

5 10767452960174269132 79.9999999732536

6 -241172007857181043199.99999998394560

7 20657535116444513280 0.00000000189038

8 21621413448277799039.999999998013209

9 16214802798054850560.000000000087224

10 79658805264868684 80.0000000000939053

11 531042160467363839.99999999998826682

12 59862907052330111 9.99999999999867962

13 10068606925977600.000000000000304258

14 21357039422937599.999999999999985771

15 0.0000000000000000000000000000000000000

16 193916304689760.00000000000000000000

1/T-order : 17

D-order :

0 -611391451107142135739232.00000000000

1 170.836474100362691594244028838873882

2 -555542879294109646242852.66717503592

3 -420551729212932772319 34.789663109928

4 -184863257614180875124501.09291181341

5 -505984641623706597280 47.265661587939

6 -228215317625706169681 86.157444739481

7 -175537775225645562516 60.565531834902

8 165379151591294909188.16183909051142

9 -233252559667910281996 8.4650002297203

10 2386609139313734215 68.00570257517029

11 -885786171357449272 32.000618769507128

12 16895283750395352575.999990645846879

13 5185291917152994048.0000007161134761

14 271564358604788735.99999999412750999

15 363794918632487424.00000000039150466

16 0.00000000000000000000000000000000000000

17 1813660872084000.0000000000000000000

1/T-order : 18

D-order :

0 -914988693500131838633697 6.0000000000

1 -104183.492397892212260124036035624 91

2 188847851124002592387811 7.7024842501

3 -780430606866500344510812 0.3967514634

4 437271153386957938536095 4.0441572070

5 -530792493534835963631043 9.6859882474

6 106836482715350610153096 9.6268084273

7 -131605949824185319836469 9.7804109380

8 -631873140702057895378 70.847942554741

9 -142812438689065747385703.50490794890

10 -482353804378887630740 55.549985578749

11 -620549271525956217523 2.1392495080363

12 -549012381180497228879 9.9755676076747

13 -75074387239658325888.000281999632080

14 -215513382145316093279.99996624477535

15 -149375932880744678 3.9999997223833116

16 -486057692325964456 8.0000000284355224

18 -44540376825659148.000000000000000000

1/T-order : 19

D-order :

0 216514275512499293894375957 9.9999847

1 6362561.475085082803100133830298 5459

2 233560905275031840988835521 8.5256958

3 738005660917172309836521 63.613878727

4 941658115694904121375956367.19382477

5 169665476584916097821667095.13447475

6 151009040284465617563306225.24403191

7 815766941618981146610181 05.546412468

8 176715904201575598916094 8.0691311806

9 149671387015653607444659 94.661488563

10 -210906191656753417670548 0.4004050270

11 955467798876662717763012.37924189866

12 -224598125967406702392959.75556565262

13 -227627955629449131677 75.685135310283

15 -535849523592172960694 4.0004995671043

16 -124543401156142067376.00000001676744

17 -198012090204084168215.99999985099930

18 0.00000000000000000000000000000000000000

19 -966836320351010676.00000000000000000

1/T-order : 20

D-order :

0 65414053028901744339879146780.000000

1 -1645730233.92246034638361606994294 56

2 22857867846598172311640275903.581543

3 36462803689119376954310641857.098145

4 -95198719255351621427412973 31.4746704

5 29885521010887589936726636581.248779

6 -46690903319798631691306484 99.1762085

7 92092186949143959927562823 45.0463257

8 15041440348942863101384864 6.57219696

9 13069436274026571463433791 44.3957672

10 30881989135975758875753021 6.55378151

11 81270845855369479465627474.792070389

12 51210550941140087678555938.085169315

13 10538156980441801739519 83.3968225271

14 31233423861154562297760 05.8624264002

15 -64307863926090595584 00.056661920622

17 -47268919418418532 8000.00004387601803

18 27928095074290953360 0.00001169103780

19 0.00000000000000000000000000000000000000

## A.2 Perpendicular Magnetic Susceptibility

For the magnetic susceptibility with the magnetic field oriented perpendicular to the chain the series is

$$3T\chi_x = \sum a_n/(3^n n!)(1/T)^n. \tag{A.3}$$

The coefficients $a_n$ are polynomials in $D$ whose coefficients are:

1/T-order : 0

D-order :

0 2.00000000000000000000000000000000000

1/T-order : 1

D-order :

0 -8.00000000000000000000000000000000000

1 4.00000000000000000000000000000000000

1/T-order : 2

D-order :

0 20.00000000000000000000000000000000000

1 -16.00000000000000000000000000000000000

2 4.00000000000000000000000000000000000

1/T-order : 3

D-order :

0 96.0000000000000000000000000000000000

1 72.0000000000000000000000000000000000

2 36.0000000000000000000000000000000000

3 -12.000000000000000000000000000000000000

1/T-order : 4

D-order :

0 -780.000000000000000000000000000000000

1 -456.000000000000000000000000000000000

2 -576.000000000000000000000000000000000

3 336.00000000000000000000000000000000

4 -60.000000000000000000000000000000000

1/T-order : 5

D-order :

0 -14688.00000000000000000000000000000000

1 3240.0000000000000000000000000000000

2 -7800.000000000000000000000000000000000

3 -4656.000000000000000000000000000000000

4 -84.000000000000000000000000000000000000

5 84.000000000000000000000000000000000000

1/T-order : 6

D-order :

0 101916.00000000000000000000000000000000

1 76176.00000000000000000000000000000000

2 153216.00000000000000000000000000000000

3 -3600.00000000000000000000000000000000

4 16200.00000000000000000000000000000000

5 -12312.00000000000000000000000000000000

6 1764.00000000000000000000000000000000

1/T-order : 7

D-order :

0 5446440.00000000000000000000000000000000

1 -1868471.99999999999999999999999999999952

2 3465827.99999999999999999999999999999879

3 458064.00000000000000000000000000000969

4 568331.99999999999999999999999999999657

5 373248.00000000000000000000000000000056

6 -35676.00000000000000000000000000000032

7 1908.00000000000000000000000000000000

1/T-order : 8

D-order :

0 -16226028.00000000000000000000000000

1 -38953224.00000000000000000000001137

2 -65471183.99999999999999999999997699

3 7226495.99999999999999999999984490

4 -17502047.99999999999999999999999612

6 180287.99999999999999999999998829

7 635616.00000000000000000000000121

8 -79740.00000000000000000000000000

1/T-order : 9

D-order :

0 -3552744239.99999999999999999999992

1 1281675960.00000000000000000000281

2 -2755937520.00000000000000000000546

3 16722288.00000000000000000000031019

4 -639975816.00000000000000000000000414

5 -194293728.00000000000000000000000134

6 -37250927.99999999999999999999999612

7 -36477216.00000000000000000000000026

8 5331420.00000000000000000000000000

9 -407916.00000000000000000000000000

1/T-order : 10

D-order :

0 -11465749259.999999999999999999999974

1 36909350352.000000000000000000193150

2 38433358223.999999999999999999473834

3 -5069386943.9999999999999999994314953

4 20139342335.999999999999999999675626

5 -6320484431.9999999999999999998917460

6 1370061215.999999999999999999781690

7 -682336223.9999999999999999999738508

8 -199814040.000000000000000000017099

9 -36923687.999999999999999999995308

10 4601124.00000000000000000000000000

1/T-order : 11

D-order :

0 3508721851967.999999999999999999966

1 -1203821801711.99999999999999990378

2 3322825109819.99999999999999973001

3 -323755669007.999999999999999688885

4 975639189383.99999999999999800439

5 192893691600.00000000000000080320

6 97329853367.999999999999999999787659

7 48663506592.000000000000000000036806

8 175612211.999999999999999999598983

9 4033653552.000000000000000000002482

10 -787587948.000000000000000000000662

11 59355828.000000000000000000000000

1/T-order : 12

D-order :

0 42078240698508.000000000000000000027

1 -52611861285432.000000000000004787620

2 -21973888468079.999999999999985734014

3 3290087461967.999999999999825139738

4 -26377344970847.999999999999988193235

5 10835510605631.99999999999995083119

6 -4540663595087.999999999999986703175

7 2381295995999.999999999999997621968

8 146680223760.000000000000000002788602

9 116123545295.999999999999999794224

10 55352491776.000000000000000000086417

11 876537935.999999999999999999843073

12 -241916220.000000000000000000000000

## A.3 Parallel Magnetic Susceptibility

For the magnetic susceptibility with the magnetic field oriented parallel to the chain the series is

$$3T\chi_z = \sum a_n/(3^n n!)(1/T)^n. \tag{A.4}$$

The coefficients $a_n$ are polynomials in $D$ whose coefficients are:

1/T-order : 0

D-order :

0 2.00000000000000000000000000000000000

1/T-order : 1

D-order :

0 -8.00000000000000000000000000000000000

1 -2.00000000000000000000000000000000000

1/T-order : 2

D-order :

0 20.00000000000000000000000000000000000

1 32.00000000000000000000000000000000000

2 -2.00000000000000000000000000000000000

1/T-order : 3

D-order :

0 96.00000000000000000000000000000000

1 -252.000000000000000000000000000000000

2 0.00000000000000000000000000000000000

3 6.00000000000000000000000000000000000

1/T-order : 4

D-order :

0 -780.0000000000000000000000000000000000

1 480.000000000000000000000000000000000

2 936.000000000000000000000000000000000

3 -384.0000000000000000000000000000000000

4 30.00000000000000000000000000000000000

1/T-order : 5

D-order :

0 -14688.000000000000000000000000000000000

1 11340.00000000000000000000000000000000

2 -21840.000000000000000000000000000000000

3 6360.00000000000000000000000000000000

4 -480.000000000000000000000000000000000

5 -42.0000000000000000000000000000000000

1/T-order : 6

D-order :

0 101916.00000000000000000000000000000000

1 7056.00000000000000000000000000000000

2 115092.00000000000000000000000000000000

3 36576.00000000000000000000000000000000

4 -41148.00000000000000000000000000000000

5 12096.00000000000000000000000000000000

6 -882.00000000000000000000000000000000

1/T-order : 7

D-order :

0 5446440.00000000000000000000000000000000

1 -2412899.99999999999999999999999999742

2 4474007.99999999999999999999999999418

3 -3146219.99999999999999999999999999540

4 2022551.99999999999999999999999999834

5 -460403.99999999999999999999999999717

6 50399.99999999999999999999999999823

7 -954.00000000000000000000000000000000

1/T-order : 8

D-order :

0 -16226028.00000000000000000000000000

1 -29102976.00000000000000000000000517

2 -37156175.99999999999999999999998733

3 22410431.99999999999999999999998798

4 -15662807.99999999999999999999999447

5 -1005120.00000000000000000000000012602

6 2198160.00000000000000000000000137

8 39870.00000000000000000000000000000

1/T-order : 9

D-order :

0 -3552744240.00000000000000000000000000

1 969449148.00000000000000000000000662

2 -2712940128.00000000000000000000000265

3 1198075536.00000000000000000000000352

4 -1227855024.00000000000000000000000215

5 580839336.00000000000000000000000651

6 -259928352.00000000000000000000000098

7 51247728.00000000000000000000000058

8 -5824224.00000000000000000000000000000

9 203958.00000000000000000000000000000

1/T-order : 10

D-order :

0 -11465749260.00000000000000000000000026

1 35607476879.99999999999999999790042

2 12536744220.00000000000000000574712

3 -11133858240.00000000000000000624779

4 20183570280.00000000000000000358910

5 -11997302688.00000000000000000120557

6 4642709400.00000000000000000244300

7 -709871040.00000000000000000293173

8 -71320499.99999999999999999808650

9 33773759.99999999999999999994778

10 -2300562.00000000000000000000000000

1/T-order : 11

D-order :

0 3508721851968.00000000000000000000

1 -526107590315.99999999999999997153630

2 2882974449959.99999999999999185781

3 -900694903283.99999999999999590588151

4 1178670084767.9999999999999999413815

5 -428431112999.99999999999999997813289

6 303064868303.999999999999999991230

7 -113849549351.999999999999999926110

8 41197238279.999999999999999935539

9 -7332876539.999999999999999969518

10 804751199.999999999999999994106

11 -29677914.000000000000000000000000

1/T-order : 12

D-order :

0 42078240698508.000000000000000000054

1 -51430862185631.999999999999995972406

2 9291597603767.999999999999880875997

3 1894921581600.000000000000144841143

4 -18829421828604.000000000000009711294

5 17630500756608.000000000000004025961

6 -11126075134032.000000000000001087792

7 5488114253760.000000000000001952284

8 -1647970515324.000000000000000230867

9 326382740064.000000000000000172742

10 -22864758408.000000000000000074023

11 -766184831.999999999999999999861819

12 120958110.000000000000000000000000

APPENDIX B

Low Temperature Crystallographic data for $MnCl_3$(d-bipy)

| Unit Cell Parameters | |
|---|---|
| Space group | Cc |
| $T$(K) | 11 |
| $a$(Å) | 8.0872(2) |
| $b$(Å) | 16.1394(6) |
| $c$(Å) | 9.5517(2) |
| $\alpha$(deg) | 90 |
| $\beta$(deg) | 90 |
| $\gamma$(deg) | 109.469(2) |

| Atomic positions | | | |
|---|---|---|---|
| atom | X | Y | Z |
| Mn | 0.7725 | 0.0169 | 0.7158 |
| Cl | 0.7750 | 0.0605 | 0.9760 |
| Cl | 0.6236 | 0.1237 | 0.5989 |
| Cl | 1.0374 | 0.0774 | 0.7437 |
| N | 0.5597 | -0.0519 | 0.7055 |
| C1 | 0.3990 | -0.0261 | 0.6549 |
| C2 | 0.2596 | -0.0840 | 0.6217 |
| C3 | 0.2900 | -0.1628 | 0.6490 |
| C4 | 0.4560 | -0.1892 | 0.7034 |
| C5 | 0.5927 | -0.1359 | 0.7267 |
| C6 | 0.7781 | -0.1554 | 0.7885 |
| C7 | 0.8449 | -0.2365 | 0.8289 |
| C8 | 1.0216 | -0.2500 | 0.8960 |
| C9 | 1.1359 | -0.1856 | 0.9206 |
| C10 | 1.0661 | -0.1054 | 0.8823 |
| N | 0.8978 | -0.0916 | 0.8186 |
| H1 | 0.3748 | 0.0375 | 0.6473 |
| H2 | 0.1185 | -0.0578 | 0.5794 |
| H3 | 0.1854 | -0.2091 | 0.6185 |
| H4 | 0.4864 | -0.2610 | 0.7213 |
| H5 | 0.7411 | -0.2876 | 0.8034 |
| H6 | 1.0761 | -0.3139 | 0.9180 |
| H7 | 1.2764 | -0.1863 | 0.9738 |
| H8 | 1.1489 | -0.0499 | 0.9019 |

Bond Lengths

| Bond | Length(Å) |
|---|---|
| Mn-Mn | 4.80698(8) |
| Mn-Cl | 2.57743(4) |
| Mn-Cl | 2.61529(4) |
| Mn-Cl | 2.18371(5) |
| Mn-Cl | 2.28781(5) |
| Mn-N | 2.02353(4) |
| Cl-Mn | 2.18371(5) |
| N-C1 | 1.29436(3) |
| N-C5 | 1.38428(5) |
| C1-C2 | 1.41633(3) |
| C1-H1 | 1.04402(3) |
| C2-C3 | 1.30515(4) |
| C2-H2 | 1.15669(3) |
| C3-C4 | 1.33747(3) |
| C3-H3 | 1.09282(2) |
| C4-C5 | 1.35881(3) |
| C4-H4 | 1.18513(4) |
| C5-C6 | 1.45094(4) |
| C6-C7 | 1.42001(4) |

| Bond | Length(Å) |
|---|---|
| C7-C8 | 1.37524(4) |
| C7-H5 | 1.14319(2) |
| C8-C9 | 1.35908(3) |
| C8-H6 | 1.11209(3) |
| C9-C10 | 1.41103(4) |
| C9-H7 | 1.07881(3) |
| C10-H8 | 1.09629(3) |
| N-C6 | 1.37622(3) |
| N-C10 | 1.31114(3) |

Bond Angles

| Bond | Angle (deg.) |
|---|---|
| Cl-Mn-Cl | 167.270(0) |
| Cl-Mn-Cl | 95.925(2) |
| Cl-Mn-Cl | 93.688(2) |
| Cl-Mn-N | 85.987(2) |
| Cl-Mn-N | 85.950(1) |
| Cl-Mn-Cl | 93.331(2) |
| Cl-Mn-N | 95.352(2) |
| Cl-Mn-N | 175.325(0) |
| Cl-Mn-N | 171.299(0) |
| Cl-Mn-N | 90.816(2) |
| N-Mn-N | 80.485(2) |
| Mn-Cl-Mn | 135.551(1) |
| N-C1-C2 | 119.789(2) |
| N-C1-H1 | 118.964(0) |
| C2-C1-H1 | 121.073(2) |
| C1-C2-C3 | 120.983(2) |
| C1-C2-H2 | 117.105(2) |
| C3-C2-H2 | 121.696(0) |
| C2-C3-C4 | 119.081(0) |
| C2-C3-H3 | 122.350(2) |
| C4-C3-H3 | 118.259(2) |
| C3-C4-C5 | 121.238(2) |
| C3-C4-H4 | 120.017(0) |
| C5-C4-H4 | 118.488(2) |

| Bond | Angle (deg.) |
|---|---|
| N-C5-C4 | 119.272(2) |
| N-C5-C6 | 113.193(0) |
| C4-C5-C6 | 127.187(2) |
| C5-C6-C7 | 123.843(0) |
| C5-C6-N | 118.893(2) |
| C7-C6-N | 117.149(2) |
| C6-C7-C8 | 120.999(1) |
| C6-C7-H5 | 114.957(2) |
| C8-C7-H5 | 124.034(2) |
| C7-C8-C9 | 120.011(2) |
| C7-C8-H6 | 121.336(0) |
| C9-C8-H6 | 118.190(2) |
| C8-C9-C10 | 117.846(2) |
| C8-C9-H7 | 128.477(1) |
| C10-C9-H7 | 113.527(1) |
| C9-C10-N | 122.701(1) |
| C9-C10-H8 | 122.426(2) |
| N-C10-H8 | 114.865(2) |

## BIBLIOGRAPHY


[1] H. Bethe, Z. Phys. **71**, 205 (1931).

[2] F. D. M. Haldane, Phys. Lett. **93A**, 464 (1983).

[3] F. D. M. Haldane, Phys. Rev. Lett. **50**, 1153 (1983).

[4] N. W. Ashcroft and N. D. Mermin, *Solid State Physics*, W. B. Saunders Company, Orlando, 1976.

[5] D. C. Mattis, *The Theory of Magnetism*, Harper & Row, New York, 1965.

[6] J. des Cloizeaux and J. J. Pearson, Phys. Rev. **128**, 2131 (1962).

[7] A. Auerbach, *Interacting Electrons and Quantum Magnetism*, Springer-Verlag, New York, 1994.

[8] A. M. Tsvelick, *Quantum Field Theory in Condensed Matter Physics*, Cambridge University Press, Cambridge, 1995.

[9] K. Majumdar and G. E. Granroth, University of Florida, Graduate Student Seminar Notes, 1997, unpublished.

[10] Th. Jolicœur and O. Golinelli, Phys. Rev. B **50**, 9265 (1994).

[11] E. Fradkin, *Field Theories of Condensed Matter Systems*, Addison-Wesley, Redwood City, 1991.

[12] J. Saggi, Ph. D. Thesis, University of British Columbia, 1996, unpublished.

[13] I. Affleck, T. Kennedy, E. H. Lieb, and H. Tasaki, Phys. Rev. Lett. **59**, 799 (1987).

[14] I. Affleck, T. Kennedy, E. H. Lieb, and H. Tasaki, Commun. Math. Phys. **115**, 477 (1988).

[15] P. W. Anderson, Mat. Res. Bull. **8**, 153 (1973).

[16] P. W. Anderson, Science **235**, 1196 (1987).

[17] R. J. Birgeneau, to be published in J. Magn. Magn. Mater., January 1998.

[18] T. Kennedy, J. Phys. Cond. Matter **2**, 5737 (1990).

[19] T. Brill, Ph. D. Thesis, Grenoble, 1995, unpublished.

[20] H. Tasaki, Phys. Rev. Lett. **66**, 798 (1991).

[21] C. Y. Weng, Ph.D. Thesis, Carnegie Institute of Technology, 1968, unpublished.

[22] A. Meyer, A. Gleizes, J.-J. Girerd, M. Verdaguer, and O. Khan, Inorg. Chem, **21**, 1729 (1982).

[23] W. Hiller, J. Strähle, A. Datz, M. Hanack, W. E. Hatfield, L. W. ter Haar, and P. Gütlich, J. Am. Chem. Soc. **106**, 329 (1984).

[24] S. Yamamoto and S. Miyahsita, Phys. Rev. B **48**, 9528 (1993).

[25] M. Takahashi, Phys. Rev. B **38**, 5188 (1988).

[26] M. Takahashi, Phys. Rev. Lett. **62**, 2313 (1989).

[27] G. Gómez-Santos, Phys. Rev. Lett. **63**, 790 (1989).

[28] O. Golinelli, Th. Jolicœur, and R. Lacaze, J. Phys. Condens. Matter **5**, 1399 (1993).

[29] S. V. Meshkov, Phys. Rev. B **48**, 6167 (1993).

[30] S. R. White, Phys. Rev. Lett. **69**, 2863 (1992).

[31] S. R. White, Phys. Rev. B **48**, 10345 (1993).

[32] E. S. Sorensen and I. Affleck, Phys. Rev. B **49**, 15771 (1994).

[33] E. S. Sorensen and I. Affleck, Phys. Rev. B **51**, 16115 (1995).

[34] J. Deisz, M. Jarrell, and D. L. Cox, Phys. Rev. B **48**, 10227 (1993).

[35] Y. Nishiyama, K. Totuska, N. Hatano, and M. Suzuki, J. Phys. Soc. Jpn. **64**, 414 (1995).

[36] G. Sun, Phys. Rev. B **51**, 8370 (1995).

[37] U. Schollwöck and Th. Jolicœur, Europhys. Lett. **30**, 493 (1995).

[38] U. Schollwöck, O. Golinelli, and Th. Jolicœur, Phys. Rev. B **54**, 4038 (1996).

[39] S. Yamamoto, Phys. Rev. Lett. **75**, 3348 (1995).

[40] S. Miyashita and S. Yamamoto, J. Phys. Soc. Jpn. **62**, 1459 (1993).

[41] S. Miyashita and S. Yamamoto, Phys. Rev. B **48**, 913 (1993).

[42] S. Yamamoto and S. Miyahsita, Phys. Rev. B **50**, 6277 (1994).

[43] S. Yamamoto and S. Miyahsita, Phys. Rev. B **51**, 3649 (1995).

[44] E. Lieb and D. Mattis, J. Math. Phys. **3**, 749 (1962).

[45] L. P. Regnault, I. Zaliznyak, J. P. Renard, and C. Vettier, Phys. Rev. B **50**, 9174 (1994).

[46] R. Botet, R. Jullien, and M. Kolb, Phys. Rev. B **28**, 3914 (1983).

[47] I. Affleck, Phys. Rev. B **41**, 6697 (1990).

[48] A. M. Tsvelick, Phys. Rev. B **42**, 10499 (1990).

[49] I. Affleck, Phys. Rev. B **43**, 3215 (1991).

[50] O. Golinelli, Th. Jolicœur, and R. Lacaze, J. Phys. Cond. Matter **5**, 7847 (1993).

[51] Th. Jolicœur, private communications.

[52] A. Abragam and B. Bleaney, *Electron Paramagnetic Resonance of Transition Ions*, Clarendon Press, Oxford, 1970.

[53] C. P. Slichter, *Principles of Magnetic Resonance*, Springer-Verlag, Berlin, 1990.

[54] R. M. White, *Quantum Theory of Magnetism*, Springer-Verlag, Berlin, 1983.

[55] C. P. Poole, *Electron Spin Resonance*, John Wiley & Sons, New York, 1967.

[56] S. Geschwind, *Electron Paramagnetic Resonance*, Plenum Press, New York, 1972.

[57] P. P. Mitra, B. I. Halperin, and I. Affleck, Phys. Rev. B **45**, 5299 (1992).

[58] L. J. De Jongh and A. R. Miedema, Adv. Phys. **23**, 1 (1974).

[59] J. B. Goodenough, *Magnetism and the Chemical Bond*, John Wiley & Sons, New York, 1963.

[60] Z. Tun, W. J. L. Buyers, R. L. Armstrong, K. Hirakawa, and B. Briat, Phys. Rev. B **42**, 4677 (1990).

[61] J. P. Renard, M. Verdaguer, L. P. Regnault, W. A. C. Erkelens, J. Rossat-Mignod, and W. G. Sterling, Europhys **3**, 945 (1987).

[62] J. P. Renard, L. P. Ragnault, and M. Verdaguer, J. de Phys. **49**, C8-1425 (1988).

[63] K. Katsumata, H. Hori, T. Takeuchi, M. Date, A. Yamagishi, and J. P. Renard, Phys. Rev. Lett. **63**, 86 (1989).

[64] Y. Ajiro, T. Goto, H. Kikuchi, T. Sakakibara, and T. Inami, Phys. Rev. Lett. **63**, 1424 (1989).

[65] M. Date and L. Kindo, Phys. Rev. Lett. **65**, 1659 (1990).

[66] P. Gaveau, J. P. Boucher, L. P Regnault, and J. P. Renard, Europhys. Lett. **12**, 647 (1990).

[67] S. Ma, C. Broholm, D. H. Reich, B. J. Sternlieb, and R. W. Erwin, Phys. Rev. Lett. **69**, 3571 (1992).

[68] T. Kobayashi, Y. Tabuchi, K. Amaya, Y. Ajiro, T. Yosida, and M. Date, J. Phys. Soc. Jpn. **61**, 1772 (1992).

[69] N. Fujiwara, T. Goto, S. Maegawa, and T. Kohmoto, Phys. Rev. B **47**, 11860 (1993).

[70] C. P. Landee, K. A. Reza, M. R. Bond, and R. D. Willet, Phys. Rev. B **56**, 147 (1997).

[71] D. M. L. Goodgame and M. A. Hitchman, Inorg. Chem. **6**, 813 (1967).

[72] V. Gadet, M. Verdaguer, V. Briois, A. Gleizes, J. P. Renard, P. Beauvillian, C. Chappert, T. Goto, K. Le Dang, and P. Veillet, Phys. Rev. B **44**, 705 (1992).

[73] T. Takeuchi, H. Hori, T. Yosida, A. Yamagishi, K. Katsumata, J. P. Renard, V. Gadet, M. Verdaguer, and M. Date, J. Phys. Soc. Jpn. **61**, 3262 (1992).

[74] L.-K. Chou, K. A. Abboud, D. R. Talham, W. W. Kim, and M. W. Meisel, Chem. Mater. **6**, 2051 (1994).

[75] G. E. Granroth, L.-K. Chou, W. W. Kim, M. Chaparala, M. J. Naughton, E. Haanappel, A. Lacerda, D. Rickel, D. R. Talham, and M. W. Meisel, Physica B **211**, 208 (1995).

[76] G. E. Granroth, M. Chaparala, L.-K. Chou, M. Orendáč, A. Orendáčová, J. Černák, A. Feher, D. R. Talham, and M. W. Meisel, *Physical Phenomena at High Magnetic Fields-II*, ed. Z. Fisk, L. Gor'kov, D. Meltzer and R. Schrieffer, World Scientific, Singapore, 1996.

[77] J. P. Renard, V. Gadet, L. P. Regnault, and M. Verdaguer, J. Magn. Magn. Mater. **90 & 91**, 213 (1990).

[78] S. Lee, P. Colombet, G. Ouvrard, and R. Brec, Mater. Res. Bull. **21**, 917 (1986).

[79] H. Mutka, J.L. Soubeyroux, G. Bourleaux, and P. Colombet, Phys. Rev. B **39**, 4820 (1989).

[80] M. Takigawa, T. Asano, Y. Ajiro, and M. Mekata, Phys. Rev. B. **52**, R13087 (1995).

[81] V. Gadet, M. Verdaguer, J. P. Renard, J. Ribas, C. Diaz, M. Monfront, X. Solans, C. P. Landee, J. P. Jamet, and A. Dworkin, unpublished.

[82] A. Zheludev, S. E. Nagler, S. M. Shapiro, L.-K. Chou, D. R. Talham, and M. W. Meisel, Phys. Rev. B **53**, 15004 (1996).

[83] L.-K. Chou, Ph. D. Thesis University of Florida, 1996.

[84] H. Kikuchi, Y. Ajiro, N. Mori, T. Goto, and H. Aruga, Solid State Comm. **76**, 999 (1990).

[85] D. J. Buttrey and J. D. Sullivan, J. Solid State Chem. **88**, 291 (1990).

[86] J. Amador, E. Gutiérrez-Puebla, M. A. Monge, I. Rasines, C. Ruíz-Valero, F. Fernández, R. Sáez-Puche, and J. A. Campá, Phys. Rev. B **42**, 7918 (1990).

[87] J. A. Alonso, J. Amador, J. L. Martínez, I. Rasines, J. Rodríguez-Caravajal, R. Sáez-Puche, Solid State Comm. **76**, 467 (1990).

[88] R. Sáez-Puche, J. M. Coronado, C. L. Otero-Díaz, and J. M. Martín Llorente, J. Solid State Chem. **93**, 461 (1991).

[89] E. García-Matres, J. L. Martínez, and J. Rodríguez-Carvajal, J. Solid State Chem. **103**, 322 (1993).

[90] J. Darriet and L. P. Regnault, Solid State Comm. **86**, 409 (1993).

[91] J. F. DiTusa, S-W. Cheong, J.-H. Park, G. Aeppli, C. Brohom, and C. T. Chen, Phys. Rev. Lett. **73**, 1857 (1994).

[92] B. Batlogg, S-W. Cheong, and L. W. Rubb, Jr., Physica B **194-196**, 173 (1994).

[93] T. Yokoo, T. Sakaguchi, K. Kakuri, and J. Akimitsu, J. Phys. Soc. Jpn. **64**, 3651 (1995).

[94] G. Xu, J. F. DiTusa, T. Ito, K. Oka, H. Takagi, C. Broholm, and G. Aeppli, Phys. Rev. B **54**, R6827 (1996).

[95] H. A. Goodwin and R. N. Sylva, Aust. J. Chem. **20**, 629 (1967).

[96] S. P. Perlepes, A. G. Balckman, J. C. Huffman, and G. Christou, Inorg. Chem. **30**, 1665 (1991).

[97] G. E. Granroth, M. W. Meisel, M. Chaparala, Th. Jolicœur, B. H. Ward, and D. R. Talham, Phys. Rev. Lett. **77**, 1616 (1996).

[98] M. Chiba, Y. Ajiro, H. Kikuchi, T. Kubo, and T. Morimoto, Phys. Rev. B **44**, 2838 (1991).

[99] T. M. Brill, J. P. Boucher, L. C. Brunel, J. P. Renard, and M. Verdaguer, Physica B **204**, 303 (1995).

[100] M. Sieling, W. Palme, and B. Lüthi, Z. Phys. B **96**, 297 (1995).

[101] J. Saggi and I. Affleck, Phys. Rev. B **53**, 15004 (1996).

[102] A. P. Reyes, H. N. Bachman, X. P. Tang, M. W. Meisel, W. P. Halperin, N. Fujiwara, and T. Goto, Phys. Rev. B **55**, 8079 (1997).

[103] T. Goto, N. Fujiwara, T. Kohmoto, and S. Maegawa, J. Phys. Soc. Jpn. **59**, 1135 (1990).

[104] N. Fujiwara, T. Goto, S. Maegawa, and T. Kohmoto, Phys. Rev. B. **45**, 7837 (1992).

[105] T. Shimizu, D. E. MacLaughlin, P. C. Hammel, and J. D. Thompson, Phys. Rev. B **52**, R9835 (1995).

[106] S. Kimura, H. Ohta, M. Motokawa, T. Yokoo, J. Akimitsu, to be published J. Magn. Magn. Mater. January (1998).

[107] L. C. Brunel, T. M. Brill, I. Zaliznyak, J. P. Boucher, and J. P. Renard, Phys. Rev. Lett. **69**, 1699 (1992).

[108] M. Hagiwara, K. Katsumata, I. Affleck, B. I. Halperin, and J. P. Renard, Phys. Rev. Lett. **65**, 3181 (1990).

[109] S. H. Glarum, S. Geschwind, K. M. Lee, M. L. Kaplan, and J. Michel, Phys. Rev. Lett. **67**, 1614 (1991).

[110] Y. Ajiro, T. Uchikawa, T. Asano, M. Mekata, and N. Mori, J. Phys. Soc. Jpn. **66**, 971 (1997).

[111] N. Fujiwara, J. R. Jeitler, C. Navas, M. M. Turnbull, T. Goto and N. Hosioito, J. Magn. Magn. Mater. **140-144**, 1663 (1995).

[112] H. Kikuchi, Y. Ajiro, N. Mori, H. Aruga Katori, T. Goto, and H. Nagasawa, Physica B **201**, 186 (1994).

[113] A. P. Ramirez, S-W. Cheong, and M. L. Kaplan, Phys. Rev. Lett. **73**, 1857 (1994).

[114] H. Kikuchi, H. Nagasawa, K. Mibu, T. Ono, N. Hosoito, and T. Shinjyo, J. Phys. Soc. Jpn. **64**, 3429 (1995).

[115] H. Deguchi, S. Takagi, M. Ito, and K. Takeda, J. Phys. Soc. Jpn. **64**, 22 (1995).

[116] K. Hallberg, C. D. Betista, and A. A. Aligia, LANL cond-mat/9709111.

[117] E. Dagotto, J. Riera, A. Sandvik, and A. Moreo, Phys. Rev. Lett. **76**, 1731 (1996).

[118] M. Hagiwara and K. Katsumata, J. Phys. Soc. Jpn. **61**, 1481 (1992).

[119] O. Avenel, J. Xu, J. S. Xia, M-F. Xu, B. Andraka, T. Lang, P. L. Moyland, W. Ni, P. J. C. Signore, C. M. C. M. van Woerkens, E. D. Adams, G. G. Ihas, M. W. Meisel, S. E. Nagler, N. S. Sullivan, Y. Takano, D. R. Talham, T. Goto, and N. Fujiwara, Phys. Rev. B **46**, 8655 (1992).

[120] O. Avenel, J. Xu, J. S. Xia, M-F. Xu, B. Andraka, T. Lang, P. L. Moyland, W. Ni, P. J. C. Signore, C. M. C. M. van Woerkens, E. D. Adams, G. G. Ihas, M. W. Meisel, S. E. Nagler, N. S. Sullivan, Y. Takano, D. R. Talham, T. Goto, and N. Fujiwara, J. Low Temp. Phys. **89**, 547 (1992).

[121] H. Yamazaki and K. Katsumata, Phys. Rev. B **54**, R6831 (1996).

[122] I. Affleck, Phys. Rev. Lett. **62**, 474 (1989).

[123] M. L. Plumer and A. Caillé, Phys. Rev. Lett. **68**, 1042 (1992).

[124] I. Affleck and G. F. Wellman, Phys. Rev. B **46**, 8934 (1992).

[125] M. Hagiwara, K. Katsumata, and T. Yosida, Hyper. Inter. **78**, 415 (1993).

[126] Y. Trudeau, D. Sénéchal, and M. Poirier, Phys. Rev. B **51**, 334 (1995).

[127] A. Zheludev, J. M. Tranquada, T. Vogt, and D. J. Buttrey, Phys. Rev. B **54**, 6437 (1996).

[128] V. Sachan, D. J. Buttrey, J. M. Tranquada, and G. Shirane, Phys. Rev. B **49**, 9658 (1994).

[129] A. Zheludev, J. P. Hill, and D. J. Buttrey, Phys. Rev. B **54**, 7216 (1996).

[130] A. Zheludev, J. M. Tranquada, T. Vogt, and D. J. Buttrey, Phys. Rev. B **54**, 7211 (1996).

[131] T. Yokoo, A. Zheludev, M. Nakamura, and J. Akimitsu, Phys. Rev B **55**, 11516 (1997).

[132] I. A. Zaliznyak, D. Dender, C. L. Broholm, and D. H. Reich, LANL cond-mat/9709150.

[133] M. Ito, H. Yamashita, T. Kawae, and K. Takeda, J. Phys. Soc. Jpn. **66**, 1265 (1997).

[134] User manual for the Quantum Design MPMS magnetometer, Quantum Design, Inc., San Diego, CA.

[135] J. Clarke in *Superconducting Devices*, ed. S. T. Ruggiero and D. A. Rudman, Academic press, San Diego, 1990.

[136] M. Chaparala, O. H. Chung, and M. J. Naughton, AIP Conf. Proc. **273**, 407 (1992).

[137] Sales literature for Oxford Instruments MagLab system, Oxford Instruments, Oxford, Great Britain.

[138] W. H. Press, S. A. Teukolsky, W. T. Vetterling, and B. P. Flannery, *Numerical Recipes in C*, Cambridge University Press, Cambridge, 1992.

[139] R. S. Alger, *Electron Paramagnetic Resonance*, John Wiley & Sons, New York, 1968.

[140] *Oxford Instruments ESR 900 Flow Cryostat User Maual*, Oxford Instruments, Oxford, Great Britain.

[141] S. W. Lovesey, *Theory of Neutron Scattering from Condensed Matter*, Vol 1, Oxford University Press, Oxford, 1984.

[142] D. L. Price and K. Sköld in *Methods of Experimental Physics*, Vol 23 C, ed. K. Sköld and D. L. Price, Academic Press, Orlando, 1987.

[143] H. M. Rietveld, Acta. Crystallogr. **21**, A228 (1966).

[144] H. M. Rietveld, Acta. Crystallogr. **22**, 151 (1967).

[145] H. M. Rietveld, J. Appl. Crystallogr. **2**, 65 (1969).

[146] A. N. Fitch, A. F. Wright, and B. Fender, Acta Crystallogr. **38**, 2546 (1982).

[147] R. A. Young, *Rieveld Refinement*, Oxford University Press, Oxford, 1993.

[148] M. Yethiraj and J. A. Fernandez-Baca http://neutrons.ornl.gov/NSatHFIR/Instruments/HFIRInsts.HTML# HB-4B (1996).

[149] http://rrdjazz.nist.gov/fctof.html (1996).

[150] L. Keviczky, M. Hilger and J. Kolostori, *Mathematics and Control Engineering of Grinding Technology*, Kluwer Academic Publishers, Dordrecht, 1989.

[151] T. Allen, *Particle Size Measurement*, Chapman and Hall, London, 1990.

[152] A. Montaser and D. W. Golightly, *Inductively Coupled Plasmas in Analytical Atomic Spectrometry*, VCH Publishers, Inc., New York, 1987.

[153] A. R. Date and A. L. Gray, *Applications of Inductively Coupled Plasma Mass Spectrometry*, Blackie and Sons Ltd., Glasgow, 1989.

[154] M. Sieling, W. Palme, B. Lüthi, T. M. Brill, J. P. Boucher, and J. P. Renard, J. Magn. Magn. Mater. **140-144**, 1637 (1995).

[155] N. Koido, T. Kambe, S. Teraoka, S. Hirai, T. Goto, L.-K. Chou, D. R. Talham, M. W. Meisel, and K. Nagata, J. Magn. Magn. Mater. **140-144**, 1639 (1995).

[156] L.-K. Chou, D. R. Talham, W. W. Kim, P. J. C. Signore, and M. W. Meisel, Physica B **194-196**, 313 (1994).

[157] B. H. Ward, private communications.

[158] M. Monfort, J. Ribas, X. Solans, and M. Font-Bardía, Inorg. Chem. **35**, 7633 (1996).

[159] I. Affleck and R. A. Weston, Phys. Rev. B **45**, 4667 (1992).

[160] J. Ribas, M. Monfort, C. Diaz, C. Bastos, C. Mer, and X. Solans, Inorg. Chem. **34**, 4986 (1996).

[161] B. H. Ward, G. E. Granroth, D. R. Talham, and M. W. Meisel, to be published in J. Magn. Magn. Mater., January 1998.

[162] C. A. Hayward, D. Poilblanc, and L. P. Lévy, LANL cond-mat/9606145.

[163] P. R. Hamar and D. H. Reich, J. Appl. Phys. **79**, 5392 (1996).

[164] M. Hagiawara and K. Katsumata, J. Magn. Magn. Mater. **140-144**, 1665 (1995).

[165] P. R. Bevington and D. K. Robinson, *Data Reduction and Error Analysis for the Physical Sciences*, Mc-Graw Hill, Boston, 1992.

[166] R. M. Mueller, Ph. D. Thesis, University of Florida, 1976.

[167] P. J.-C. Signore, Ph. D. Thesis, University of Florida, 1994.

[168] G. E. Granroth, S. Maegawa, M. W. Meisel, N. S. Bell, J. H. Adair, B. H. Ward, L.-K. Chou, and D. R. Talham, LANL cond-mat/9710161.

[169] K. D. Bowers and J. Owen, Rep. Prog. Phys. **18**, 304 (1955).

[170] B. H. Ward, Ph.D. Thesis, University of Florida, 1997.

[171] A. K. Gregson and N.T. Moxon, Inorg. Chem. **21**, 586 (1982).

[172] J. A. Bonadies, M. L. Kirk, M. Soo Lah, D. P. Kessissoglou, W. E. Hatfield, and V. L. Pecoraro, Inorg. Chem. **28**, 2037 (1989).

[173] C. Bellito, L. P. Regnault, and J. P. Renard, J. Magn. Magn. Mater. **102**, 116 (1991).

[174] S. Yamamoto, Phys. Rev. B **53**, 3364 (1996).

## BIOGRAPHICAL SKETCH

Garrett Earl Granroth was born the youngest son of Earl G. and Barbra J. Granroth on October 13, 1971 in Rockford, Illinois. He started elementary school in the fall of 1976. During these years, his interest in the physical sciences developed through several chemistry classes. Garrett graduated from Booker High School in Sarasota, Florida in the spring of 1989. At Stetson University, in DeLand, Florida, and under the direction of Professor Kevin Riggs, he conducted research on magnetic thin films using the techniques of ferromagnetic resonance and the magneto-optical Kerr effect. After four years, Garrett graduated Cum Laude with a B.S. in physics on a hot summer day in 1993. The fall of 1993 saw Garrett beginning his graduate studies at the University of Florida in physics. In the spring of 1994, he joined the research group of Professor Mark W. Meisel to begin the work of which this thesis is the culmination. Besides the work of this thesis, he also took the opportunity to make several ultrasound measurements in normal and superfluid $^3$He at $T \approx 200\ \mu$K.

I certify that I have read this study and that in my opinion it conforms to acceptable standards of scholarly presentation and is fully adequate, in scope and quality, as a dissertation for the degree of Doctor of Philosophy.

Mark W. Meisel, Chairman
Associate Professor of Physics

I certify that I have read this study and that in my opinion it conforms to acceptable standards of scholarly presentation and is fully adequate, in scope and quality, as a dissertation for the degree of Doctor of Philosophy.

Selman P. Hershfield
Associate Professor of Physics

I certify that I have read this study and that in my opinion it conforms to acceptable standards of scholarly presentation and is fully adequate, in scope and quality, as a dissertation for the degree of Doctor of Philosophy.

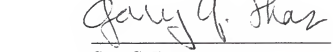

Gary G. Ihas
Professor of Physics

I certify that I have read this study and that in my opinion it conforms to acceptable standards of scholarly presentation and is fully adequate, in scope and quality, as a dissertation for the degree of Doctor of Philosophy.

Fred Sharifi
Assistant Professor of Physics

I certify that I have read this study and that in my opinion it conforms to acceptable standards of scholarly presentation and is fully adequate, in scope and quality, as a dissertation for the degree of Doctor of Philosophy.

Dan R. Talham
Associate Professor of Chemistry

This dissertation was submitted to the Graduate Faculty of the Department of Physics in the College of Liberal Arts and Sciences and to the Graduate School and was accepted as partial fulfillment of the requirements for the degree of Doctor of Philosophy.

May 1998

Dean, Graduate School

LD
1780
199_
.G759